GENERATION DEPENDENT ULTRAFAST CHARGE SEPARATION AND RECOMBINATION IN PYRENE-VIOLOGEN SYSTEMS

By ZHENG GONG

A dissertation submitted to the

Graduate School-Newark

Rutgers, The State University of New Jersey

In partial fulfillment of the requirements

for the degree of

Doctor of Philosophy

Graduate Program in Chemistry

written under the direction of

Professor Piotr Piotrowiak

and approved by

_____

_____

_____

_____

Newark, New Jersey

May, 2018

ABSTRACT OF THE DISSERTATION

GENERATION DEPENDENT ULTRAFAST CHARGE SEPARATION AND RECOMBINATION IN PYRENE-VIOLOGEN SYSTEMS

by ZHENG GONG

Dissertation Director: Professor Piotr Piotrowiak

The dissertation consists of two projects: electron transfer dynamics in pyrene-viologen donor-acceptor dendritic systems and vibrational cooling of the photoexcited methyl viologen radical cation. Two projects are closely related and involve same experimental techniques.

In the first project, the ability of a dendritic network to intercept electrons and extend the lifetime of a short-lived photoinduced charge separated (CS) state was investigated in a homologous family of a pyrene-methylene-viologen dendron family in which the number of viologen subunits grows exponentially from P−C1−G0 to P−C1−G3. The CS state in the parent diad P−C1−G0 with a single acceptor exhibits an extremely short lifetime of $\tau = 0.72$ ps. The expansion of the viologen network introduces slower components to the recombination kinetics by allowing the injected electron to migrate further away from the donor. As a result, the fraction of long-lived population increases with 10-fold or greater lifetime extension in the order of P−C1−G3 > P−C1−G2 > P−C1−G1 > P−C1−G0, which can be interpreted in terms of the electron hopping between two viologen sites and long-range electron tunneling across multiple viologen units.

Additionally, the influences of donor-acceptor separation, connectivity, and solvent on electron transfer rates were studied applying different pyrene-viologen donor-acceptor systems.

In the second project, the vibrational cooling of hot ground state methyl viologen radical cation ($MV^{+\bullet}$) was studied using femtosecond pump-probe spectroscopy. The photoexcitation of the $D_1 \leftarrow D_0$ transition led to very rapid internal conversion within 460 fs, generating a vibrationally excited ground state of $MV^{+\bullet}$ which thermalized on 1.6~16 ps time scale. The initial stage of vibrational excess energy loss corresponds to the intermolecular energy transfer to vibrational modes of the surrounding medium molecules, and the latter stage involves energy dissipation into relatively low-frequency librational and translational modes of the solvent. The effect of solvent and host-guest complexation on cooling dynamics of $MV^{+\bullet}$ was also investigated, and the results suggested that a good match between the density of vibrational states in $MV^{+\bullet}$ and surrounding medium could efficiently accelerate the vibrational cooling.

ACKNOWLEGEMENT

I am grateful for the help I have received from many people in this work. Firstly, I would like to express my sincere gratitude to my advisor Prof. Piotrowiak for his continuous support of my Ph.D. study and related research, for his patient explanations from fundamental optics to sophisticated theory, and for his contributions of time, ideas and funding to make my Ph.D. experience productive and stimulating. The enthusiasm and immerse knowledge he has for his research inspires me and will have a profound impact on the rest of my life. It has been a great honor to be his student.

Secondly, I would like to acknowledge my thesis committee members, Prof. Lockard, Prof. Pavanello, and Prof. Chen for their time, interest, and insightful comments.

Thirdly, I am thankful to the collaborators and colleagues I have worked with in this program. My deepest thanks go to Prof. Iyoda and Prof. Kawauchi for their beautiful synthesis of dendron samples which have been used in most experiments presented in this dissertation. I would also like to thank all the faculty and staff in the Chemistry Department for their help over the past five years. I especially appreciate the help from a former member Dr. Bao in our group who taught me to set up the pump-probe experiment. I thank my colleagues Mandy and Lujia for the happy time we spent together during my study at Rutgers. I am grateful for conversations with Pablo who guided me to calculate the molecular dynamics simulation.

Finally, I take this opportunity to express the gratitude from my deep heart to my beloved parents for their love and support, both spiritually and materially.

TABLE OF CONTENT

LIST OF TABLES

LIST OF FIGURES AND SCHEMES

Chapter 1. Introduction of Photoinduced Electron Transfer

This chapter provides a brief review on the development of the field of photoinduced electron transfer and an introduction to basic electron transfer theory. The differences between adiabatic and nonadiabatic electron transfer reactions are distinguished. The essential equations and predictions of the classical Marcus theory are included as well as the concepts of inner-sphere and outer-sphere reorganization energy. An application of quantum mechanical theories on nonadiabatic electron transfer processes is also described. Finally, the more enhanced semiclassical Marcus-Jortner rate equation is expressed.

1.1 Scope of photoinduced electron transfer

Photoinduced electron transfer (PET) is the process of transferring an electron from an excited-state donor to a ground-state acceptor [1]. In the past few decades, the phenomenon of PET has attracted considerable interest among chemists in various areas of research. In organic chemistry, PET has been the subject of synthetic development in solar cells. For instance, the discovery of PET in the composite of conducting polymers as donors and fullerene derivatives as acceptors provides a novel approach to design efficient photovoltaics [2, 3]. The other crucial organic aspect of PET application appears in the synthesis of fluorescent sensors and switches through a photoinduced metal-to-fluorophore electron transfer mechanism [4, 5]. For inorganic chemists, studying the photoinduced electron transfer from quantum dots to metal oxides or metal complexes is the key to the development of energy conversion and light-harvesting devices [6-8]. Biologists are

mainly focusing on photosynthesis and electron transport in biological structures. The investigation of PET reactions and the solution of the crystal structure of the photosynthetic reaction center in purple bacteria contributed to understanding the primary processes involved in photosynthesis [9]. In addition, the π-stacked bases of DNA double-helix could provide a better intervening medium to examine the distance dependence of PET reactions [10-12].

Theoretical study is also an important aspect in the field of PET. The most successful theory of electron transfer was introduced and developed by Marcus, Levich, Dogonadze, and later elaborated by Jortner (See **1.4.2**). The theoretical predictions were validated thanks to the ultrafast laser technology and spectroscopy which permits the direct observations and measurements of radical ion intermediates in rapid chemical reactions while the theory predicts the electron transfer pathway [6-8, 14-16].

1.2 The electron exchange interaction for electron and energy transfer

In an electron transfer reaction between two ground states from an electron donor (D) to an acceptor (A): $D + A \rightarrow D^{\bullet+} + A^{\bullet-}$, both D and A are molecular entities either brought together in a collision complex or chemically linked by a covalent bond. PET is an electron transfer process which involves an electronically excited state.

Generally, there are four kinds of photoinduced electron and energy transfer processes (**Scheme 1**). Energy transfer occurs either through an electron exchange interaction which requires orbital overlap or through a dipole-dipole interaction. Specifically, dipole-dipole electronic energy transfer occurs when two oscillating electric dipole fields interact through space occupied with molecules or empty space, therefore,

orbital overlap and electron exchange are not required [17]. Whereas, photoinduced electron or hole transfer only occurs through an electron exchange interaction (**Figure 1**).

1) **Electron transfer:** $\boldsymbol{R_1{}^*(D) + R_2(A) \rightarrow I(R_1{}^{\bullet+}, R_2{}^{\bullet-})}$
2) **Hole transfer:** $\boldsymbol{R_1(D) + R_2{}^*(A) \rightarrow I(R_1{}^{\bullet+}, R_2{}^{\bullet-})}$
3) **Exchange electronic energy transfer:** $\boldsymbol{R_1{}^* + R_2 \rightarrow R_1 + R_2{}^*}$
4) **Dipole-dipole electronic energy transfer:** $\boldsymbol{R_1{}^* + R_2 \rightarrow R_1 + R_2{}^*}$

Scheme 1. Four kinds of electronic electron and energy transfer processes [18]. *R* and *R** are the ground-state and excited-state reactant respectively, and *I* stands for intermediate generated in the reaction.

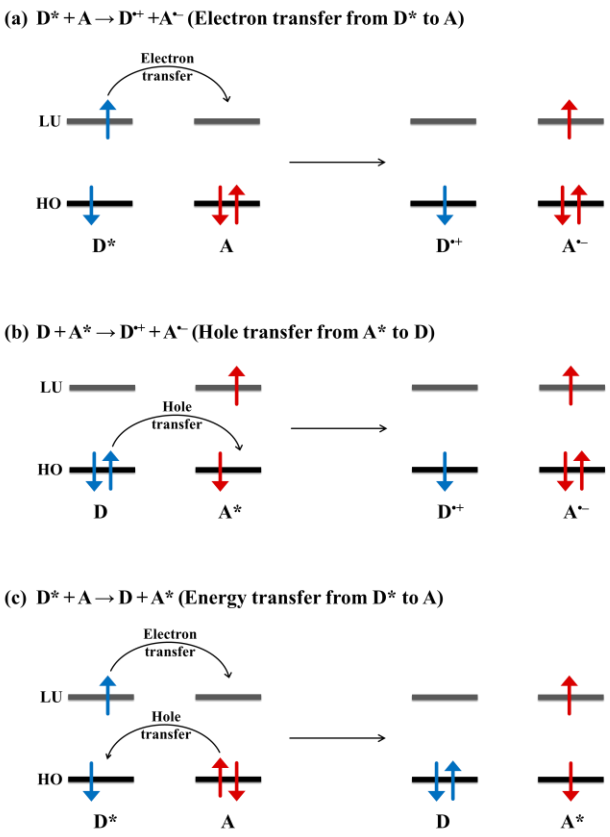

Figure 1. Frontier orbital representation of electron exchange in photoinduced (a) electron transfer from an excited-state donor (D^*) to a ground-state acceptor (A), (b) hole transfer

from an excited-state acceptor (A^*) to a ground-state donor (D), and (c) electron exchange energy transfer from D^* to A by the Dexter mechanism [1, 18-20].

1.3 Energetics

The feasibility of electron transfer between an excited-state donor (D^*) and ground-state acceptor (A) is dictated by the overall free energy change ΔG [14]. From the point of view of thermodynamics, the condition of exothermicity ($\Delta G < 0$) is favored so that the electron transfer process is able to compete with other pathways such as internal conversion and inter system crossing.

For electron transfer between two ground-state molecules in the gas phrase, the standard free energy change is given by

$$\Delta G_g\ (ET) = (IP)_D - (EA)_A$$

where $(IP)_D$ is the ionization potential of the ground-state donor and $(EA)_A$ is the electron affinity of the ground-state acceptor.

For photoinduced electron and hole-transfer reactions involving an excited-state, the value of the free energy ΔG^* changes by the magnitude of E_{D^*} and E_{A^*} respectively as shown in **Figure 2**.

Thus, if the donor is electronically excited,

$$\Delta G^*\ (PET) = (IP)_D - (EA)_A - E_{D^*}$$

If the acceptor is electronically excited and hole transfer occurs,

$$\Delta G^*\ (PHT) = (IP)_D - (EA)_A - E_{A^*}$$

Where E_{D^*} and E_{A^*} are electronic excitation energy of donor and acceptor, respectively.

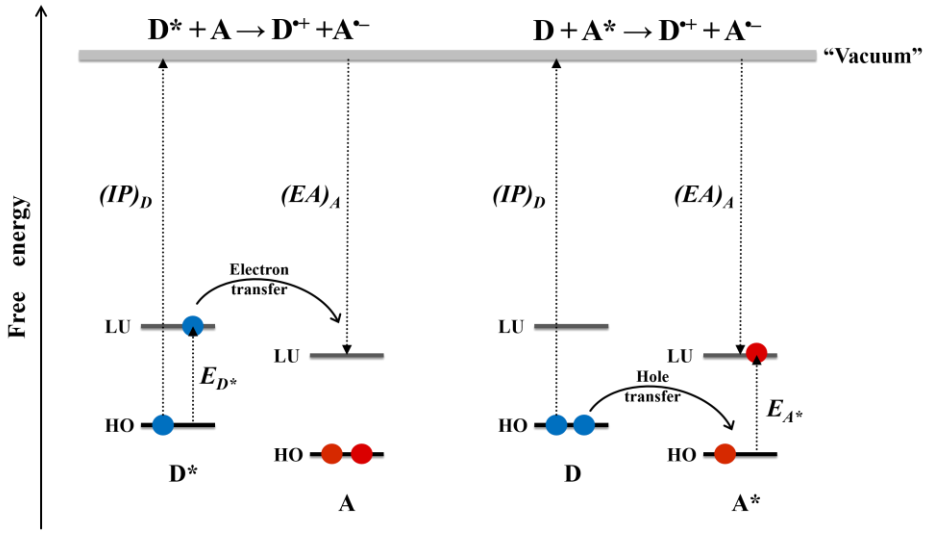

Figure 2. Energetics of electron and hole transfer [14, 18].

To derive a more realistic equation of free energy change for electron transfer reactions taking place in liquid solution, both Coulombic interactions and solvent stabilization of all participants must be accounted for [21].

Considering the solvent stabilization effect, the standard free energy change in solution $\Delta G_{sol}\ (ET)$ can be translated from gas-phase value of $\Delta G_g\ (ET)$ by directly employing the experimental electrochemical potentials for the oxidation $E^{\circ}_{D^+/D}$ and reduction E°_{A/A^-} in solution which can be determined using experimental techniques such as cyclic voltammetry [18].

Therefore, the free energy change in solution can be obtained by

$$\Delta G^*_{sol}\ (PET) = E^{\circ}_{D^+/D} - E^{\circ}_{A/A^-} - E_{D^*}$$

The Coulombic term for interaction between two oppositely charged ions $(-e^2/\varepsilon r)$ can be introduced in $\Delta G^*_{sol}\ (PET)$, which finally gives rise to the Rehm-Weller equation [22]:

$$\Delta G^*_{sol}\,(PET) = E^{\circ}_{D^+/D} - E^{\circ}_{A/A^-} - E_{D^*} - \frac{e}{4\pi\varepsilon_0\varepsilon_s r_{D^+A^-}}$$

where $r_{D^+A^-}$ is the center-to-center distance between oxidized donor (D^+) and reduced acceptor (A^-), ε_s is the dielectric constant of the solvent, and ε_0 is the vacuum permittivity.

1.4 Dynamics of electron transfer

1.4.1 Adiabatic and nonadiabatic electron transfer processes

The rate of most electron transfer reactions, as with other chemical reactions, can be originally expressed by the Arrhenius equation:

$$k_{et} = A \cdot \exp(-\frac{E_a}{k_B T})$$

where A is the preexponential factor, k_B is the Boltzmann constant, T is the absolute temperature, and E_a is the activation energy.

According to the classical transition state theory, the first-order rate constant is given by

$$k_{et} = \kappa\nu_n \cdot \exp(-\frac{\Delta G^{\neq}}{k_B T})$$

where κ is the transmission coefficient, ν_n is the average low-frequency of nuclear motions that takes the system through the transition state, and the activation energy is replaced by activation free energy $\Delta G^{\neq}$.

The preexponential factor κ, which is described by the Landau-Zener theory [23, 24], is a product of two factors, nuclear and electronic [25]. Nuclear factor determines the probability of nuclear tunneling leading from reactants to products without activation to the transition state (TS). Electronic factor is related to the interaction energy $|V|$ between the initial and final states (the resonance integral). If this value is sufficiently high, the

mixing between these two states is strong, which results in the splitting of electronic energy levels at the intersection region and a decrease in energy barrier (**Figure 3**). This is described as an adiabatic behavior [26]. However, for an electron transfer process where no bond is made or broken, the electronic interaction is relatively weak, and the system continues on the initial surface and gets reflected back many times before it finally jumps to the other surface, which is defined as a nonadiabatic process [27].

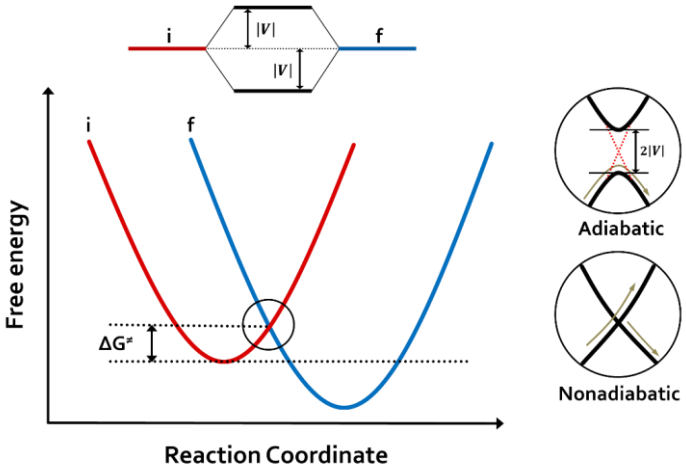

Figure 3. Schematic representation of free energy cross sections of initial (i) and final (f) states. The intersection region is addressed in black circles showing the adiabatic and nonadiabatic processes which can be distinguished depending on the magnitude of V. V is matrix element for the electronic coupling between initial and final states.

In fact, the adiabatic and nonadiabatic processes are distinguished as two limiting cases of a transition-state formalism depending on the magnitude of electronic coupling. In an adiabatic electron transfer process ($|V| \gg k_B T$), the reacting system always stays on the lowest energy surface while proceeding to the product, which gives $\kappa \cong 1$. Therefore,

$$k_{et} = \nu_n \cdot \exp(-\frac{\Delta G^{\neq}}{k_B T})$$

where ν_n is likely to be dominated by a solvent relaxation or an inner-shell vibrational mode.

At the other extreme, when V is very small, the probability of crossing from initial to final state at the intersection region is much lower, which corresponds to $\kappa \ll 1$. In this case, the electron transfer rate is significantly decreased and not merely controlled by the nuclear motion. As a result, the calculation should be approached by a quantum mechanical method such as Fermi's "golden rule" [28] which is also a good starting point for a rate constant expression of the nonadiabatic electron transfer reaction:

$$k_{et} = \frac{2\pi}{\hbar} |V\ |^2 FCWD$$

where $\hbar = \frac{h}{2\pi}$, h is Planck constant;

$FCWD$ stands for Franck-Condon weighted density-of-states which is a sum of the overlap integrals of the nuclear wavefunctions of the reactants and products [29]:

$$FCWD = \sum_j \sum_i \langle \chi_{Pj} | \chi_{Ri} \rangle^2 \, p(\epsilon_{Ri}) \delta(\epsilon_{Pj} - \epsilon_{Ri})$$

where χ_{Ri} and χ_{Pj} are the vibrational wave functions for the equilibrium reactant state at level i and the equilibrium product state at level j respectively; ϵ_{Ri} and ϵ_{Pj} are the vibrational energies of level i in the reactant state and levels j in the product state separately; $\langle \chi_{Pj} | \chi_{Ri} \rangle^2$ is called the Franck-Condon (FC) factor for levels i and j which incorporates both internal and solvent modes; $p(\epsilon_{Ri})$ is the Boltzmann probability of finding the reactant state in the level i with energy ϵ_{Ri}; the sum is taken over all vibronic

sates (including solvent oscillators) in both reactant and product state; δ is the Dirac delta function ($\delta = 0$ if $\epsilon_{Pj} \neq \epsilon_{Ri}$; $\delta = 1$ if $\epsilon_{Pj} = \epsilon_{Ri}$);

V is the electronic coupling between donor and acceptor which decreases exponentially with increasing the donor-acceptor separation distance r_{DA} [30]:

$$V = V_{DA}^{0} \cdot \exp\left[-\frac{1}{2}\beta(r_{DA} - r_0)\right]$$

where V_{DA}^{0} is the electronic coupling when donor and acceptor are in contact at van der Waals separation r_0, and β is an attenuation parameter which reflects the sensitivity of the electronic coupling to distance.

It should be noted that this relationship was derived using McConnell's superexchange model for electron tunneling through a single potential barrier [30]. In order to connect with the Arrhenius equation, V is included into the preexponential factor A.

1.4.2 Classical Marcus theory

The development of electron transfer theory in the condensed phrase was initiated by Libby who qualitatively explained the electron transfer behavior on the basis of related ideas of FC principle. Libby [31] claimed that the electron transfer from one reacting ion or molecule to another, which was through a vertical transition and governed by FC principle (**Figure 4**), would be a much faster process than structural rearrangement of surrounding solvent stimulated by the creation of charged ion pair. However, Libby's model failed to satisfy the energy conservation law while considering the electron transfer reactions taking place in the dark. Based on his work, Marcus developed a more successful and sophisticated model [32-37].

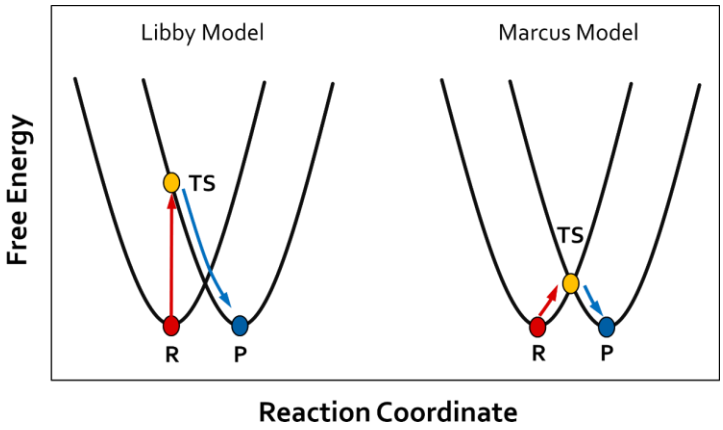

Figure 4. The comparison of Libby and Marcus model in terms of potential energy surfaces for a self-exchange reaction [18]. R and P indicate the initial reactant and final product, and TS stands for the transition state intermediate.

According to the Marcus model, the potential energy (PE) of the initial reactants, which is a function of all nuclear coordinates (including the orientational coordinates of the surrounding solvent molecules), can define a multidimensional parabolic PE surface and can be further simplified to a harmonic free energy curve that is a function of a single reaction coordinate [34-36]. In this way, Marcus connected the transition state theory with the electron transfer process by incorporating the nuclear motion and solvent motion into the activation free energy $\Delta G^{\neq}$ as the reorganization energy λ. The standard free energy change of the reaction, ΔG°, is defined as a difference between minimum of PE curves of reactants and products (**Figure 5**). The reorganization energy λ is defined as energy for the vertical transition without replacement of the nuclear frame and solvent coordinates, namely, from the minimum of the ground-state parabola of the reactants to the intersection with the parabola of the products. Marcus pointed out that, instead of "vertical transition" pathway, there is another energetically less expensive pathway to move the system from reactant state to product state through a transition state where the geometry of the system

remains unchanged (**Figure 4**) [27].

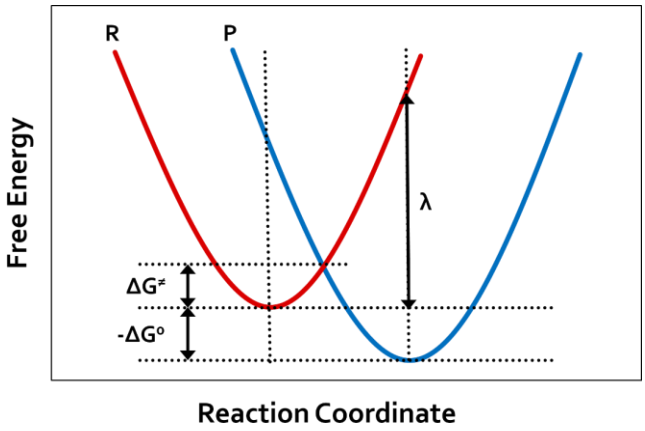

Figure 5. One-dimensional representation of PE curves of an electron transfer reaction according to Marcus model.

Based on the Marcus quadratic relationship, the activation free energy of the reaction can be derived [34-36]:

$$\Delta G^{\neq} = \frac{(\Delta G^{\circ} + \lambda)^2}{4\lambda}$$

Then, Marcus firstly presented that the first-order rate constant (k_{et}) for outer-sphere electron transfer reactions would be related to the free activation energy on the basis of transition state theory [32, 33] and expressed by

$$k_{et} = \kappa \nu_n \bullet \exp\left[-\frac{(\Delta G^{\circ} + \lambda)^2}{4\lambda k_B T}\right]$$

This pioneering Marcus equation predicts the exponential dependence for the rate constant on relative magnitudes of the driving force $-\Delta G^{\circ}$and the reorganization energy λ. Particularly, for an isoenergetic reaction where $-\Delta G^{\circ} = 0$ (**Figure 6a**),

$$\Delta G^{\neq} = \frac{\lambda}{4}$$

Pulling vertically the parabola representing PE surface of products down makes the reaction more and more exothermic with increasing the value of $-\Delta G^{\circ}$. During this process, the free activation energy firstly decreases, then become zero, and finally increases again, which gives rise to three regimes (**Figure 6b**):

1) Normal Marcus region for a small driving force ($0 < -\Delta G^{\circ} < \lambda$) in which the rate constant increases with increasing driving force;
2) Activationless region ($\lambda \approx -\Delta G^{\circ}$) in which there is no barrier for the reaction and the electron transfer rate reaches the maximum;
3) Inverted region ($\lambda < -\Delta G^{\circ}$) in which the rate constant decreases when driving force increases. The best experimental evidence for the existence of the inverted region was provided by Miller and Closs [38].

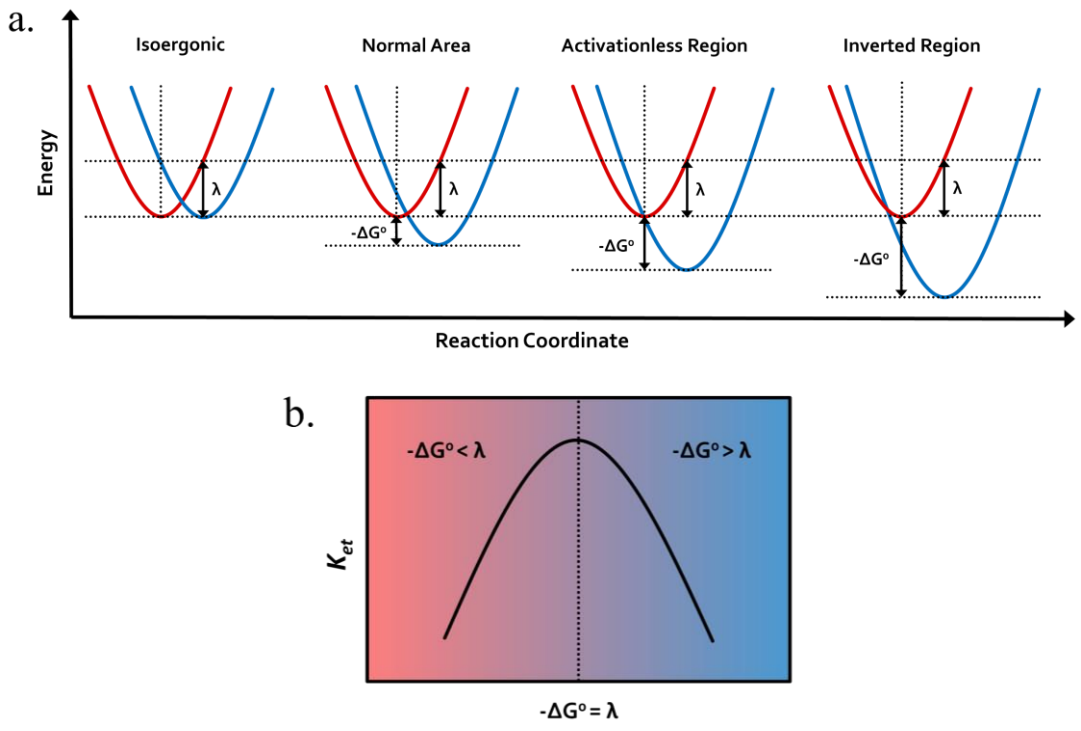

Figure 6. (a) Three regimes of Marcus parabola; (b) Marcus parabola showing the dependence of electron transfer rate on the reaction driving force.

The other important aspect of Marcus's work was his treatment of reorganization energy λ as the sum of a solvent independent internal term, λ_{inner}, and a solvent reorganization energy term, λ_{sol}. Thus,

$$\lambda = \lambda_{sol} + \lambda_{inner}$$

The inner-sphere reorganization comes from vibrations within the reactants which involves bond stretching and bending. It can be estimated from

$$\lambda_{inner} = \sum_i \left[\frac{f_i(R) f_i(P)}{f_i(R) + f_i(P)}\right] [\Delta q_i]^2$$

where Δq_i is the change of equilibrium bond distance from reactant state (R) to product state (P) for the *i*th vibration, and f_i is the force constant for the same vibration.

The modern development of computational chemistry allows scientists to calculate λ_{inner} for any donor-acceptor pair in a much easier way.

The solvation component is due to the reorganization of surrounding solvent which is regarded as a dielectric continuum, and it can be approximately calculated through the framework of a two-sphere model [35].

$$\lambda_{sol} = \frac{e}{4\pi\varepsilon_0}\left(\frac{1}{2r_{D^+}} + \frac{1}{2r_{A^-}} - \frac{1}{r_{D^+A^-}}\right)\left(\frac{1}{{n_s}^2} - \frac{1}{\varepsilon_s}\right)$$

where oxidized donor (D^+) and reduced acceptor (A^-) with radii r_{D^+} and r_{A^-} respectively are separated by the distance $r_{D^+A^-}$ in the solvent with a dielectric constant ε_s and a refractive index n_s.

However, the basic Marcus equation has its limitations. Since all internal and solvational vibrations modes are treated purely classically at low frequencies, it is only valid for the reactions where the potential surfaces are nonadiabatic with insignificant splitting at the intersection area; namely, the reactants are weakly coupled.

1.4.3 Semi-Classical Marcus-Jortner equation

In parallel with the development of the classical electron transfer theories, Levich and Dogonadze developed a treatment of solvent reorganization in a quantum mechanical approach based on Fermi's "golden rule" and Marcus equation [39-41].

Under the condition of high temperature ($h\nu < k_B T$), $FCWD$ can be approximated by

$$FCWD = \left(\frac{1}{4\pi\lambda k_B T}\right)^{1/2} \bullet exp\left[-\frac{(\Delta G^{\circ} + \lambda)^2}{4\lambda k_B T}\right]$$

Therefore, the rate of nonadiabatic electron transfer between a donor and an acceptor can be described giving the explicit dependence of the prefactor on V, λ, and T:

$$k_{et} = \left(\frac{\pi}{\hbar^2\lambda k_B T}\right)^{1/2} \bullet |V|^2 \bullet exp\left[-\frac{(\Delta G^{\circ} + \lambda)^2}{4\lambda k_B T}\right]$$

This "high-temperature limit" of semiclassical Marcus expression is mostly accurate for many room temperature electron transfer processes and has shown great success in modeling a wide range of experimental data. However, only low-frequency modes are taken into account in the term λ.

Later, Jortner and co-workers introduced a treatment of internal reorganization energy [42, 43]. In this theory, all high-frequency vibrations ($h\nu > k_B T$) involved in the initial state can be mixed and represented by a single averaged vibration with a frequency ν and the low-frequency medium vibrations ($h\nu_s \ll k_B T$) are still treated classically. Accordingly, the term reorganization energy λ can be divided into the reorganization energy of low-frequency motion of the solvent λ_{sol} and high-frequency vibrations of donor and acceptor λ_{inner}:

$$\lambda = \lambda_{inner} + \lambda_{sol}$$

The rate constant equation is given by

$$k_{et} = \left(\frac{\pi}{\hbar^2 \lambda_{sol} k_B T}\right)^{1/2} \bullet |V|^2 \bullet \sum_{w=0}^{\infty} \left[\frac{S^w}{w!} exp(-S)\right] \bullet exp\left[-\frac{(whv + \Delta G^\circ + \lambda_{sol})^2}{4\lambda_{sol} k_B T}\right]$$

where the summation is over the activation free energies leading into all the vibrational states, w, in the final state, and $S = \lambda_{inner}/hv$ is the Huang-Rhys factor which is the coupling of the high frequency mode to the electron transfer coordinate.

The Marcus-Jortner equation exhibits a maximum at $\Delta G^\circ \approx \lambda$. In the normal region ($-\Delta G^\circ < \lambda$), the equation above is represented very well by the "high-temperature limit" of semiclassical Marcus expression.

While considering the participation of intramolecular high-frequency vibrational modes in both initial and final states, Marcus and Sutin developed a semiclassical theory in which they also treated the solvent modes classically and the internal modes quantum mechanically (**Figure 7**) [36]. Thus, the Fermi's "golden rule" can be rewritten as the semiclassical Marcus equation:

$$k_{et} = \left(\frac{\pi}{\hbar^2 \lambda_{sol} k_B T}\right)^{1/2} \bullet |V|^2 \bullet \sum_j \sum_i \langle \chi_{Pj} | \chi_{Ri} \rangle^2 \, p(\epsilon_{Ri}) \bullet exp\left[-\frac{\left(\epsilon_{Pj} - \epsilon_{Ri} + \Delta G^0 + \lambda_{sol}\right)^2}{4\lambda_{sol} k_B T}\right]$$

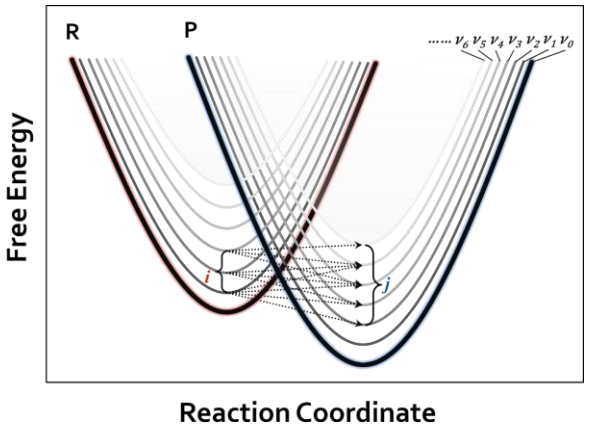

Figure 7. Potential energy diagram to describe radiationless transitions for electron transfer

process from a set of initial levels *i* in the reactant state to a set of levels *j* in the product state (not all transitions are included).

1.5 References

1. Kavarnos, G. J., Fundamental-Concepts of Photoinduced Electron transfer. *Top Curr Chem* **1990,** *156*, 21-58.

2. Sariciftci, N. S.; Smilowitz, L.; Heeger, A. J.; Wudl, F., Photoinduced Electron Transfer from a Conducting Polymer to Buckminsterfullerene. *Science* **1992,** *258* (5087), 1474-1476.

3. Yu, G.; Gao, J.; Hummelen, J. C.; Wudl, F.; Heeger, A. J., Polymer Photovoltaic Cells: Enhanced Efficiencies via a Network of Internal Donor-Acceptor Heterojunctions. *Science* **1995,** *270* (5243), 1789-1791.

4. Fabbrizzi, L.; Licchelli, M.; Pallavicini, P.; Perotti, A.; Taglietti, A.; Sacchi, D., Fluorescent Sensors for Transition Metals Based on Electron transfer and Energy Transfer Mechanisms. *Chemistry - A European Journal* **1996,** *2* (1), 75-82.

5. de Silva, A. P.; Gunaratne, H. Q. N.; Gunnlaugsson, T.; Huxley, A. J. M.; McCoy, C. P.; Rademacher, J. T.; Rice, T. E., Signaling recognition events with fluorescent sensors and switches. *Chem Rev* **1997,** *97* (5), 1515-1566.

6. Tvrdy, K.; Frantsuzov, P. A.; Kamat, P. V., Photoinduced electron transfer from semiconductor quantum dots to metal oxide nanoparticles. *P Natl Acad Sci USA* **2011,** *108* (1), 29-34.

7. Kamat, P. V., Manipulation of Charge Transfer Across Semiconductor Interface. A Criterion That Cannot Be Ignored in Photocatalyst Design. *J Phys Chem Lett* **2012,** *3* (5), 663-672.

8. Huang, J.; Stockwell, D.; Huang, Z. Q.; Mohler, D. L.; Lian, T. Q., Photoinduced ultrafast electron transfer from CdSe quantum dots to re-bipyridyl complexes. *J Am Chem Soc* **2008,** *130* (17), 5632-5633.

9. Deisenhofer, J.; Michel, H., The Photosynthetic Reaction Center from the Purple Bacterium Rhodopseudomonas viridis. *Science* **1989,** *245* (4925), 1463-1473.

10. Oneill, P.; Fielden, E. M., Primary Free-Radical Processes in DNA. *Adv Radiat Biol* **1993,** *17*, 53-120.

11. Lewis, F. D., Distance-Dependent Electron Transfer in DNA Hairpins. *Science* **1997,** *277* (5326), 673-676.

12. Fukui, K.; Tanaka, K., Distance dependence of photoinduced electron transfer in DNA. *Angew Chem Int Edit* **1998,** *37* (1-2), 158-161.

13. Lewis, F. D.; Letsinger, R. L.; Wasielewski, M. R., Dynamics of photoinduced charge transfer and hole transport in synthetic DNA hairpins. *Accounts Chem Res* **2001,** *34* (2), 159-170.

14. Kavarnos, G. J.; Turro, N. J., Photosensitization by reversible electron transfer: theories, experimental evidence, and examples. *Chem Rev* **1986,** *86* (2), 401-449.

15. Hannappel, T.; Burfeindt, B.; Storck, W.; Willig, F., Measurement of Ultrafast Photoinduced Electron Transfer from Chemically Anchored Ru-Dye Molecules into Empty Electronic States in a Colloidal Anatase TiO_2 Film. *The Journal of Physical Chemistry B* **1997,** *101* (35), 6799-6802.

16. Kraabel, B.; McBranch, D.; Sariciftci, N. S.; Moses, D.; Heeger, A. J., Ultrafast spectroscopic studies of photoinduced electron transfer from semiconducting polymers to C_{60}. *Phys Rev B* **1994,** *50* (24), 18543-18552.

17. Speiser, S., Novel Aspects of Intermolecular and Intramolecular Electronic-Energy Transfer in Solution. *J Photochem* **1983,** *22* (3), 195-211.

18. Turro, N. J.; Ramamurthy, V.; Scaiano, J. C. *Principles of Molecular Photochemistry: An Introduction*; University Science Publishers: New York, **2008**; pp 383-479.

19. Dexter, D. L., A Theory of Sensitized Luminescence in Solids. *The Journal of Chemical Physics* **1953,** *21* (5), 836-850.

20. Closs, G. L.; Johnson, M. D.; Miller, J. R.; Piotrowiak, P., A Connection between Intramolecular Long-Range Electron, Hole, and Triplet Energy Transfers. *J Am Chem Soc* **1989,** *111* (10), 3751-3753.

21. Aleksandr, K. C., Electron Transfer in Photochemical Reactions. *Russian Chemical Reviews* **1981,** *50* (7), 615.

22. Rehm, D.; Weller, A., Kinetik und Mechanismus der Elektronübertragung bei der Fluoreszenzlöschung in Acetonitril. *Berichte der Bunsengesellschaft für physikalische Chemie* **1969,** *73* (8-9), 834-839.

23. Landau, L., Zur Theorie der Energieübertragung. II. *Phys. Z. Sow* **1932**, 2 (46).

24. Zener, C., Non-Adiabatic Crossing of Energy Levels. *Proceedings of the Royal Society A: Mathematical, Physical and Engineering Sciences* **1932,** *137* (833), 696-702.

25. Balzani, V.; Bolletta, F.; Scandola, F., Vertical and Nonvertical Energy Transfer Processes - a General Classical Treatment. *J Am Chem Soc* **1980,** *102* (7), 2152-2163.

26. The distinct difference between adiabatic and nonadiabatic processes were discussed a lot in a) Sutin, N.; Eichhorn, G., Inorganic biochemistry. *by GL Eichhorn, Elsevier, Amsterdam* **1973,** *2*, 611; b) Marcus, R. A., Chemical and Electrochemical Electron-transfer Theory. *Annual Review of Physical Chemistry* **1964,** *15* (1), 155-196; c) Closs, G. L.; Miller, J. R., Intramolecular long-distance electron transfer in organic molecules. *Science* **1988,** *240* (4851), 440-447; d) Bixon, M.; Jortner, J., Electron Transfer—from Isolated Molecules to Biomolecules. In *Advances in Chemical Physics*, John Wiley & Sons, Inc.: **2007**; pp 17-18; e) Ceroni, P.; Balzani, V., Photoinduced energy and electron transfer processes. In *The exploration of supramolecular systems and nanostructures by photochemical techniques*, Springer: 2012; pp 21-38.

27. Closs, G. L.; Miller, J. R., Intramolecular long-distance electron transfer in organic molecules. *Science* **1988,** *240* (4851), 440-447.

28. Fermi, E., *Nuclear Physics*, University of Chicago Press: Chicago, **1950**.

29. Bolton, J. R.; Archer, M. D., Basic Electron-transfer Theory. **1991,** *228*, 7-23.

30. McConnell, H. M., Intramolecular Charge Transfer in Aromatic Free Radicals. *The Journal of Chemical Physics* **1961,** *35* (2), 508-515.

31. Libby, W. F., Theory of Electron Exchange Reactions in Aqueous Solution. *The Journal of Physical Chemistry* **1952,** *56* (7), 863-868.

32. Marcus, R. A., On the Theory of Oxidation-Reduction Reactions Involving Electron Transfer. I. *The Journal of Chemical Physics* **1956,** *24* (5), 966-978.

33. Marcus, R. A., Electrostatic Free Energy and Other Properties of States Having Nonequilibrium Polarization. I. *The Journal of Chemical Physics* **1956,** *24* (5), 979-989.

34. Marcus, R. A., Exchange reactions and electron transfer reactions including isotopic exchange. Theory of oxidation-reduction reactions involving electron transfer. Part 4. —A statistical-mechanical basis for treating contributions from solvent, ligands, and inert salt. *Discuss. Faraday Soc.* **1960,** *29* (0), 21-31.

35. Marcus, R. A., Chemical and Electrochemical Electron-transfer Theory. *Annual Review of Physical Chemistry* **1964,** *15* (1), 155-196.

36. Marcus, R. A.; Sutin, N., Electron transfers in chemistry and biology. *Biochimica et Biophysica Acta (BBA) - Reviews on Bioenergetics* **1985,** *811* (3), 265-322.

37. Marcus, R. A., Electron Transfer Reactions in Chemistry. Theory and Experiment. *Rev Mod Phys* **1993,** *65* (3), 599-610.

38. Miller, J. R.; Calcaterra, L. T.; Closs, G. L., Intramolecular long-distance electron transfer in radical anions. The effects of free energy and solvent on the reaction rates. *J Am Chem Soc* **1984,** *106* (10), 3047-3049.

39. Levich, V.; Dogonadze, R. In *Theory of the emissionless electron transitions between ions in solutions*, Doklady Acad Nauk USSR, **1959**; pp 123-126.

40. Levich, V., Present state of the theory of oxidation-reduction in solution (bulk and electrode reactions). *Advances in electrochemistry and electrochemical engineering* **1966,** *4*, 249-371.

41. Levich, V. G.; Dogonadze, R. R.; German, E. D.; Kuznetsov, A. M.; Kharkats, Y. I., Theory of homogeneous reactions involving proton transfer. *Electrochimica Acta* **1970,** *15* (2), 353-367.

42. Ulstrup, J.; Jortner, J., The effect of intramolecular quantum modes on free energy relationships for electron transfer reactions. *The Journal of Chemical Physics* **1975,** *63* (10), 4358-4368.

43. Jortner, J., Temperature dependent activation energy for electron transfer between biological molecules. *The Journal of Chemical Physics* **1976,** *64* (12), 4860-4867.

Chapter 2. Experimental Methods

This chapter outlines the main experimental methods which were utilized to characterize the electron transfer reactions in the dendron/linear pyrene-viologen systems and siderite and also the vibrational relaxation in the reduced methyl viologen. A detailed description of pump-probe techniques and spectroscopy is included.

2.1 Techniques and instruments

2.1.1 Steady-state absorption spectroscopy

All absorption spectra were collected at room temperature on a Cary 5000 UV–Vis–NIR spectrophotometer using a 10-mm quartz cuvette containing the sample. Absorption of pure solvent was recorded for baseline correction.

2.1.2 Fluorescence spectroscopy

Steady-state fluorescence spectra were measured on a Varian Cary Eclipse fluorimeter with the excitation and emission spectral slit widths of 5 nm. Fluorescence measurements of all pyrene-viologen dendrons were performed at the excitation wavelength of 325 nm. For reduced methyl viologen, the excitation spectrum was measured at the wavelength range of 300~400 nm.

2.1.3 Pump-probe spectroscopy

The electron transfer dynamics was measured by applying ultrafast pump-probe laser spectroscopy. The mode-locked Ti-sapphire oscillator (Spectra-Physics Tsunami),

which was pumped by a frequency-doubled CW Nd:VO_4 diode laser at 532 nm with 4.5 W of average power, produced 50 fs pulses centered at 795 nm. The pulses were stretched in time using dispersion so that the peak intensity was reduced in the process [1], which was followed by amplification in a home-built 1.25 kHz multipass amplifier (**Figure 1**). The output (500 mW) of the amplifier was split into two pulses: pump and probe. The pump pulses were directed into a noncollinear optical parametric amplifier (NOPA, Topas White, Light Conversion) and frequency doubled in a β-BBO crystal positioned in a second harmonic generator (SHG, Topas White, Light Conversion) to produce the pump beam which was used to excite the sample and initiate a chemical reaction of interest. During the measurements, the pump beam was delayed in time using a computer-controlled delay stage and modulated at 17 Hz with a mechanical chopper. The probe pulses passed through a 2-mm sapphire plate and generated white light continuum. The excitation beam and the white light continuum were focused with the help of a parabolic mirror and spatially overlapped in a 10-mm quartz cuvette containing the sample. The probe beam through the sample was dispersed with a monochromator (Oriel MS257) and detected by a Si photodiode (Thorlabs, DRT 110) (**Figure 2**).

The transient absorption spectra were recorded using a digital lock-in amplifier (Stanford Research, SR810) with the monochromator scanning the wavelength range and delay stage being fixed at a specific position. As for the measurements of kinetic profiles, the pump-probe delay time was scanned with the probe being fixed at a desired value.

In most cases, 8 scans were averaged to improve the signal-to-noise ratio. The relative polarization of the probe and pump beams was set at the “magic angle”.

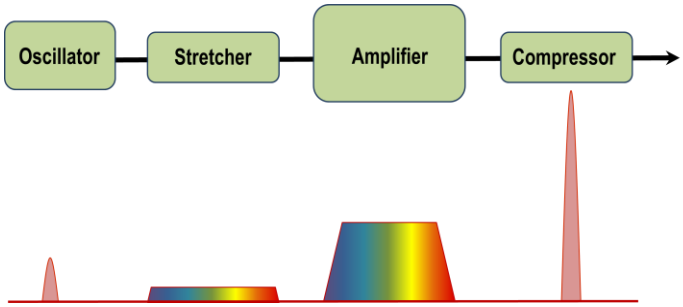

Figure 1. Diagram showing the chirped-pulse amplification process.

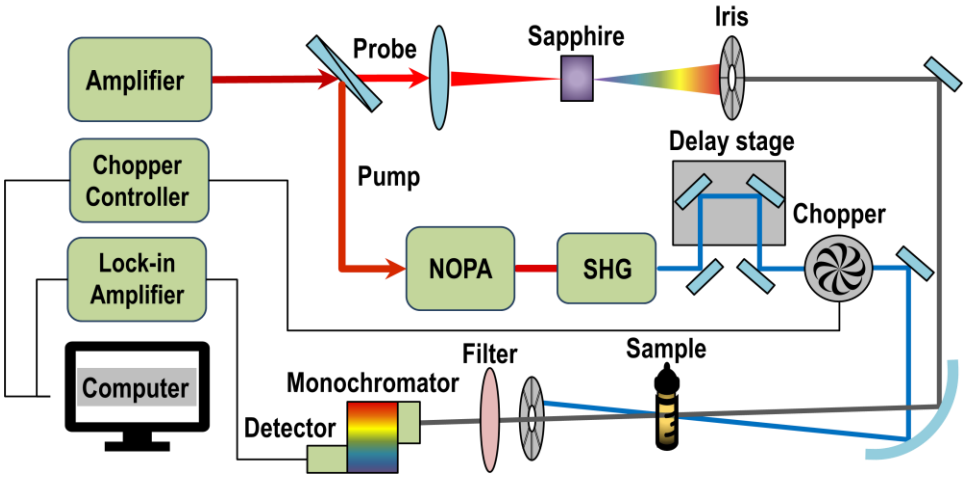

Figure 2. Scheme of the pump-probe experiment set-up

2.1.4 Theoretical calculations

2.1.4.1 Molecular orbital (MO) calculations

The calculations were carried out at the DFT B3LYP/6-31G* and AM1 semi-empirical levels using the Spartan'14 software package (Wavefunction, Inc.).

2.1.4.2 Molecular dynamics (MD) simulation calculation

The structure of P−C1−G0 together with two PF_6^- counter ions was optimized at the B3LYP/6-311+G* level of theory using Gaussian 03 program [2]. The minimized

P−C1−G0 was soaked into a cubic box with sizes of 45 Å filled with acetonitrile molecules. Subsequently, a 500-ps MD simulation was performed utilizing the TINKER package [3] with relaxing the solute and surrounding solvent molecules to obtain a well-solvated equilibrium system. All Lennard-Jones σ and ε parameters and electrostatic charges were taken from the OPLS-AA force field [4-7]. VMD [8] was used as a visualization program to make the MD video.

2.2 References

1. Reid, G. D.; Wynne, K., Ultrafast Laser Technology and Spectroscopy. **2006**.

2. Frisch, M. J.; Trucks, G. W.; Schlegel, H. B.; Scuseria, G. E.; Robb, M. A.; Cheeseman, J. R.; Montgomery, J. A.; Vreven, T.; Kudin, K. N.; Burant, J. C.; Millam, J. M.; Iyengar, S. S.; Tomasi, J.; Barone, V.; Mennucci, B.; Cossi, M.; Scalmani, G.; Rega, N.; Petersson, G. A.; Nakatsuji, H.; Hada, M.; Ehara, M.; Toyota, K.; Fukuda, R.; Hasegawa, J.; Ishida, M.; Nakajima, T.; Honda, Y.; Kitao, O.; Nakai, H.; Klene, M.; Li, X.; Knox, J. E.; Hratchian, H. P.; Cross, J. B.; Bakken, V.; Adamo, C.; Jaramillo, J.; Gomperts, R.; Stratmann, R. E.; Yazyev, O.; Austin, A. J.; Cammi, R.; Pomelli, C.; Ochterski, J. W.; Ayala, P. Y.; Morokuma, K.; Voth, G. A.; Salvador, P.; Dannenberg, J. J.; Zakrzewski, V. G.; Dapprich, S.; Daniels, A. D.; Strain, M. C.; Farkas, O.; Malick, D. K.; Rabuck, A. D.; Raghavachari, K.; Foresman, J. B.; Ortiz, J. V.; Cui, Q.; Baboul, A. G.; Clifford, S.; Cioslowski, J.; Stefanov, B. B.; Liu, G.; Liashenko, A.; Piskorz, P.; Komaromi, I.; Martin, R. L.; Fox, D. J.; Keith, T.; Laham, A.; Peng, C. Y.; Nanayakkara, A.; Challacombe, M.; Gill, P. M. W.; Johnson, B.; Chen, W.; Wong, M. W.; Gonzalez, C.; Pople, J. A., Gaussian 03, Revision C.02.

3. J.W. Ponder, P. Ren, R.V. Pappu, *et al.*, *TINKER–software tools for molecular design*, version 4.2 edn (Washington University School of Medicine, Washington, USA, 2004).

4. Jorgensen, W. L.; Maxwell, D. S.; TiradoRives, J., Development and testing of the OPLS all-atom force field on conformational energetics and properties of organic liquids. *J Am Chem Soc* **1996,** *118* (45), 11225-11236.

5. Kaminski, G. A.; Jorgensen, W. L., Host-guest chemistry of rotaxanes and catenanes: application of a polarizable all-atom force field to cyclobis(paraquat-p-phenylene) complexes with disubstituted benzenes and biphenyls. *J Chem Soc Perk T 2* **1999**, (11), 2365-2375.

6. Lopes, J. N. C.; Padua, A. A. H., Molecular force field for ionic liquids III: Imidazolium, pyridinium, and phosphonium cations; Chloride, bromide, and dicyanamide anions. *J Phys Chem B* **2006,** *110* (39), 19586-19592.

7. Price, M. L. P.; Ostrovsky, D.; Jorgensen, W. L., Gas-phase and liquid-state properties of esters, nitriles, and nitro compounds with the OPLS-AA force field. *J Comput Chem* **2001**, *22* (13), 1340-1352.

8. Humphrey, W., Dalke, A. and Schulten, K., "*VMD - Visual Molecular Dynamics*", J. Molec. Graphics, **1996**, vol. 14, pp. 33-38.

Chapter 3. Generation Dependent Ultrafast Charge Separation and Recombination in a Pyrene-methylene-viologen Family of Dendrons

This chapter gives an introduction of a pyrene-methylene-viologen dendron family in which the number of viologen subunits grows exponentially from P−C1−G0 to P−C1−G3. Their ability to intercept electrons and prolong the lifetime of a short-lived photoinduced charge-separated (CS) state was investigated by applying the femtosecond pump-probe spectroscopy. In this homologous family of donor-acceptor dendrons, the expansion of the viologen subunits introduces slower components to the recombination kinetics by allowing the injected electron to migrate further away from the donor. As a result, the fraction of long-lived population increases with 10-fold or greater lifetime extension in the order of P−C1−G3 > P−C1−G2 > P−C1−G1 > P−C1−G0, which can be interpreted in terms of the electron hopping between two viologen sites and long-range electron tunneling across multiple viologen units (**Scheme 1**).

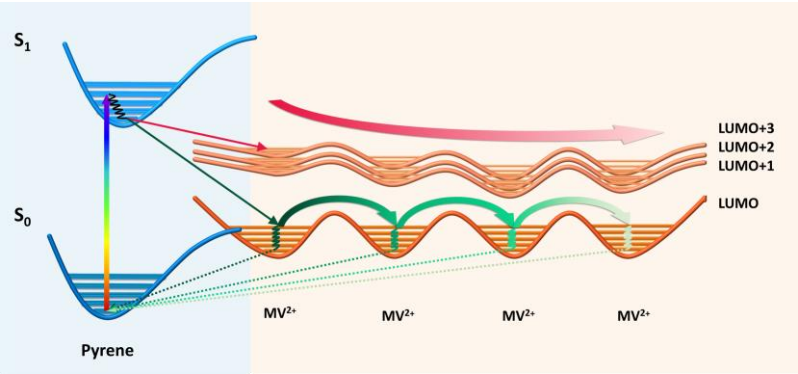

Scheme 1. Scheme of charge-transfer dynamics in pyrene-methylene-viologen dendrons. The bold red arrow represents the long-distance superexchange pathway, and the bold green arrows indicate sequential site-to-site electron hops.

3.1 Introduction

3.1.1 Dendrimers and dendrons

Dendrimers are cauliflower-shaped synthetic macromolecules which comprise of numerous layers of branched repeat units emanating from a single central core, in either a divergent or a convergent way. Dendrons, the simplified form of dendrimers, usually contain one chemically addressable group located at the focal point of the wedge-shaped dendritic fragment [1, 2] (**Figure 1**). Due to the uniqueness of tunable sizes and topologies via varying the number of generations and the chemistry of repeat units, dendrimers and dendrons are expected to exhibit adjustable electronic and optical properties, giving rise to potential applications in catalysis [3-6], nanotechnology [7-10], light harvesting [11-13] and drug or gene delivery [14-21].

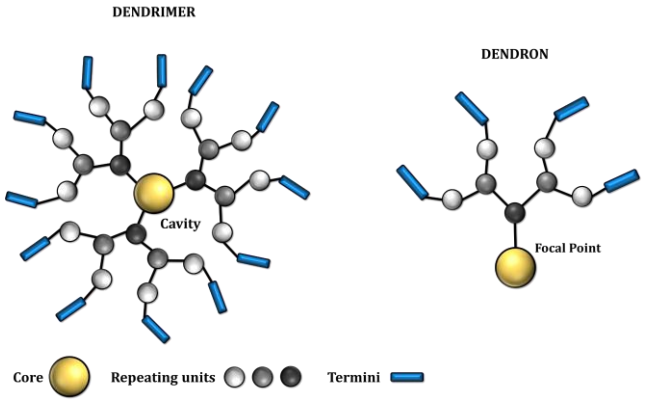

Figure 1. Representations of the general structure of a third-generation dendrimer and corresponding dendron formation with 1→2 connectivity.

3.1.2 Electron-transfer processes in dendrimers and dendrons

In dendrimer and dendron chemistry, the donor-acceptor dendritic systems, which usually consist of fully organic or mixed organic/metalorganic assemblies bearing photo-

active or redox-active functionalities, provide a powerful tool for detailed studies of electron-transfer reactions in versatile macromolecules and therefore play an important role in the promising research fields [2].

On the one hand, the synthetic approaches to dendrimers and dendrons have been very well developed, which allows scientists to accurately position the active groups at their central cores, branching points, termini and even cavities. Thus, the flow of excitons and electrons in the system can be controlled in a way that is not possible in corresponding linear polymers. On the other hand, experimental and theoretical chemists are dedicated to determining the electrochemical and electron-transfer kinetic parameters in order to investigate the influences of connectivity configuration [22], branching generation [23, 24], electronic coupling [25] and topological effect [26-28] on the electron propagation directions and rates in dendritic networks. Such synergy of the experimental and theoretical efforts leads to interesting and valuable insights.

3.1.3 Introduction of pyrene-methylene-viologen dendrons

Functionalization of dendrimers and dendrons with redox-active sites has been the subject of considerable researches since the resulting dendritic systems exhibit interesting properties in electron-transfer processes. Viologen (4,4’-bipyridinium salts) subunits are frequently involved in the synthesis of dendrimers and dendrons because of their well-known electrochromic properties [29] and their pronounced ability to accept electrons [30]. Walder *et al.* adopted both convergent and divergent approaches to prepare benzylic viologen dendrimers whose charge-transfer complexation with anionic dye molecules was guided through molecular recognition [31-33]. Kaifer *et al.* synthesized a series of

dendrimers containing a single redox-active viologen unit covalently attached to the apical position of a Newkome-type or Fréchet-type dendron, and the electrochemical results showed a decreasing trend of heterogeneous electron-transfer rates as the dendrimer size grows [28, 34-36]. Recently, Iyoda *et al.* fabricated the gold electrode with the dendritic viologen-arranged molecular arrays, which improved the electron transporting behavior on the metal surfaces and may lead to the application in molecular devices with tunable electric properties [37].

Pyrene, whose fluorescence properties are characterized by long excited-state lifetime and distinct solvatochromic shifts [38], is another popular functional subunit incorporated in the dendrimers and dendrons [39]. A series of dendrimers in which pyrene units are grafted at peripheries was prepared to afford light-harvesting antennae through the formation of intramolecular excimers [13, 40]. Moreover, the size-controlled pyrene-centered dendrimers showed adjustable photo- and electroluminescence properties, resulting in possible applications in organic light-emitting diode (OLED) devices [41-43].

In this project, a family of pyrene-methylene-viologen dendrons (up to third generation, **Scheme 2**) was successfully synthesized and characterized by mass spectroscopy, NMR, and electrochemistry. In these dendritic structures, the pyrene head group (Py) is attached to the apical viologen (V^{2+}) through a single methylene link (−C1−) and the number of viologen subunits continues to increase exponentially from P−C1−G0 to P−C1−G3 along with a growing number of hexafluorophosphate counterions (PF_6^-) which are used to minimize ion pairing effect and to promote solubility in most organic solvents. The studied pyrene-methylene-viologen dendrons are all donor-acceptor systems where the pyrene always serves as a light-absorbing electron donor and the branched

network of viologens acts as a hierarchical array of electron acceptors. The fanning out of the viologens makes it possible to build a unique system in which one electron donor and more than one acceptor are connected in a well-defined topology.

The main purpose of this project is to investigate the generation dependent capture of electrons produced by a short-lived photoinduced charge separated state formed at the apex of each dendron.

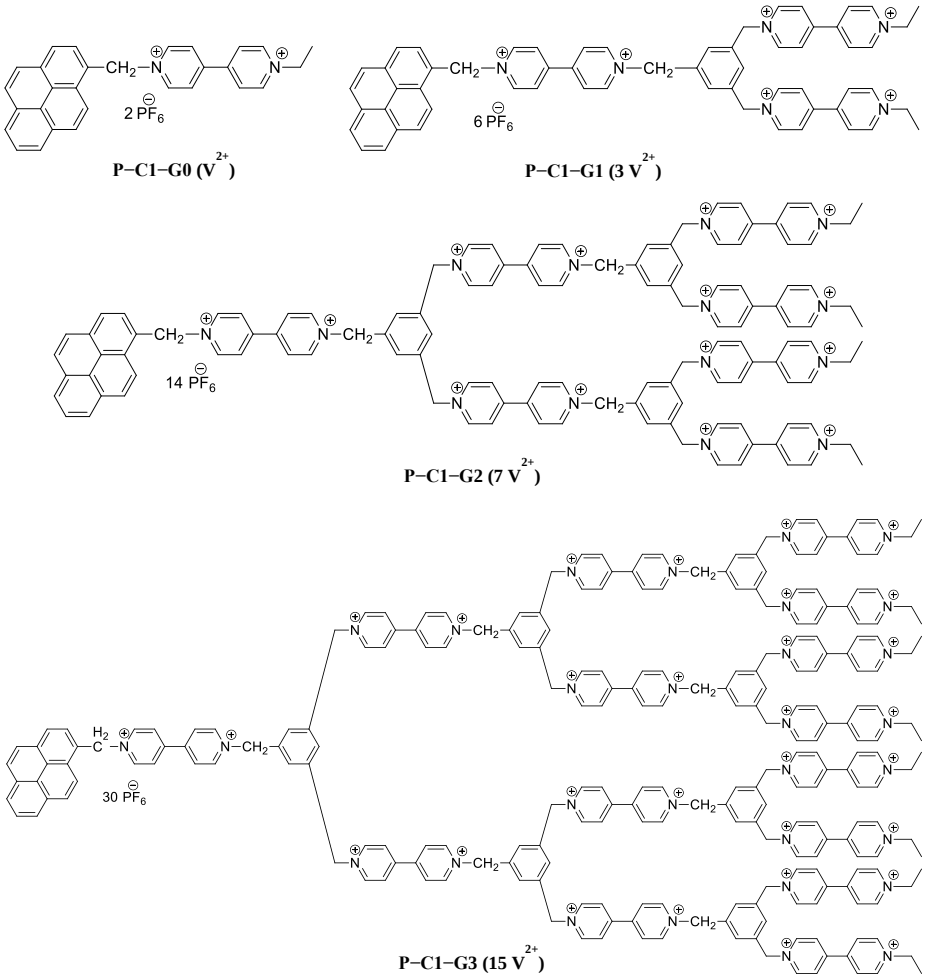

Scheme 2. Chemical structures of the pyrene-methylene-viologen dendron family. The number of viologen (V^{2+}) units grows exponentially from P−C1−G0 to P−C1−G3 and is indicated in parentheses.

3.1.4 Electron propagation in pyrene-methylene-viologen dendrons

The theoretical calculation of molecular orbital contributions of each subunit involved in the systems (**Scheme 3**) suggests the electron transfer from the photoexcited pyrene donor to the LUMO of the viologen acceptor and the subsequent electron migration across the dendritic network through a series of hops between adjacent viologen sites which are mediated and facilitated by mesitylene bridging units with low lying π-orbitals.

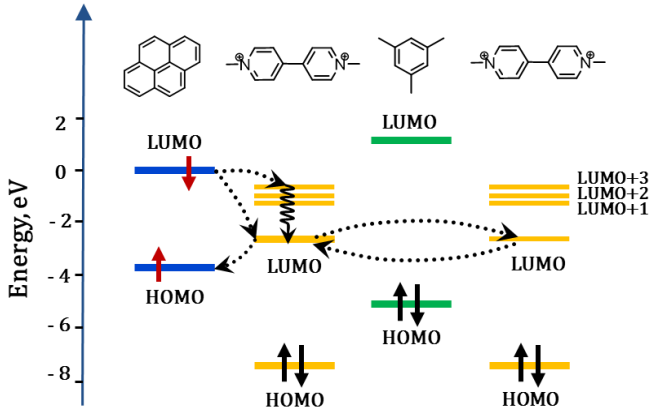

Scheme 3. A simplified energy level diagram of the components of the P−C1−$(V^{2+})_n$ dendrons. Note that several empty low-lying LUMO orbitals of each MV^{2+} lie below the LUMO of the pyrene.

For the P−C1−$(V^{2+})_{n=0,1,2,3}$ dendrons, the number of their branches is doubled each time it increases by a generation because of 1→2 connectivity. Thus, the probability of a forward electron hopping from any viologen site is $P_{fr} = \frac{1}{2}$. Whereas, the probability of a return hop is only $P_{back} = \frac{1}{4}$ because of the possibility of lateral hopping within the same shell of viologens. P_{back} grows to $\frac{1}{2}$ when the injected electron reaches a terminal viologen site. As a result, overall probability for the electron migration from periphery to the apex in the minimum possible number of moves decreases with increasing generation n as

$P_{total} = \frac{1}{2} \times (\frac{1}{4})^{n-1}$, which suggests a slower charge recombination rate as viologen branches expand. Therefore, an increased lifetime of the CS state is expected to be observed in higher generations.

3.2 Experimental methods

3.2.1 Synthesis

The dendrons were prepared via a microwave heating technique starting from a central pyrene and working out towards the methyl viologen peripheries (divergent synthesis). The general synthetic routes are shown in **Scheme 4**.

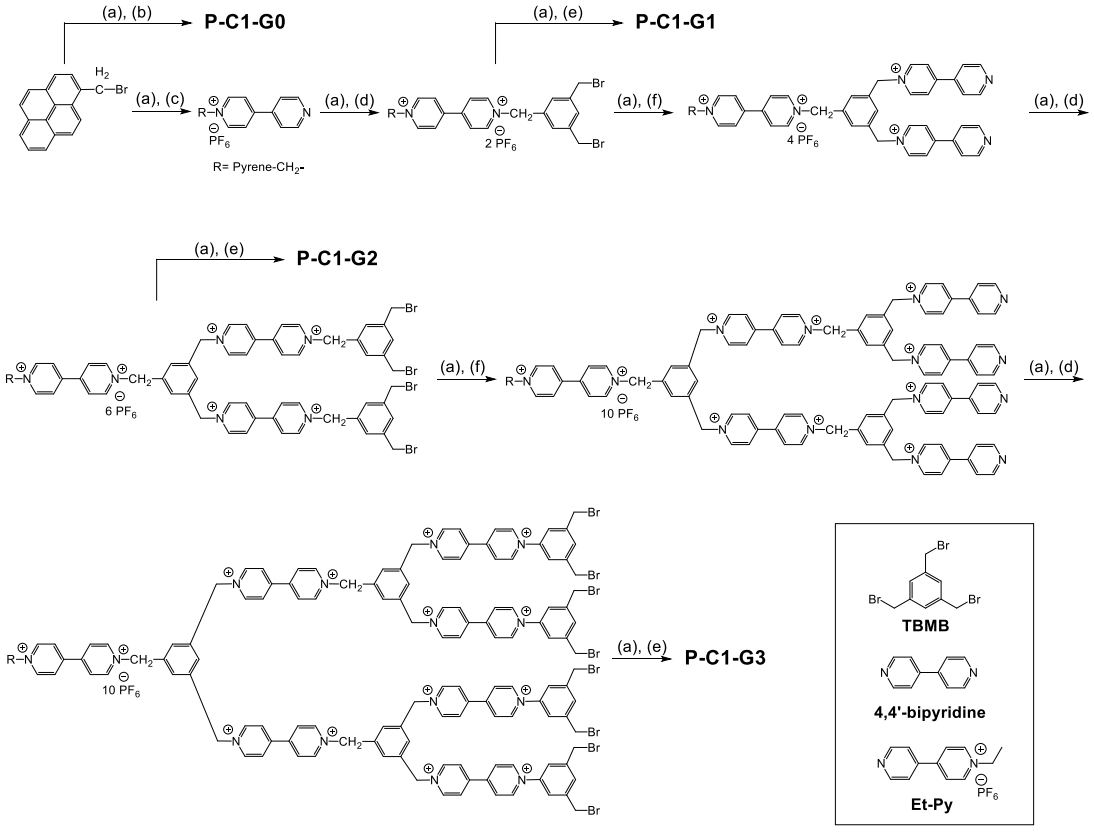

Scheme 4. Synthesis of P−C1−$(V^{2+})_n$ dendrons [37, 44]. (a) Saturated aqueous solution of NH_4PF_6. (b) 1-Ethyl-4-(4'-pyridyl) pyridinium hexafluorophosphate (Et-Py), 80 °C, 18 h. (c) 4'4-bipyridine,

microwave, 100 °C, 10 min. (d) 1,3,5-tris(bromomethyl)benzene (TBMB), microwave, 100 °C, 5 min. (e) Et-Py, microwave, 80 °C, 10 min. (f) 4'4-bipyridine, microwave, 80 °C, 10 min.

3.2.2 Sample preparation

Acetonitrile ($\geq$ 99.9 %, Fisher Scientific) was used without further purification. Samples for all the measurements were prepared by a similar method: Approximately 1.6 mg of each dendron was dissolved in 1 mL of solvent to obtain a series of concentrated solutions. Then, different amount of concentrated solution (20 μL of P−C1−G0, 50 μL of P−C1−G1, 110 μL of P−C1−G2, 225 μL of P−C1−G3) was pipetted into 3 mL of solvent for dilution separately. The concentration of all the samples was 1.5×10^{-5} M, as verified by their absorption spectra (**Figure 2a**). Finally, 3 mL of the solution was transferred into a standard quartz cuvette.

3.3 Results

3.3.1 Steady-state spectroscopy

The ground-state UV-Vis absorption spectrum of each pyrene-methylene-viologen dendron dissolved in aqueous acetonitrile (CH_3CN) at the concentration 1.5×10^{-5} M is shown in **Figure 2a**. In the ultraviolet region, the characteristic absorption of pyrene ranging from 310 to 340 nm is assigned to the $S_2 \leftarrow S_0$ transition and remains unchanged for all generations. The well-defined vibronic peak at 345 nm offers a convenient reference for determining and maintaining the molarity of dendrons in solution for all measurements. Since the strong absorption of methyl viologen lies in the wavelength range between 220 and 290 nm, it overlaps with the absorption of transitions to higher lying electronic states

of pyrene. As the number of viologen units grows, the contribution of absorbance from viologen moieties becomes more and more dominant. The $S_1 \leftarrow S_0$ transition of pyrene lies in the region from 350 to 370 nm, but only appears as a shoulder of the strong $S_2 \leftarrow S_0$ peak because of a vanishingly small extinction coefficient [45]. Overall, the spectra do not suggest aggregation or a major conformational change in the higher generation dendrons. The saturation of the viologen peak visible in the spectrum of P−C1−G3 occurs because the limit of the dynamic range of the spectrometer has been reached.

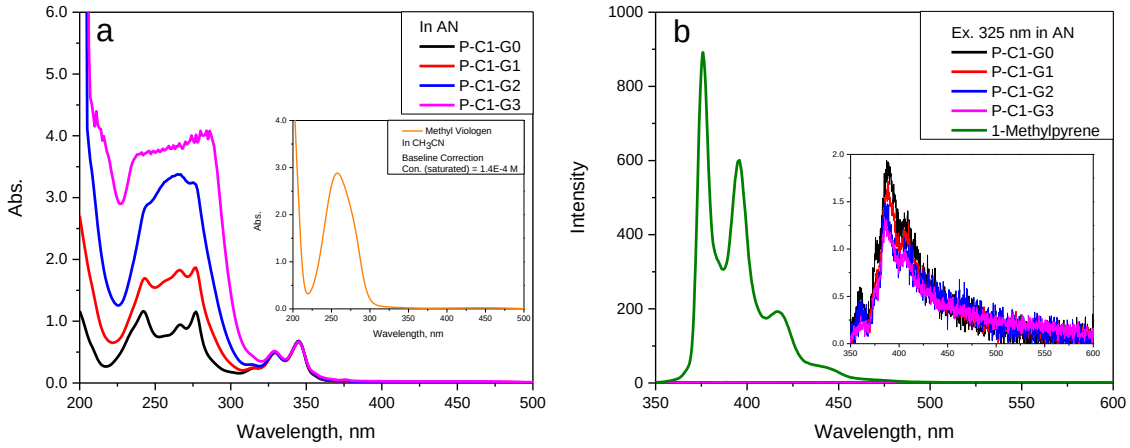

Figure 2. Steady state absorption (a) and fluorescence (b) spectra of P−C1−G0, P−C1−G1, P−C1−G2, and P−C1−G3 recorded at the concentration of 1.5×10^{-5} M in CH_3CN.

The fluorescence spectra (**Figure 2b**) of all dendrons, as well as 1-methylpyrene, were measured at room temperature with the excitation wavelength of 325 nm. For all dendrons, the characteristic intense fluorescence arising from the free pyrene is > 99.8 % quenched by the attached viologen unit(s), which suggests a very rapid electron-transfer process. Furthermore, their fluorescence spectra redshift by about 12 nm in comparison with that of 1-methylpyrene indicating the coupling interaction between pyrene and viologen. Additionally, the intensity of emission keeps falling off while increasing the

generation, implying a faster quenching through electron transfer in the higher generations of the dendron family due to the growing number of acceptor sites (**Figure 2b, inset**).

3.3.2 Transient absorption spectroscopy

The transient absorption spectrum of each pyrene-methylene-viologen dendron in acetonitrile was recorded at the time delay of 0.5 ps in the pump-probe experiment (**Figure 3**). For all generations, the photoexcitation at the 345 nm vibronic peak of pyrene to its S_2 state results in the very rapid formation of a CS state which occurs within the time resolution of our measurements, $\tau_{CS} < 100$ fs. It should be noted that pyrene possesses two closely lying excited singlet states and $S_2 \leftarrow S_1$ internal conversion occurs with a time constant of ~75 fs in unsubstituted pyrene [46]. The investigation of thermodynamic and kinetic parameters for pyrene-methylene-viologen dendrons is based on the energy level of the S_1 state. The possible direct involvement of the short-lived S_2 state of pyrene is difficult to examine due to the low extinction coefficient of the $S_0 \rightarrow S_1$ transition.

The rapid charge separation process is manifested by the instantaneous growing of two distinct transient absorption bands located at 420-470 nm and 500-700 nm, both of which are assigned to the generation of the chemical species resulting from the electron-transfer reaction. The absorption band with a sharp peak centered at 440 nm belongs to the oxidized pyrene ($Py^{\bullet+}$) [47] and the much broader absorption band peaking at 615 nm indicates the generation of the mono-reduced methyl viologen ($MV^{\bullet+}$) [48].

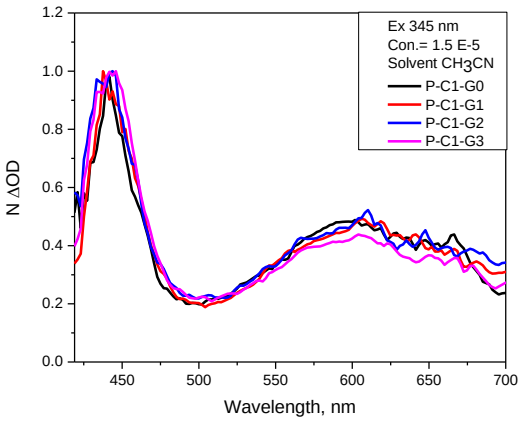

Figure 3. Normalized transient absorption spectra of the P−C1−G0, P−C1−G1, P−C1−G2, and P−C1−G3. All spectra were recorded at 0.5 ps delay following 345 nm excitation of 1.5×10^{-5} M solutions in CH_3CN. The 440 nm band is characteristic of $Py^{+\bullet}$ while the broad 615 nm band belongs to $MV^{+\bullet}$.

The kinetic profiles of $Py^{+\bullet}$ and $MV^{+\bullet}$ were collected at the probe wavelength of 440 and 615 nm separately in a 20 ps time window (**Figure 4a, b**). The resulting change of optical density, ΔOD, was analyzed by fitting the data after time zero to an exponential function (**Table 1, 2**).

3.3.3 Charge separation and recombination in P−C1−G0

The initial charge separation and electron-hole recombination at the junction between pyrene and the attached viologen unit at the apex are crucial for the overall electron transfer kinetics of all dendrons. Furthermore, the rates of these steps should be nearly identical in all generations. Therefore, it is of significance to understand the electron transfer dynamics in P−C1−G0.

The fitting results by applying a single exponential function of $\Delta OD(t) = A_1 e^{-t/\tau_1} + A_\infty$ for both dynamic traces of the $Py^{+\bullet}$ at 440 nm and $MV^{+\bullet}$ at 615 nm indicate

the very rapid charge recombination for oxidized pyrene and reduced viologen in P–C1–G0 with a time constant of $\tau_{CR} = \sim 0.7$ ps (**Table 1, 2**). The homogeneous decay is somewhat surprising because the pyrene and the viologen moiety can sample a broad range of dihedral angles which cannot be fully rotationally averaged within the sub-picosecond lifetime of the CS state. Therefore, it is concluded that the electronic coupling between donor and acceptor is relatively insensitive to the mutual orientation of the pyrene and viologen planes within a wide range of thermally-accessible conformer geometries.

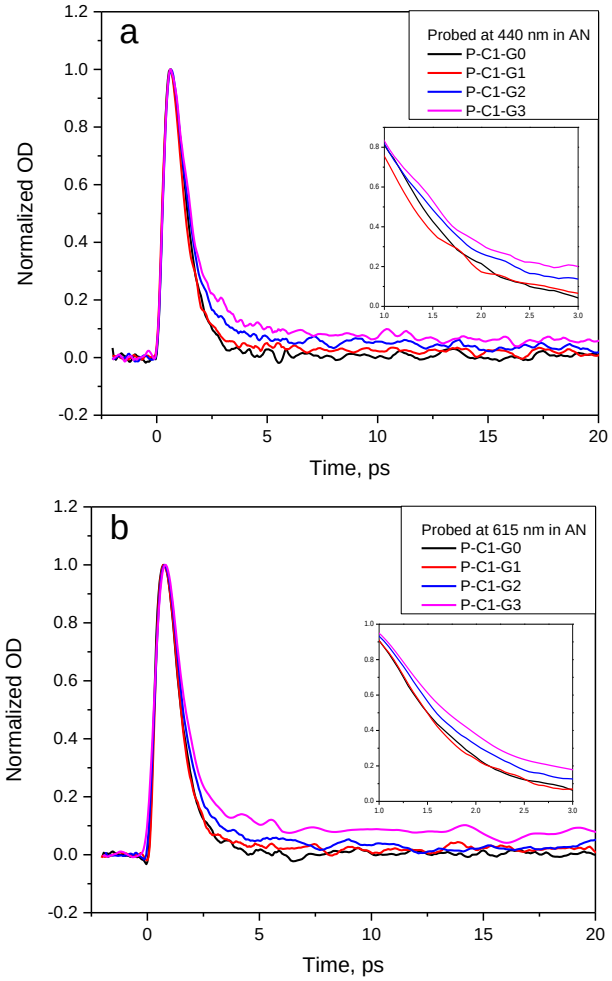

Figure 4. Transient absorption decay profiles recorded at (a) 440 nm, the absorption maximum of $Py^{+\bullet}$, and (b) 615 nm, the absorption maximum of $MV^{+\bullet}$.

The origin of such rapid charge separation and recombination rates in P−C1−G0 is rooted in its unique energetics of donor-bridge-acceptor framework. In most photoinduced electron-transfer systems, charge separation is mildly exoergic and lies in the Marcus "normal region", whereas the recombination dynamics is highly exoergic and buried deep in the "inverted region". However, in pyrene-methylene-viologen dendrons, the CS state locates nearly midway between the excited state of pyrene and the ground state of the system resulting from the exceptionally low reduction potential of the methyl viologen (~0.45 eV) [29]. The driving force for charge separation, $-\Delta G^{\circ}_{CS} = 1.7$ eV, and the recombination, $-\Delta G^{\circ}_{CR} = 1.6$ eV, are both greater than the reorganization energy, $\lambda_{CS} \cong \lambda_{CR} = 1.3$ eV, which determines the locations of both processes in the "inverted region" close to the "activationless region" where the maximum rate of electron transfer is achieved.

The estimate of the electronic coupling between $\mathrm{LUMO_{MV^{2+}}}$ and $\mathrm{HOMO_{Py}}$ associated with recombination rate constant of $1/\tau_{CR} = 1.4 \times 10^{12}\ \mathrm{s^{-1}}$ and the above thermodynamic parameters in the framework of the Marcus equation gives rise to a reasonable value of 120.1 $\mathrm{cm^{-1}}$. The reason why the charge separation rate in P−C1−G0 is remarkably faster than the recombination rate is because of a much stronger electronic coupling between $\mathrm{LUMO_{Py}}$ and $\mathrm{LUMO_{MV^{2+}}}$. Besides, there is a possibility that the charge separation is boosted by the involvement of three low-lying LUMOs of methyl viologen (**Scheme 3, Figure 5**). Each low-lying LUMO of methyl viologen can interact with the LUMO of pyrene and contributes to the overall charge separation rate.

In addition, since the charge separation process in P−C1−G0 is highly exoergic and completed within less than 100 fs, the system does not have enough time to reach the

thermal equilibrium and still retains part of the thermal excitation energy. In this case, the Marcus equation may lead to inaccurate predictions.

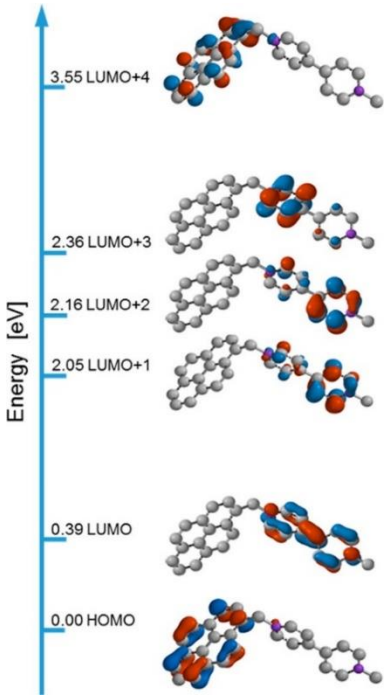

Figure 5. The low-lying molecular orbitals of P−C1−G0 which are involved in the charge separation and recombination. The energy is shown relative to the HOMO of pyrene (B3LYP, 6-31G*, in vacuum, Spartan' 14 by Wavefunction, Inc.).

3.3.4 Ion pairing

The charged viologen subunits in pyrene-methylene-viologen dendrons raise the possibility of ion pairing between viologen dications and PF_6^- counterions. It is known that the presence of counterions may stabilize the photoinduced CS states and slow the electron-transfer rates by introducing the ionic contribution to the overall reorganization energy and modulating the reaction driving force [49-52]. Even though a large body of work showed the ionic associations between viologen dications and numerous anionic solutes [53-55],

pronounced ion-pairing effects were mostly observed in the low polarity solvents with dielectric constants $\varepsilon_s < 10$. In acetonitrile, $\varepsilon_s = 36.6$, if there was ion pairing present, it would influence the electron-transfer dynamics and show a generation dependence on the concentration of viologen units and counterions from P−C1−G0 to P−C1−G3. In order to investigate this effect, pump-probe experiments were carried out on the 1.5×10^{-5} M P−C1−G0 solution containing 1.0 mM of tetrabutylammonium hexafluorophosphate ($NBu_4^+PF_6^-$) in CH_3CN. The transient absorption decays collected in the pure CH_3CN and the ones obtained in the solution where PF_6^- counterions were added in 30-fold excess are visually not distinct from one another (**Figure 6**), which suggests negligible ion-pairing effect at the employed dendron concentration of 1.5×10^{-5} M.

This result is supported by the reported association constant of $\overline{K}_a = 2.5 \times 10^3\ \mathrm{M}^{-2}$ for methyl viologen bis(hexafluorophosphate) in acetone, $\varepsilon_s = 20.7$ [56]. Applying this experimental value to the dendron systems, the ionic association ratio of viologens could be calculated and the resulting values ranges from 0.0002 % for P−C1−G0 to 0.05 % for P−C1−G3 indicating an extremely low degree of ion-pairing. In the more polar acetonitrile, the association constant must be even lower and ion-pairing effect should remain inappreciable under our experimental conditions.

In addition, the 500 ps MD simulation was performed on P−C1−G0 in a solvent box filled with acetonitrile molecules to visualize the diffusion dynamics of counterions. The trajectories were saved at 0.5 ps intervals. The snapshots captured in VMD (**Figure 7**) shows the rapid separation between PF_6^- counterions and the viologen subunit within 150 ps at 18 mM concentration of P−C1−G0, which further confirms that the ion-pairing effect is insignificant.

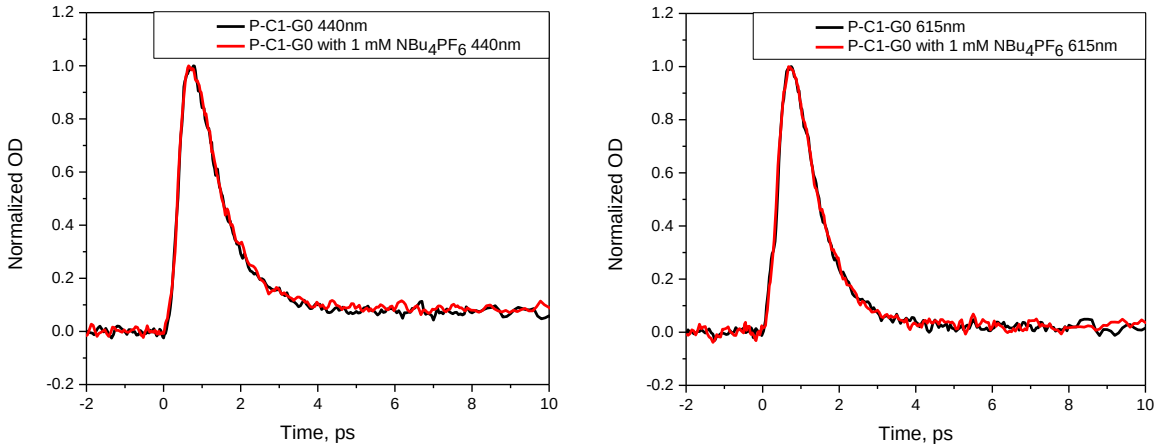

Figure 6. Kinetic profiles of P−C1−G0 probed at 440 nm (left) and 615 nm (right) detained in the pure CH_3CN (black) and in the presence of 1.0 mM of NBu_4PF_6 (red).

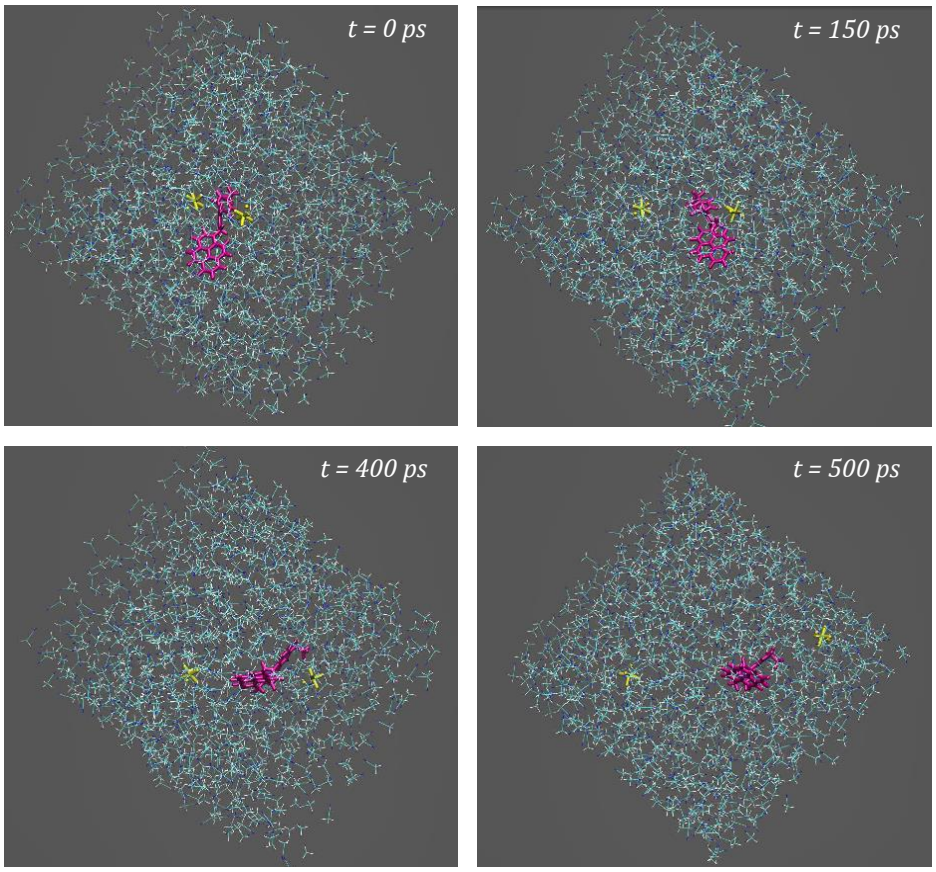

Figure 7. The 500 ps MD simulation of P−C1−G0 in acetonitrile was visualized in VMD, and four snapshots were captured at 0, 150, 400 and 500 ps. P−C1−G0 is marked with purple, and two PF_6^- counterions are shown in yellow.

3.3.5 Charge Separation and Recombination in P−C1−G1, P−C1−G2, and P−C1−G3

All charge recombination kinetic profiles of P−C1−G1, P−C1−G2, and P−C1−G3 were fitted with a double exponential function $\Delta OD(t) = A_1 e^{-t/\tau_1} + A_2 e^{-t/\tau_2} + A_\infty$ (**Figure 4**, **Table 1, 2**). As expected, the addition of viologen shells to the dendron leads to the appearance of longer lifetime components in the decay of the CS state. The behavior is evident both when the 440 nm band of $Py^{+\bullet}$ or the 615 nm band of $MV^{+\bullet}$ is monitored. In P−C1−G1, the first generation of the dendron, a slow component with time constant $\tau_2 =$ 6∼7 ps is observed. This value is approximately ten times slower than $\tau_{CR} =$ ∼0.7 ps detected in P−C1−G0, which indicates a 10-fold lifetime extension of the CS state. The slower component τ_2 can be interpreted either in terms of sequential hops between the adjacent viologen sites or a single step long-distance electron tunneling between pyrene and the second layer of viologens. Furthermore, a much longer-lived component, which is fitted as a constant A_∞, is also observed and persists for more than 20 ps time window in P−C1−G1. Together, the long-lived components, $A_2 + A_\infty$, constitute 3∼5 % of the initial population and can be ascribed to the electrons which escape the instantaneous recombination and migrate beyond the apical viologen site. The dominant component, decaying with $\tau_1 = 0.69$ ps, is assigned to the recombination at the apex and remains consistent with τ_{CS} in P−C1−G0.

Table 1. Fitting parameters for the decay of the $Py^{+\bullet}$ signal recorded at 440 nm.

Generation	τ_1, ps	A_1	τ_2, ps	A_2	A_∞	$A_2 + A_\infty$
P−C1−G0	0.71 ± 0.01	1.0	–	–	–	–
P−C1−G1	0.69 ± 0.01	0.955 ± 0.01	7.6 ± 1.8	0.027 ± 0.006	0.018 ± 0.002	0.05 ± 0.008
P−C1−G2	0.78 ± 0.01	0.905 ± 0.01	8.3 ± 0.9	0.064 ± 0.011	0.031 ± 0.002	0.10 ± 0.013
P−C1−G3	0.83 ± 0.02	0.874 ± 0.02	10.1 ± 2.9	0.081 ± 0.010	0.045 ± 0.008	0.13 ± 0.018

Table 2. Fitting parameters for the decay of the $MV^{+\bullet}$ signal recorded at 615 nm.

Generation	τ_1, ps	A_1	τ_2, ps	A_2	A_∞	$A_2 + A_\infty$
P−C1−G0	0.76 ± 0.01	1.0	–	–	–	–
P−C1−G1	0.69 ± 0.02	0.967 ± 0.01	6.1 ± 4.4	0.014 ± 0.009	0.019 ± 0.007	0.03 ± 0.016
P−C1−G2	0.72 ± 0.02	0.919 ± 0.01	5.2 ± 1.1	0.059 ± 0.010	0.022 ± 0.002	0.08 ± 0.012
P−C1−G3	0.78 ± 0.03	0.861 ± 0.01	9.0 ± 2.6	0.068 ± 0.011	0.071 ± 0.010	0.14 ± 0.021

As for P−C1−G2 and P−C1−G3, their capability to prolong the electron-hole recombination becomes more pronounced, which is reflected in the decreased decay rate constants of slow component and increased the long-lived population of the CS state. In order to treat the data in a consistent manner, all dynamic traces of higher generations were fitted using a double exponential function. In reality, new nonexponential terms will be introduced to the overall decay dynamics every time when an additional viologen shell is added into the dendron system. Overall, from P−C1−G0 to P−C1−G3, the fitting parameter τ_1 slightly changes in magnitude and always corresponds to the charge recombination for oxidized pyrene and attached reduced viologen. We attempted to fix $\tau_1 = \tau_{CS}$ before fitting so that the decay rates of fast the component would be identical in all generations, but this idea was abandoned due to lack of convergence. The slow component with a time constant τ_2 increases from 6 to 10 ps in an order of P−C1−G3 > P−C1−G2 > P−C1−G1 (**Table 1, 2**) indicating an electron-transfer process in which the injected electron travels further away from the apex and combines with the hole in donor through multiple itinerant hops to the apical viologen unit. The longest-lived component, A_∞, represents the fraction of radical ion species which does not decay appreciably within the measured time window and grows up to ~6 % in P−C1−G3. Accordingly, the total fraction of electrons $A_2 + A_\infty$, which escapes beyond the apical viologen site, keeps increasing from 4 % in P−C1−G1 to 9 % in P−C1−G2 and 13~14 % in P−C1−G3. This generation dependent growth in long-lived

population of CS state can be achieved either through a series of site-to-site electron hops between two viologen units or a direct long-distance electron tunneling from excited pyrene to the distant viologen sites especially to the ones in the second layer (**Scheme 1**, see **3.3.6**).

3.3.6 Discussion

The electron transfer dynamics in P−C1−G0 has been elaborated in the previous section (see **3.3.3**) focusing on the rapid charge separation and recombination at the apex. In this section, the plausible mechanisms which lead to the generation dependent growth of the long-lived population of the CS state in the extended dendrons are discussed.

The relative rate constant of charge recombination between pyrene and apical viologen, k_{CR}, and the electron hopping, k_{hop}, between degenerate viologens determines the decay pathway of the injected electron which is taken from pyrene and is located at the attached viologen site. Due to the highly exoergic charge recombination ($-\Delta G_{CR}^{\circ} = 1.6\ eV$), the electron hopping, as a hypothetical isoergic reaction, is a much slower process and not competitive. Based on the knowledge of energetics in P−C1−G0, the relationship of $k_{CS} > k_{CR} \gg k_{hop}$ can be derived. Therefore, the fraction of electrons which has an opportunity to migrate further down the dendron is remarkably low.

In P−C1−G1, only 4 % of the overall population of the CS state escapes from the instantaneous recombination, which predicts $k_{hop} \approx 4\,\% \cdot k_{CR} = 5.6 \times 10^{10}\ \mathrm{s}^{-1}$. However, this estimated value of k_{hop} is slower than the measured recombination rate of the slow component, $1/\tau_{2,G1} = 1.3\sim1.6 \times 10^{11}\ \mathrm{s}^{-1}$, which corresponds to the “round

trip" of electron hopping between first and second viologen shell. Furthermore, from the point of view of Marcus theory, the calculated $k_{hop} = 3.2 \times 10^5\ s^{-1}$ is six orders of magnitude slower than the experimental result. The electronic coupling for hopping, $|V_{hop}|$, equals half of the splitting between LUMOs of two viologen units in the model where two viologen substituents are symmetrically linked to the *meta* positions of the bridging benzene ring. The value of $|V_{hop}|$ ranges from ~30 cm^{-1} to ~100 cm^{-1} depending on the calculation method and corresponding basis set. The predicted k_{hop} increases to $3.6 \times 10^6\ s^{-1}$ at the maximum value when $|V_{hop}| = 100\ cm^{-1}$ but is still very slow. The reorganization energy $\lambda_{hop} = 1.35$ eV is the sum of the solvation component calculated through the Marcus two-sphere model and the intramolecular component (see **1.4.1**). Since the electron hopping occurs between two degenerate viologen sites, the driving force is assumed to be zero at this point and resulting activation free energy equals $\lambda_{hop}/4$.

These simple estimates may be prone to errors, but the discrepancy of several orders of magnitude warrants the consideration of other mechanisms which could allow the electrons reach further acceptor sites in the network.

Long-range electron tunneling, which allows the electron-transfer reactions to occur over distances larger than the sum of van der Waals radii of electron donor and the acceptor [57-60], would be the most obvious alternative path for populating distant viologen sites. It is known that an electron donor attached to a linear or branched array of acceptors is electronically coupled with all available acceptors [25, 61], not exclusively the one at the apex. Therefore, superexchange mediated tunneling from excited pyrene to distant viologen site is possible for higher generations. In most donor–$(bridge)_n$–acceptor

systems, according to McConnell's expression [62] for the rate constant $k_n \propto e^{-\beta n}$ where n is the number of bridging molecules and β is the attenuation parameter per repeat unit describing the efficiency of long-range coupling, the electron tunneling rate falls off exponentially with increasing the separation of reacting partners. In pyrene-methylene-viologen dendrons, since the number of acceptors increases by 2^n as one viologen shell is added to generate a nth-generation dendron, the dependence of long-range tunneling rate on the electron coupling is weaken, and the resulting rate constant is proportional to $e^{-\beta n} \times 2^n$. The equivalent expression can be written into $k_n/k_0 = e^{-\beta n} \times 2^n$ [63] and plotted in **Figure 8** which shows the relative electron tunneling rates against the generation for a dendron family with 1→2 connectivity as well as for a series of linear donor-(bridge)$_n$-acceptor diads as a contrast. It is evident that the involvement of multiple acceptors can enhance the long-range electron tunneling rate over a certain donor-acceptor distance even for a large attenuation factor β.

While considering the electron tunneling from excited state of pyrene to the second layer of viologens in P−C1−G1, the calculated electronic coupling equals 31.9 cm^{-1} by applying $\bar{k}_{CR,G1} = 1/\bar{\tau}_{2,G1} = 1.47 \times 10^{11}$ s^{-1} in the Marcus equation, and this value is reasonable considering the partially conjugated nature of the mesitylene bridges [64].

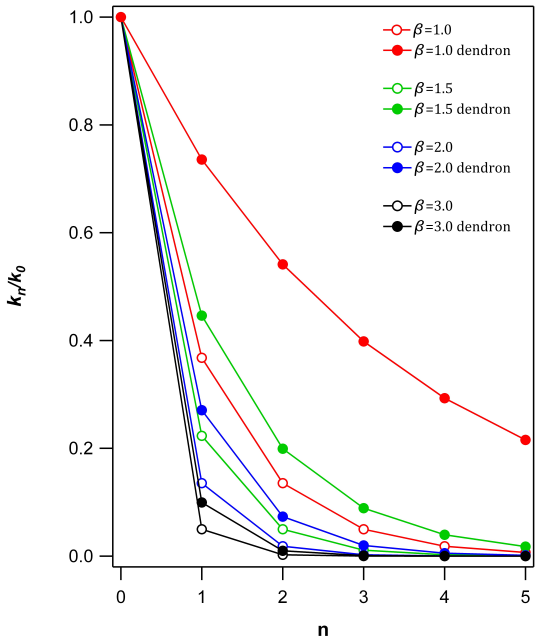

Figure 8. The relative electron tunneling rates against the number of repeat units *n* in a 1→2 dendron family (solid dots) and in a series of linear donor-(bridge)$_n$-acceptor diads (circles) under the condition of variable attenuation factors of 1.0 (red), 1.5 (green2.0 (blue) and 3.0 (black).

Furthermore, the additive relative rate of electron transfer in a n th-generation dendron, $k_{tot}/k_0 = 1 + \sum_{n=1}^{n} e^{-\beta n} \times 2^n$, is plotted in **Figure 9**. The distinct contrast between dendrons and linear donor-(bridge)$_n$-acceptor diads indicates that increasing the effective concentration of acceptors can efficiently promote the depopulation of the initial excited state of the donor, which explains the generation dependent growth of the long-lived fraction of the CS states. This is also consistent with the result extracted from the fluorescence spectra of pyrene-methylene-viologen dendrons. The residual emission of pyrene moiety continuously diminishes with increasing the generation, suggesting the probability of direct electron transfer from excited donor to the growing number of acceptor sites (**Figure 2b, inset**).

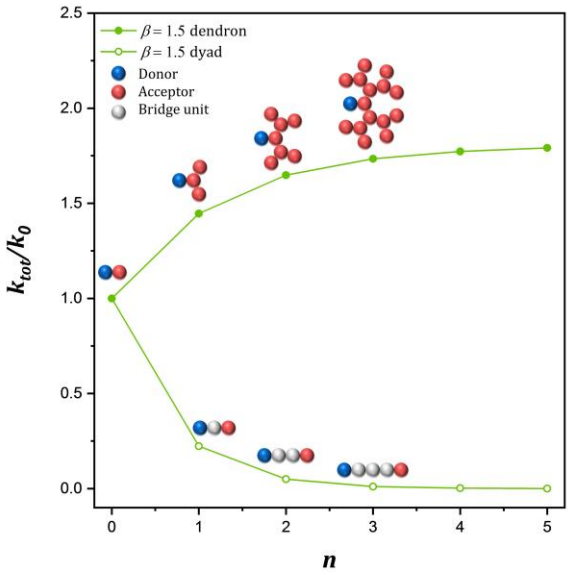

Figure 9. The total relative rates of forward electron transfer plotted against the number of repeat unit n in a 1→2 dendron family (solid dots) and in a series of linear donor-(bridge)$_n$-acceptor diads (circles) when the attenuation factor β equals 1.5.

In pyrene-methylene-viologen dendrons, the extremely rapid photoinduced electron transfer occurring with a high driving force results in a "hot" CS state with large excess energy, which is likely to benefit both electron hopping and long-range electron tunneling significantly. The large excess energy must be distributed between the donor and the acceptor and eventually dissipated into the surrounding medium. It is known that excited states of $MV^{+\bullet}$ may be generated as an initial product upon electron transfer to MV^{2+}. The D_1 state of $MV^{+\bullet}$ has a lifetime of 700 fs and decays with the formation of the vibrationally hot ground state which is completely relaxed on a slower up to 16 ps time scale [65]. Since the charge recombination between $Py^{+\bullet}$ and the apical $MV^{+\bullet}$ is completed with $\tau_{CR} = 0.72$ ps, the first-time electron hop from the apical $MV^{+\bullet}$ competes with vibrational relaxation process and necessarily occurs with the residual vibrational excitation. As a result, the actual hopping rate should be much faster than that given by

Marcus theory in which the reacting system is assumed to be fully solvated and $-\Delta G^{\circ}_{Hop} = 0$. This finding is of significance because it suggests a greater probability for the injected electron to avoid the initial charge recombination and travel further away from the excited donor, even though it is true that the vibrational excitation steeply drops off in the following hops. If the large excess energy is equally assigned to $Py^{+\bullet}$ and attached $MV^{+\bullet}$, the resulting $0.85\ eV$ of vibrational excitation in $MV^{+\bullet}$ gives rise to $k_{hop} = 3.2 \times 10^{10} \sim 3.6 \times 10^{11}\ s^{-1}$, which is sufficient to intercept ~ 15 % of the initial CS state population. In addition, the viologen-mesitylene-viologen framework is partially delocalized and should further promote the electronic coupling between LUMOs of two viologen sites.

It should be noted that the higher generations in the pyrene-methylene-viologen dendron family are polycations bearing positive charges at each viologen site. The interaction of these positive charges in a specific dendritic network would lead to an electric field which changes the electron affinity of the individual acceptor site. Therefore, the landscape of $-\Delta G^{\circ}$ determined by the number of viologen shells is not expected to be smooth. This notion is supported by the result of cyclic voltammograms (CV) characterization on a family of dendritic viologen-arranged molecules conducted by Iyoda *et al*. This group reported a decreasing trend of half-wave potential for the first reduction process of viologen subunits ($E_{V^{2+}/V^{+\bullet}}$) from -0.406 V vs. SCE for the first generation to -0.390 V for the third generation [37]. A more pronounced deceasing trend of $E_{V^{2+}/V^{+\bullet}}$ was observed in a series of viologen dendrimers from -0.355 V for G0 carrying 3 viologen subunits to -0.299 V for G3 containing 30 viologens [31]. AM1 and DFT calculations using the Spartan program show that adding one viologen layer lowers the energy of LUMOs of all preceding shells, which are consistent with those reported electrochemical results. In

addition, the electrostatic potential map illustrates the charge distribution in P−C1−G3 suggesting a boat-like shape of the ΔG° profile (**Figure 10**). Acceptors in the $(n-1)_{th}$ shell exhibit the strongest electron affinity, whereas, the apical and terminal ones are least favored sites for the injected electron. The descending gradient of driving force facilitates the injected electron to migrate away from the apex and slows the returning rate. Although the computational calculations were performed under the condition of vacuum where the magnitude of the field effect was exaggerated, they were useful in qualitative analysis.

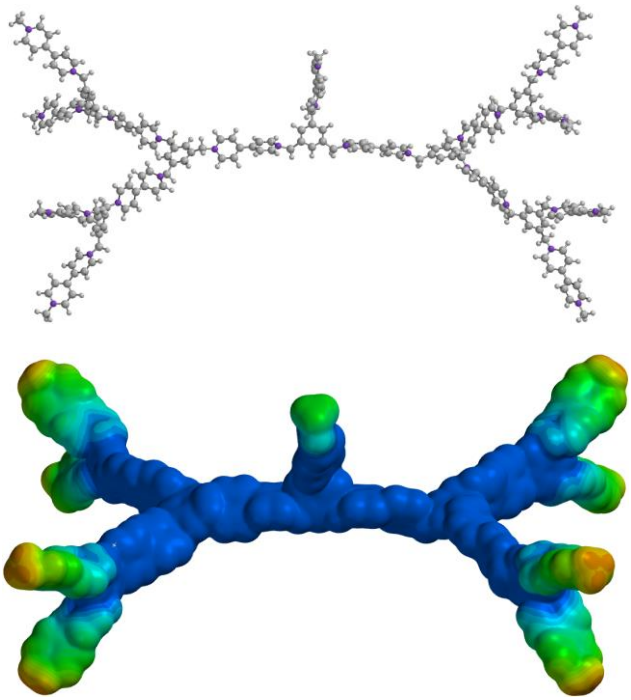

Figure 10. Surface electrostatic potential map of P−C1−G3 in vacuum (AM1, Spartan '14 by Wavefunction, Inc.). The pyrene head group at the apex is not shown. Low potential areas marked with red indicates a high electron density, whereas the high potential areas marked with blue are characterized by a low electron density.

Lastly, the polycation nature of the dendron also influences the solvent reorganization energy of electron hopping. For outer-sphere electron transfer, all

calculations of λ_s are based on the generalized Born model in which the full solvation of an ion in a dielectric continuum is viewed as resulting from the Coulomb interaction of the ionic charge with the polarization of the surrounding medium regardless of the local structure and nearby charged species. Since the excluded solvent volume increases as the size of dendron grows, it is impossible for each viologen to maintain its own infinite solvation sphere considering the influence from other charged repeat subunits in the network. To verify this effect, the more sophisticated SM8 model of acetonitrile used in conjunction with B3LYP DFT optimization [66] was used to calculate the free energies of solvation of all dendrons, and the results indicated a $\sim 5\,\%$ reduction of the average solvation energy per viologen site as the number of repeat units grows from P−C1−G0 to P−C1−G3. Therefore, the activation free energy $\Delta G^{\neq} \approx \lambda_{hop}/4$ is likely to be overestimated, and the resulting solvation barrier for electron hopping is actually not quite as high as that predicted by the Born model.

3.4 Conclusions

In this chapter, the electron transfer dynamics in a pyrene-methylene-viologen dendron family was investigated applying femtosecond pump-probe experiments. The extended dendritic networks with multiple acceptor sites favor the injected electron to travel away from the apex and demonstrate the ability to prolong the lifetime of a short-lived photoinduced CS state, which is firstly attributed to a sequence of site-to-site electron hops among viologen units. However, the “hopping” mechanism cannot completely account for the increasing fraction of electrons that escape beyond the apical viologen as the generation grows, and the value of hopping rate predicted by Marcus theory is several

orders of magnitude slower than that derived from the experimental results. Then, the "long-range electron tunneling" mechanism is proposed, which allows the direct electron transfer to the growing number of distant acceptor sites and promotes the depopulation of the initial excited-state of the donor. The dominant mechanism is determined by the corresponding electronic couplings and activation barriers. Both electron hopping and long-distance electron tunneling benefit from the extremely rapid charge separation with a high driving force which produces a "hot" CS state and deposits a large excess energy in both pyrene and the first viologen. The considerable vibrational excitation of the apical viologen unit facilitates the following hops and diminishes as the number of hopping steps increases. Therefore, the Marcus prediction based on the assumption of absolutely isoergic and fully thermally equilibrated hopping process is not realistic and accurate. In addition, the polycation nature of the higher generations affords a boat-like shape of ΔG° profile which favors the electron hopping further down into the network. Furthermore, it lowers the activation energy of electron hopping by reducing the average solvation energy of each viologen unit in the dendrons.

3.5 References

[1] Abbasi, E.; Aval, S. F.; Akbarzadeh, A.; Milani, M.; Nasrabadi, H. T.; Joo, S. W.; Hanifehpour, Y.; Nejati-Koshki, K.; Pashaei-Asl, R., Dendrimers: synthesis, applications, and properties. *Nanoscale Res Lett* **2014,** *9*.

[2] Astruc, D., Electron-transfer processes in dendrimers and their implication in biology, catalysis, sensing and nanotechnology. *Nat Chem* **2012,** *4* (4), 255-267.

[3] Zhao, M. Q.; Crooks, R. M., Homogeneous hydrogenation catalysis with monodisperse, dendrimer-encapsulated Pd and Pt nanoparticles. *Angew Chem Int Edit* **1999,** *38* (3), 364-366.

[4] Oosterom, G. E.; Reek, J. N. H.; Kamer, P. C. J.; van Leeuwen, P. W. N. M., Transition metal catalysis using functionalized dendrimers. *Angew Chem Int Edit* **2001,** *40* (10), 1828-1849.

[5] Crooks, R. M.; Zhao, M.; Sun, L.; Chechik, V.; Yeung, L. K., Dendrimer-Encapsulated Metal Nanoparticles: Synthesis, Characterization, and Applications to Catalysis. *Accounts of Chemical Research* **2001,** *34* (3), 181-190.

[6] Astruc, D.; Chardac, F., Dendritic catalysts and dendrimers in catalysis. *Chem Rev* **2001,** *101* (9), 2991-3023.

[7] Balogh, L.; Tomalia, D. A., Poly(Amidoamine) Dendrimer-Templated Nanocomposites. 1. Synthesis of Zerovalent Copper Nanoclusters. *Journal of the American Chemical Society* **1998,** *120* (29), 7355-7356.

[8] Fréchet, J. M. J., Dendrimers and other dendritic macromolecules: From building blocks to functional assemblies in nanoscience and nanotechnology. *Journal of Polymer Science Part A: Polymer Chemistry* **2003,** *41* (23), 3713-3725.

[9] Scott, R. W. J.; Wilson, O. M.; Crooks, R. M., Synthesis, Characterization, and Applications of Dendrimer-Encapsulated Nanoparticles. *The Journal of Physical Chemistry B* **2005,** *109* (2), 692-704.

[10] Shi, X. Y.; Ganser, T. R.; Sun, K.; Balogh, L. P.; Baker, J. R., Characterization of crystalline dendrimer-stabilized gold nanoparticles. *Nanotechnology* **2006,** *17* (4), 1072-1078.

[11] Stewart, G. M.; Fox, M. A., Chromophore-labeled dendrons as light harvesting antennae. *Journal of the American Chemical Society* **1996,** *118* (18), 4354-4360.

[12] Gilat, S. L.; Adronov, A.; Frechet, J. M. J., Light harvesting and energy transfer in novel convergently constructed dendrimers. *Angew Chem Int Edit* **1999,** *38* (10), 1422-1427.

[13] Adronov, A.; Fréchet, J. M. J., Light-harvesting dendrimers. *Chemical Communications* **2000,** (18), 1701-1710.

[14] Tang, M. X.; Redemann, C. T.; Szoka, F. C., In vitro gene delivery by degraded polyamidoamine dendrimers. *Bioconjugate Chem* **1996,** *7* (6), 703-714.

[15] Liu, M. J.; Frechet, J. M. J., Designing dendrimers for drug delivery. *Pharm Sci Technol To* **1999,** *2* (10), 393-401.

[16] Esfand, R.; Tomalia, D. A., Poly(amidoamine) (PAMAM) dendrimers: from biomimicry to drug delivery and biomedical applications. *Drug Discov Today* **2001,** *6* (8), 427-436.

[17] Patri, A. K.; Majoros, I. J.; Baker, J. R., Dendritic polymer macromolecular carriers for drug delivery. *Curr Opin Chem Biol* **2002,** *6* (4), 466-471.

[18] Gillies, E. R.; Frechet, J. M. J., Dendrimers and dendritic polymers in drug delivery. *Drug Discov Today* **2005,** *10* (1), 35-43.

[19] Patri, A. K.; Kukowska-Latallo, J. F.; Baker, J. R., Targeted drug delivery with dendrimers: Comparison of the release kinetics of covalently conjugated drug and non-covalent drug inclusion complex. *Adv Drug Deliver Rev* **2005,** *57* (15), 2203-2214.

[20] Dufes, C.; Uchegbu, I. F.; Schatzlein, A. G., Dendrimers in gene delivery. *Adv Drug Deliver Rev* **2005,** *57* (15), 2177-2202.

[21] Pan, B. F.; Cui, D. X.; Sheng, Y.; Ozkan, C. G.; Gao, F.; He, R.; Li, Q.; Xu, P.; Huang, T., Dendrimer-modified magnetic nanoparticles enhance efficiency of gene delivery system. *Cancer Res* **2007,** *67* (17), 8156-8163.

[22] Cardona, C. M.; Kaifer, A. E., Asymmetric redox-active dendrimers containing a ferrocene subunit. Preparation, characterization, and electrochemistry. *Journal of the American Chemical Society* **1998,** *120* (16), 4023-4024.

[23] Hong, Y. R.; Gorman, C. B., Attenuating electron-transfer rates via dendrimer encapsulation: The case of metal tris(bipyridine) core dendrimers. *Langmuir* **2006,** *22* (25), 10506-10509.

[24] Vogtle, F.; Plevoets, M.; Nieger, M.; Azzellini, G. C.; Credi, A.; De Cola, L.; De Marchis, V.; Venturi, M.; Balzani, V., Dendrimers with a photoactive and redox-active [Ru(bpy)(3)](2+)-type core: Photophysical properties, electrochemical behaviour, and excited-state electron-transfer reactions. *Journal of the American Chemical Society* **1999,** *121* (26), 6290-6298.

[25] Risser, S. M.; Beratan, D. N.; Onuchic, J. N., Electronic Coupling in Starburst Dendrimers - Connectivity, Disorder, and Finite-Size Effects in Macromolecular Bethe Lattices. *J Phys Chem-Us* **1993,** *97* (17), 4523-4527.

[26] Elicker, T. S.; Binette, J.-S.; Evans, D. G., Topological Effects in Electron Transfer: Applications to Dendrimers and Branched Molecules. *The Journal of Physical Chemistry B* **2001,** *105* (2), 370-378.

[27] Gorman, C. B.; Smith, J. C.; Hager, M. W.; Parkhurst, B. L.; Sierzputowska-Gracz, H.; Haney, C. A., Molecular structure-property relationships for electron-transfer rate

attenuation in redox-active core dendrimers. *Journal of the American Chemical Society* **1999,** *121* (43), 9958-9966.

[28] Kaifer, A. E., Electron transfer and molecular recognition in metallocene-containing dendrimers. *Eur J Inorg Chem* **2007,** (32), 5015-5027.

[29] Monk, P. M. S., *The viologens: physicochemical properties, synthesis, and applications of the salts of 4,4'-bipyridine*. Wiley: Chichester; New York, 1998.

[30] Marchioni, F.; Venturi, M.; Credi, A.; Balzani, V.; Belohradsky, M.; Elizarov, A. M.; Tseng, H. R.; Stoddart, J. F., Polyvalent scaffolds. Counting the number of seats available for eosin guest molecules in viologen-based host dendrimers. *Journal of the American Chemical Society* **2004,** *126* (2), 568-573.

[31] Heinen, S.; Walder, L., Generation-dependent intramolecular CT complexation in a dendrimer electron sponge consisting of a viologen skeleton. *Angew Chem Int Edit* **2000,** *39* (4), 806-809.

[32] Heinen, S.; Meyer, W.; Walder, L., Charge trapping in dendrimers with a viologen skeleton and a radial redox gradient. *J Electroanal Chem* **2001,** *498* (1-2), 34-43.

[33] Murugavel, K., Benzylic viologen dendrimers: a review of their synthesis, properties and applications. *Polym Chem-Uk* **2014,** *5* (20), 5873-5884.

[34] Ong, W.; Kaifer, A. E., Unusual electrochemical properties of unsymmetric viologen dendrimers. *Journal of the American Chemical Society* **2002,** *124* (32), 9358-9359.

[35] Ong, W.; Grindstaff, J.; Sobransingh, D.; Toba, R.; Quintela, J. M.; Peinador, C.; Kaifer, A. E., Electrochemical and Guest Binding Properties of Fréchet- and Newkome-Type Dendrimers with a Single Viologen Unit Located at Their Apical Positions. *Journal of the American Chemical Society* **2005,** *127* (10), 3353-3361.

[36] Bhattacharya, P.; Kaifer, A. E., Preparation, Characterization, and Electrochemical Properties of a New Series of Hybrid Dendrimers Containing a Viologen Core and Fréchet and Newkome Dendrons. *The Journal of Organic Chemistry* **2008,** *73* (15), 5693-5698.

[37] Kawauchi, T.; Oguchi, Y.; Nagai, K.; Iyoda, T., Conical Gradient Junctions of Dendritic Viologen Arrays on Electrodes. *Sci Rep-Uk* **2015,** *5*.

[38] Murov, S. L.; Carmichael, I.; Hug, G. L., *Handbook of Photochemistry, Second Edition*. Taylor & Francis: 1993.

[39] Figueira-Duarte, T. M.; Mullen, K., Pyrene-Based Materials for Organic Electronics. *Chem Rev* **2011,** *111* (11), 7260-7314.

[40] Cicchi, S.; Fabbrizzi, P.; Ghini, G.; Brandi, A.; Foggi, P.; Marcelli, A.; Righini, R.; Botta, C., Pyrene-Excimers-Based Antenna Systems. *Chem-Eur J* **2009,** *15* (3), 754-764.

[41] Liu, F.; Lai, W. Y.; Tang, C.; Wu, H. B.; Chen, Q. Q.; Peng, B.; Wei, W.; Huang, W.; Cao, Y., Synthesis and characterization of pyrene-centered Starburst oligofluorenes. *Macromol Rapid Comm* **2008,** *29* (8), 659-664.

[42] Zhao, Z. J.; Li, J. H.; Chen, X. P.; Wang, X. M.; Lu, P.; Yang, Y., Solution-Processable Stiff Dendrimers: Synthesis, Photophysics, Film Morphology, and Electroluminescence. *J Org Chem* **2009,** *74* (1), 383-395.

[43] Bolink, H. J.; Barea, E.; Costa, R. D.; Coronado, E.; Sudhakar, S.; Zhen, C.; Sellinger, A., Efficient blue emitting organic light emitting diodes based on fluorescent solution processable cyclic phosphazenes. *Org Electron* **2008,** *9* (2), 155-163.

[44] Kawauchi, T.; Oguchi, Y.; Sawayama, J.; Nagai, K.; Iyoda, T., Microwave-Assisted Synthesis of Dendritic Viologen-Arranged Molecules with an ω-Mercaptoalkyl Group and

Their Self-Assembled Monolayers Complexed with Various Anions. *Macromolecules* **2015,** *48* (22), 8090-8097.

[45] Berlman, I. B., *Handbook of fluorescence spectra of aromatic molecules*. 2d ed.; Academic Press: New York, 1971; pp 184.

[46] Raytchev, M.; Pandurski, E.; Buchvarov, I.; Modrakowski, C.; Fiebig, T., Bichromophoric interactions and time-dependent excited state mixing in pyrene derivatives. A femtosecond broad-band pump-probe study. *J Phys Chem A* **2003,** *107* (23), 4592-4600.

[47] Miyasaka, H.; Masuhara, H.; Mataga, N., Picosecond Absorption Spectra and Relaxation Processes of the Excited Singlet State of Pyrene in Solution. *Laser Chemistry* **1983,** *1* (5), 357-386.

[48] Sarkar, A.; Mukherjee, T.; Kapoor, S., Formation of silver nanoparticles in formamide:water mixtures: a radiolytic study. *Res Chem Intermediat* **2010,** *36* (2), 173-179.

[49] Piotrowiak, P.; Miller, J. R., Counterion Effects in Intramolecular Charge-Transfer in Radical-Anions. *J Phys Chem-Us* **1993,** *97* (50), 13052-13060.

[50] Piotrowiak, P., Specific ion-pairing effects in weakly exoergic intramolecular electron transfer. *Inorganica Chimica Acta* **1994,** *225* (1-2), 269-274.

[51] Piotrowiak, P., Electrolyte Effects in Intramolecular Electron Transfer. In *Photochemistry and Radiation Chemistry*, American Chemical Society: 1998; Vol. 254, pp 219-230.

[52] Marcus, R. A., Ion Pairing and Electron Transfer. *The Journal of Physical Chemistry B* **1998,** *102* (49), 10071-10077.

[53] Kuczynski, J. P.; Milosavljevic, B. H.; Lappin, A. G.; Thomas, J. K., Ion-Pair Complexes of Methyl Viologen and Anionic Solutes. *Chem Phys Lett* **1984,** *104* (2-3), 149-152.

[54] Credi, A.; Dumas, S.; Silvi, S.; Venturi, M.; Arduini, A.; Pochini, A.; Secchi, A., Viologen-Calix[6]arene Pseudorotaxanes. Ion-Pair Recognition and Threading/Dethreading Molecular Motions. *The Journal of Organic Chemistry* **2004,** *69* (18), 5881-5887.

[55] Saielli, G., Ion-Pairing of Octyl Viologen Diiodide in Low-Polar Solvents: An Experimental and Computational Study. *The Journal of Physical Chemistry A* **2008,** *112* (35), 7987-7995.

[56] Huang, F.; Jones, J. W.; Slebodnick, C.; Gibson, H. W., Ion Pairing in Fast-Exchange Host−Guest Systems: Concentration Dependence of Apparent Association Constants for Complexes of Neutral Hosts and Divalent Guest Salts with Monovalent Counterions. *Journal of the American Chemical Society* **2003,** *125* (47), 14458-14464.

[57] Grozema, F. C.; Berlin, Y. A.; Siebbeles, L. D. A., Mechanism of Charge Migration through DNA: Molecular Wire Behavior, Single-Step Tunneling or Hopping? *Journal of the American Chemical Society* **2000,** *122* (44), 10903-10909.

[58] Bixon, M.; Jortner, J., Long-range and very long-range charge transport in DNA. *Chemical Physics* **2002,** *281* (2-3), 393-408.

[59] Gray, H. B.; Winkler, J. R., Long-range electron transfer. *Proceedings of the National Academy of Sciences* **2005,** *102* (10), 3534-3539

[60] Winkler, J. R.; Gray, H. B., Long-Range Electron Tunneling. *Journal of the American Chemical Society* **2014,** *136* (8), 2930-2939.

[61] Thompson, A. L.; Gaab, K. M.; Xu, J.; Bardeen, C. J.; Martínez, T. J., Variable Electronic Coupling in Phenylacetylene Dendrimers: The Role of Förster, Dexter, and Charge-Transfer Interactions. *The Journal of Physical Chemistry A* **2004,** *108* (4), 671-682.

[62] McConnell, H. M., Intramolecular Charge Transfer in Aromatic Free Radicals. *The Journal of Chemical Physics* **1961,** *35* (2), 508-515.

[63] Turro, N. J.; Ramamurthy, V.; Scaiano, J. C. *Principles of Molecular Photochemistry: An Introduction*; University Science Publishers: New York, **2008**; pp 383-479.

[64] Paddon-Row, M. N., Orbital interactions and long-range electron transfer. 2003; pp 1-85.

[65] Häupl, T.; Lomoth, R.; Hammarström, L., Femtosecond Dynamics of the Photoexcited Methyl Viologen Radical Cation. *The Journal of Physical Chemistry A* **2003,** *107* (4), 435-438.

[66] Marenich, A. V.; Olson, R. M.; Kelly, C. P.; Cramer, C. J.; Truhlar, D. G., Self-Consistent Reaction Field Model for Aqueous and Nonaqueous Solutions Based on Accurate Polarized Partial Charges. *Journal of Chemical Theory and Computation* **2007,** *3* (6), 2011-2033.

Chapter 4. Influences of Donor-Acceptor Separation, Connectivity, and Solvent on Electron Transfer Reactions in Pyrene-Viologen Systems

The influences of donor-acceptor separation, connectivity, and solvent on electron transfer rates in different pyrene-viologen donor-acceptor systems were studied using the ultrafast laser spectroscopy. The extension of intervening bridge between pyrene and attached viologen from $-CH_2-$ to $-(CH_2)_4-$ significantly decreases the rates of charge separation and recombination occurring at the apex by ~4 times, which efficiently prolongs the intrinsic short lifetime of charge-separated (CS) state generated in $P-C1-(V^{2+})_n$ dendrons. Then, a new pyrene-viologen system in which the number of viologens grows linearly from P−C4−L1 to P−C4−L3 has been synthesized to inquire into the topology effect on electron transfer process. The linear arrays of viologen electron acceptors exhibit a weaker ability to intercept electrons in comparison with analogous dendrons. Lastly, the investigation of solvent effect in the presence of acetonitrile and propylene carbonate shows that the electron transfer rates are strongly influenced by solvent polarity as well as the viscosity.

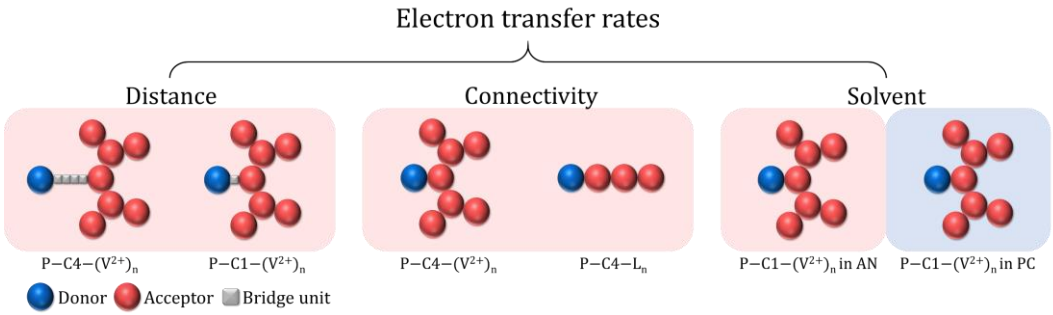

Scheme 1. The influences of distance, connectivity and solvent on electron transfer rates in pyrene-viologen systems.

4.1 Introduction

The classical Marcus theory of nonadiabatic electron transfer expresses the electron transfer rate constant using three important variables, namely, the electronic coupling between donor and acceptor (V), the reorganization energy (λ), and the driving force ($-\Delta G^{\circ}$) (see **1.4.3**). It therefore follows that an understanding of electron transfer kinetics entails an investigation of how these parameters are dependent on factors such as donor-acceptor separation and orientation [1-9], structural connectivity [10-14], and the solvent properties [15-19].

In general, for an adiabatic electron transfer occurring when donor and acceptor are in van der Waals contact, the magnitude of electronic coupling is much greater than 200 cm^{-1} which always leads to rapid electron transfer rates. Whereas, nonadiabatic electron transfer should dominate for the separation exceeding the sum of van der Waals radii of the donor and acceptor. In this case, the electronic coupling is relatively weak and significantly affected by the distance between donor and acceptor (r_{DA}), which leads to a strong distance dependence of electron transfer rates. In a given donor-acceptor system, the driving forces for the charge separation and recombination are expected to be weakly dependent on r_{DA} due to a small change in magnitude of Coulomb term, especially in polar solvents (see **1.3**). As for reorganization energy, the internal component, λ_{inner}, is characteristic of the donor and acceptor molecules and does not depend on distance. The change in solvation component, λ_{sol}, according to the calculation based on two-sphere dielectric continuum model, is usually less than 0.05 eV in nonpolar solvents but may be significant in polar solvents (see **1.4.2**).

Distance dependence of electron transfer rates has been investigated in numerous

systems where the donor and the acceptor are covalently linked by an inert bridge of variable length. The rate constants for electron transfer through saturated steroidal [2, 20-21], norbornyl [22-23], and peptide [24-25] intervening spacers have shown to decrease exponentially with increasing the distance between donor and acceptor as $e^{-0.5\beta r_{DA}}$ where β is a damping parameter scaling the distance dependence. These observations were interpreted in terms of through-space (TS) or through-bond (TB) interaction depending on how the electronic coupling between donor and acceptor was achieved. When the donor is electronically coupled with the acceptor through a TS mechanism, the coupling is accomplished through an electron exchange interaction that occurs from the overlap of their wavefunctions [6, 26-27]. Since the spatial overlap decreases dramatically as a function of separation, the TS interaction is expected to be insignificant when the donor and the acceptor are separated by >10 Å. Instead, the TB coupling predominates the long-range electron transfer processes. The strength of electronic interaction between donor and acceptor can be efficiently propagated by mixing the wavefunctions of σ and σ^* orbitals of the bridge and the wavefunctions of donor and acceptor, which is referred to as TB or superexchange interaction [6, 26-28]. The values of β extracted from TB mechanism are much smaller than TS values and usually range from 0.04 to 1.4 $Å^{-1}$ depending on the nature of intervening bridge [6].

Another important aspect of electron transfer reaction which has been recognized and elaborated in both theoretical [29-31] and experimental work [32-37] is the solvent effect. As addressed by Marcus theory, solvents with different polarity can significantly alter the charge transfer rates by varying the amplitudes of $-\Delta G^{\circ}$ and λ_{sol}. Generally, an increase in the solvent polarity results not only in stabilization of CS states but also in an

increased in λ_{sol}. Furthermore, switching solvent may affect molecular conformation and change the electronic coupling term, which also leads to different electron transfer rates. Understanding the solvent effect can provide an approach for controlling the electron transfer reactions and enhance the performance of applicable devices in various environments.

4.2 Distance dependence of intramolecular electron transfer dynamics

4.2.1 Introduction of P−C4−$(V^{2+})_n$ dendrons

In P−C1−$(V^{2+})_n$ dendron family (see **Chapter 3**), the electron donor is linked to the apical viologen unit by a single −CH_2− group. The short methylene bridge leads to very rapid charge recombination taking place with $\tau = 0.7\,\mathrm{ps}$, which largely reduces the fraction of electrons that survive to propagate into the dendritic network. In order to maximize the kinetic forward bias set up by the branched structure and allow the dendron to act as a topological rectifier, one must move the system away from the limit of $k_{CR} \gg k_{hop}$. This can be achieved by lowering the electronic coupling between the electron donor and attached acceptor at the apex of the dendron. While the charge separation rate will be similarly affected, the long S_1 lifetime of pyrene leaves a large kinetic margin for achieving nearly quantitative quantum yields of the CS state. For this purpose, a new pyrene-viologen dendron family, in which the link between pyrene and first viologen is extended by four intervening methylenes (−$(CH_2)_4$−), has been synthesized (**Scheme 2**).

All P−C4−$(V^{2+})_n$ dendrons were prepared via a microwave heating technique, which is similar to the syntheses of P−C1−$(V^{2+})_n$ dendrons. Detailed synthetic and characterization procedures are available in [38-39]. The sample preparation of

P−C4−$(V^{2+})_n$ dendrons is same as that of P−C1−$(V^{2+})_n$ dendrons (see **3.2.2**). Importantly, the concentration of all the dendrons was 1.5×10^{-5} M, as verified by their absorption spectra (**Figure 1a**).

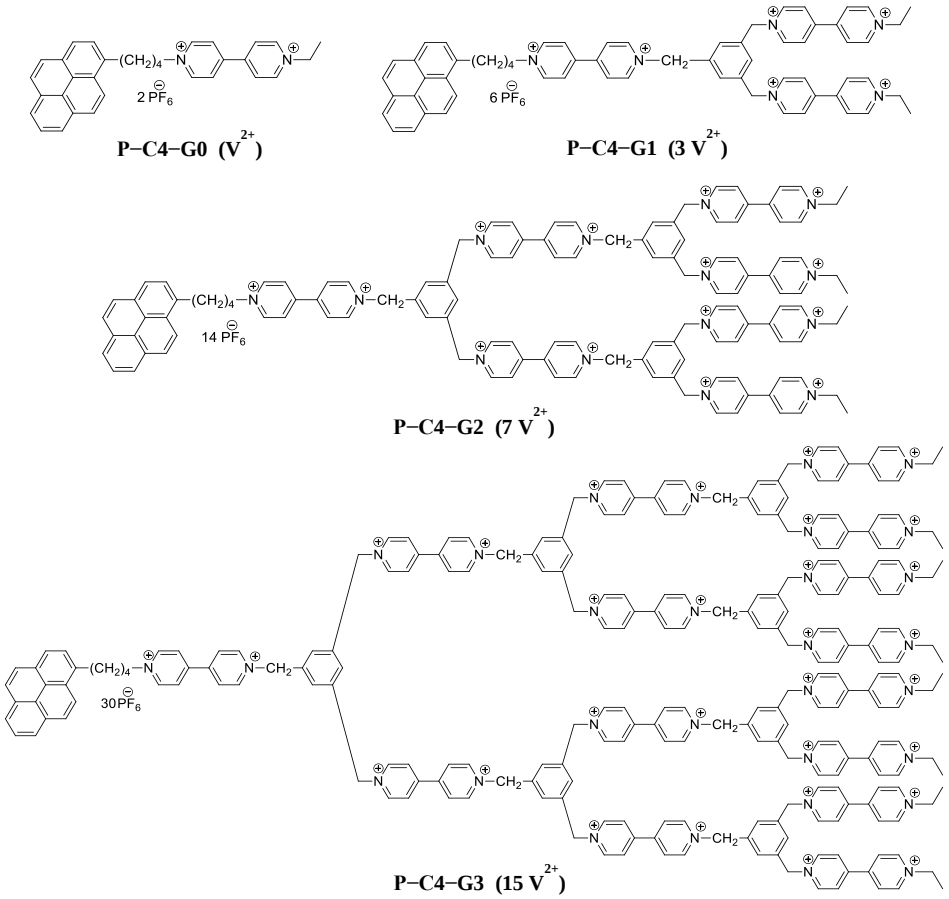

Scheme 2. Chemical structures of P−C4−$(V^{2+})_n$ family. The number of viologen units increases exponentially from P−C4−G0 to P−C4−G3 and is indicated in parentheses.

4.2.2 Results and discussion

The ground state UV absorption spectra of P−C4−$(V^{2+})_n$ dendrons (**Figure 1a**) show the characteristic pyrene progression in the 300~350 nm region, which remains unchanged for all generations. In the wavelength range between 230-290 nm, both pyrene and viologen absorb light, and as the number of viologen units increases the spectrum

becomes dominated by the absorption of the latter. The spectrum of P−C4−G0 displays a more information-riched vibronic structure of pyrene moiety in comparison with that of P−C1−G0 (**Figure 1c**), especially for the absorption bands centered at 255, 312, and 355 nm. Furthermore, a new absorption band appearing as a shoulder peak at 235 nm becomes distinguishable in the spectrum of P−C4−G0. The whole spectrum of P−C4−G0 shows a slight blueshift (~3 nm) with respect to P−C1−G0. All the observations imply a weaker interaction in which the donor and acceptor moieties in P−C4−G0 are more likely to retain their individual identities.

The characteristic intense fluorescence of pyrene is > 99.4 % quenched in the solutions of all P−C4−$(V^{2+})_n$ dendrons pointing to rapid and practically quantitative charge separation (**Figure 1b**). The weak residual emission of P−C4−G0 is blueshifted by ~10 nm accompanying with a 3-fold increase in intensity compared with the spectrum of P−C1−G0 using the same excitation wavelength (**Figure 1d**). The observed gain of emission can be attributed to a slower process of electron transfer quenching of the excited state in P−C4−G0 as well as in higher generations of P−C4−$(V^{2+})_n$ system. This result is the primary indication that the electron transfer rate is decreased with increasing the donor-acceptor separation.

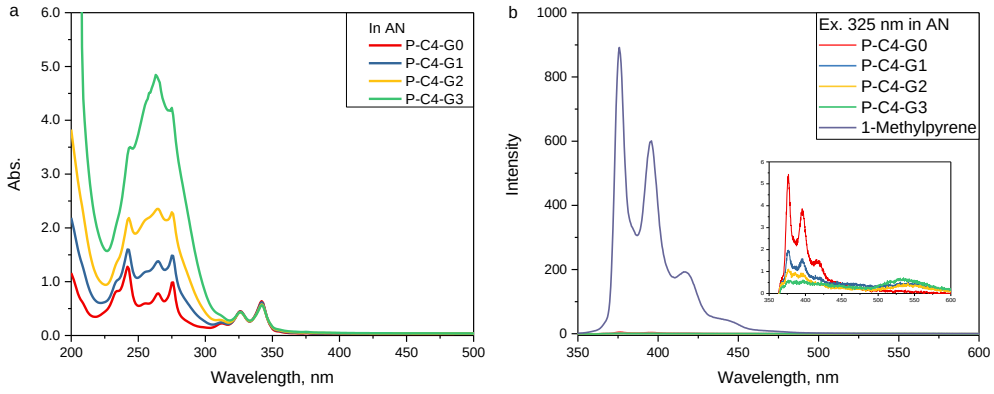

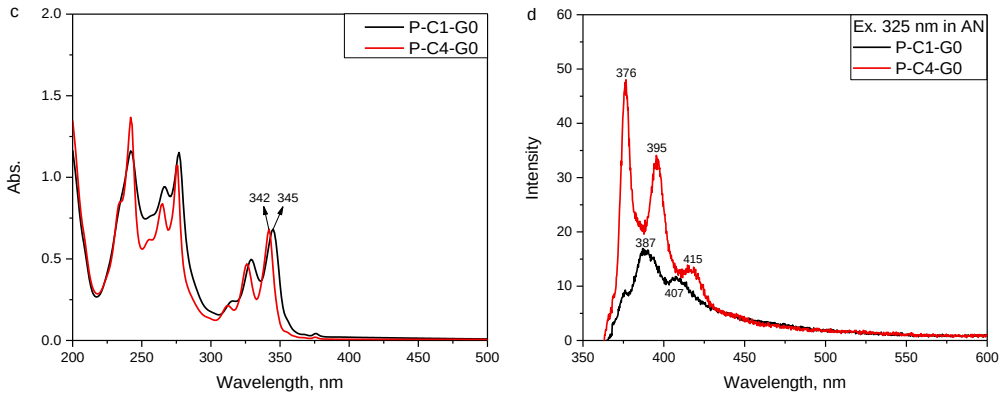

Figure 1. (a) Steady-state absorption spectra of P−C4−$(V^{2+})_n$ dendrons; (b) fluorescence spectra of P−C4−$(V^{2+})_n$ dendrons; (c) the comparison of absorption spectra of P−C1−G0 and P−C4−G0; (d) the comparison of fluorescence spectra of P−C1−G0 and P−C4−G0. All spectra were recorded for 1.5×10^{-5} M solutions of the respective compounds in CH_3CN.

Excitation of P−C4−$(V^{2+})_n$ dendrons with 342 nm ~25 fs pulses results in the rapid appearance of a CS state which is characterized by a broad absorption band of the reduced viologen, $MV^{+\bullet}$, at 550~700 nm and a sharper peak of the oxidized pyrene, $Py^{+\bullet}$, at 465 nm (**Figure 2**). The transient absorption spectra of P−C4−$(V^{2+})_n$ dendrons are redshifted by 15 nm in comparison with the ones collected for P−C1−$(V^{2+})_n$ dendrons.

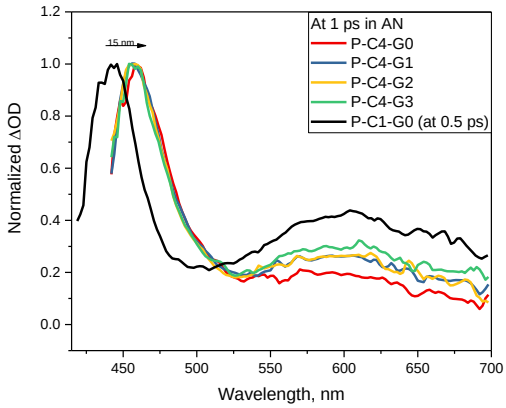

Figure 2. Normalized transient absorption spectra of P−C4−$(V^{2+})_n$ dendrons. All spectra were recorded at 1 ps delay following 342 nm excitation. The 465 nm band is characteristic of $Py^{+\bullet}$ while the broad 615 nm band belongs to $MV^{+\bullet}$.

The weaker electronic coupling between pyrene and the first viologen separated by 4 methylenes is expected to retard the rates of charge separation and the recombination at the apex of each dendron in the family of P−C4−$(V^{2+})_n$. This behavior can be demonstrated by comparing the transient absorption decays recorded for P−C1−$(V^{2+})_n$ and P−C4−$(V^{2+})_n$ dendron families. The decay of the CS state produced in P−C4−G0 occurs as a single exponential process with a time constant of $\tau_{CR} = 2.9{\sim}3.1$ ps (**Figure 3** and **Tables 1** and **2**) which corresponds to electron-hole recombination of oxidized pyrene and the attached reduced viologen. This decay time is ~4 times slower than $\tau_{CR} = 0.71{\sim}0.76$ ps detected in P−C1−G0, indicating a falloff of the charge recombination rate with the increasing distance between donor and acceptor.

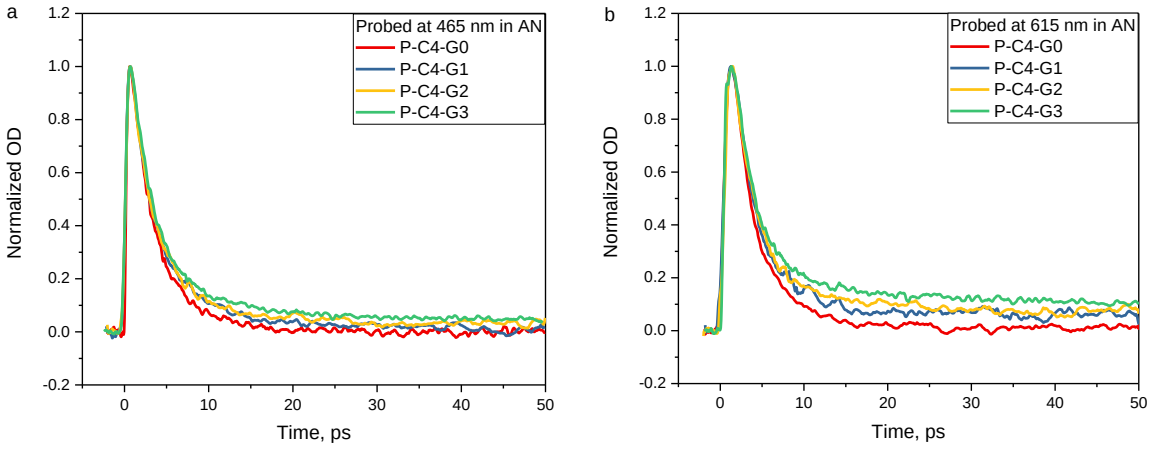

Figure 3. Transient absorption decay profiles of P−C4−G dendron family recorded at (a) 465 nm, the absorption maximum of $Py^{+\bullet}$, and (b) 615 nm, the absorption maximum of $MV^{+\bullet}$.

A similar influence on charge separation process is also observed by fitting the rising and initial decay region of the kinetic traces recorded for P−C1−G0 and P−C4−G0 using a double exponential function .in the short 10 ps time window (**Figure 4**). The component τ_f with a negative amplitude is assigned to the charge separation from the

pyrene donor to the first viologen acceptor. Both τ_1 were fixed during the fitting in accordance with the charge recombination time constant $\tau_{CR} = 0.74$ ps for P−C1−G0 and $\tau_{CR} = 3.1$ ps for P−C4−G0 respectively. Since the extremely rapid charge separation, especially for P−C1−G0, occurs within the time resolution of our measurements, the instrument response time should be taken into consideration. The actual time constant for charge separation can be calculated through $\tau_{CS} = \sqrt{{\tau_{obs}}^2 - {\tau_{IRT}}^2}$ where τ_{obs} is the observed time constant derived from the exponential fitting and τ_{IRT} is the instrument response time largely relying on the resolution of probe pulses. Due to an uncertain in τ_{IRT} ranging from 75 to 100 fs, $\tau_{CS} = 38\sim76$ fs for P−C1−G0 and $\tau_{CS} = 217\sim207$ fs for P−C4−G0 are obtained, which is consistent with respective changes of the charge recombination rate.

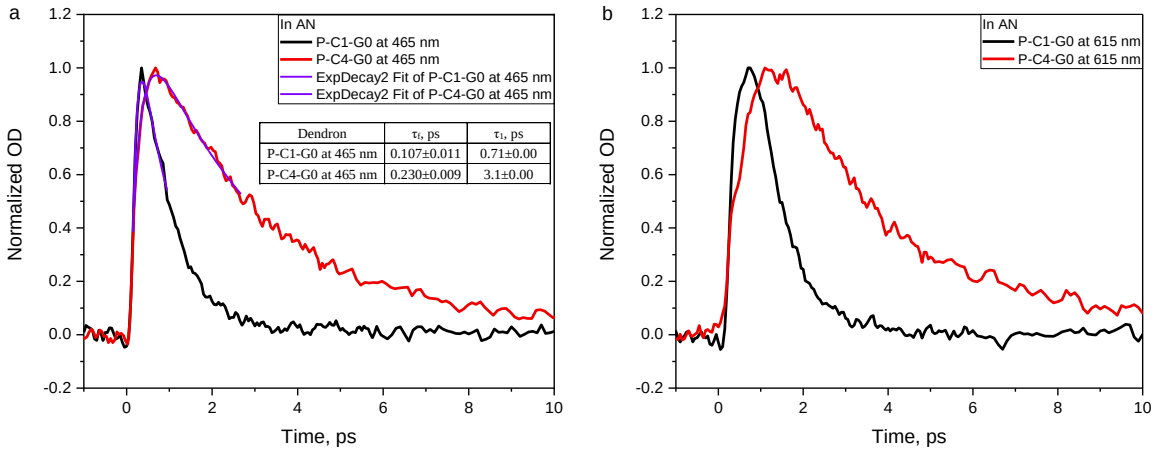

Figure 4. The comparison of transient absorption decay profiles of P−C1−G0 and P−C4−G0 in acetonitrile probed at (a) 465 nm, the absorption of $Py^{+\bullet}$, and (b) 615 nm, the absorption of $MV^{+\bullet}$. The inset shows the biexponential fitting parameters for the rising and initial decaying part of the kinetic traces.

When the distance between donor and acceptor increases to a length of the four-carbon spacer, the center-to-center distance between pyrene and attached viologen grows significantly from 7.9 Å in P−C1−G0 to 12.2 Å in P−C4−G0. However, it is surprising to find that the average charge recombination rate, $k_{CR}(\mathrm{P-C4-G0}) = 3.3 \times 10^{11}\ \mathrm{s^{-1}}$, is only approximately 4 times slower in comparison with $k_{CR}(\mathrm{P-C1-G0}) = 1.4 \times 10^{12}\ \mathrm{s^{-1}}$. Since the rate constant of electron transfer displays an exponential dependence on donor-acceptor separation as $k_{et} \propto e^{-\beta \cdot r_{DA}}$ regardless whether TS or TB mechanism is present, one can calculate the value of damping parameter, $\beta = 0.49\ \mathrm{Å^{-1}}$. In view of the insulating nature of the saturated σ-bonded framework of the hydrocarbon linkage which usually gives $\beta = 0.75{\sim}0.98\ \mathrm{Å^{-1}}$ [6], this value is unreasonably low. One plausible explanation for such a weak distance dependence of electron transfer rates observed in pyrene-viologen system can be given from the point of view of classical Marcus theory. The driving forces for charge separation, $-\Delta G^0{}_{CS} = -1.7\ \mathrm{eV}$, and recombination, $-\Delta G^0{}_{CR} = -1.6\ \mathrm{eV}$, remain almost constant when the linkage between pyrene and attached viologen is replaced by 4 methylenes. Whereas, the reorganization energy, λ, increases significantly from 1.28 eV for P−C1−G0 to 1.61 eV for P−C4−G0, which forces both charge separation and recombination processes to reach the barrier-less optimum where the maximum rate of electron transfer is achieved. The overall picture can be described as a process where the growth in r_{DA} decreases $|V|$ pulling the Marcus parabola down and meanwhile increases λ_{sol} shifting the parabola to the right. This evolution gives rise to a weaker dependence of r_{DA} on k_{et} in the inverted region than in the normal region (**Figure 5**). As a result, the rate constants for charge separation and recombination occurring at the apex of the dendron are less sensitive to the length of the bridge than one

might expect solely on the basis of the distance dependence of $|V|$.

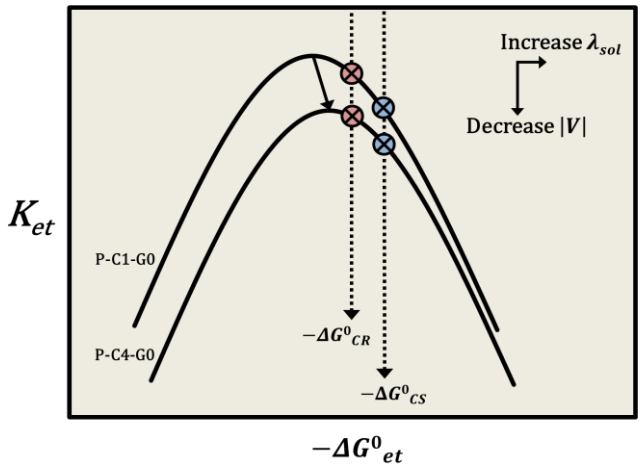

Figure 5. The shift of Marcus parabola with increasing donor-acceptor distance [3].

In addition, it should be mentioned that the charge recombination profiles of P−C4−G0 can be fitted with a double exponential function. The fitting results (**Table 3**) indicate that both kinetics probed at the 465 nm band of $Py^{+\bullet}$ and the 615 nm band of $MV^{+\bullet}$ is dominated by two components, $\tau_1 = 1.8$ ps and $\tau_2 = 4.2{\sim}4.8$ ps, each of which constitutes approximately 50% of the initial excited state population. The most obvious reason for this biexponential behavior is the existence of conformers caused by rotation around the carbon-carbon bonds of the flexible polymethylene chain. In P−C1−G0 diad, pyrene and viologen moieties can be regarded as two substituents that are located at two corners of a tetrahedral methane. Given this rigid configuration, the center-to-center distance between donor and acceptor is nearly constant, and the freedom of molecular motion is limited to pivoting about the $-CH_2-$ linkage. Since the decay of CS state produced in P−C1−G0 exhibits a single exponential and homogenous behavior, the donor-acceptor electronic coupling is relatively insensitive to the mutual orientation of the pyrene and viologen units (see **3.3.3**). However, extracting distance dependence of donor-acceptor

electronic coupling from P−C4−G0 is certainly complicated by the fact that electron transfer is likely to occur from all conformers present in the solution. The calculation on conformational distribution of P−C4−G0 in polar DMF ($\varepsilon = 36.7$) at HF/6-31G* level shows that the extended conformers constitute ~85% of the total 10^5 examined P−C4−G0 replicas. The calculation performed in DMF whose dielectric constant is close to acetonitrile suggests that the charged viologen prefers to be fully solvated by surrounding polar solvent molecules. Therefore, the folded conformation which enables the donor and acceptor moieties to lie in close spatial proximity to each other is not favored and such "shortcut" of the electron transfer pathway does not accelerate the observed charge recombination rate.

In the P−C4−$(V^{2+})_n$ family, the appearance of longer lifetime components in the decay of CS state is also observed in the diverging dendritic generations and analyzed using a biexponential fitting (**Figure 3** and **Table 1**, **2**). As in the previous chapter, the value of τ_1, which corresponds to the recombination of electrons failing to escape beyond the apical viologen, was set equal to the decay rate of CS state in P−C4−G0 and kept constant for higher generations.

For the first generation dendron, P−C4−G1, a slower component decaying with $\tau_2 = 12.3{\sim}13.8$ ps, and the longest-lived component, A_∞, which does not decay within the 50 ps time window, were detected. Together, they account for approximately 15.2% of the overall population of the initial CS state. Compared with the 4% observed in P−C1−G1, the fraction of electrons which escape beyond the first viologen unit and migrate further down into the dendritic network dramatically increases by nearly 4 times. Thus, the outward flow of electrons away from the donor was more favored by decreasing the charge

recombination rate at the apex. The charge recombination time constant, $\tau_2 =$ 12.3~13.8 ps, mainly encompasses the forward electron jump to the viologen units in the second shell, the return to the apical one, and the final electron-hole recombination. This implies that the "round trip" of electron hopping between adjacent viologen units in P−C4−G1 occurs on the time scale of 9.4~10.6 ps which is slower than 5.4~7.0 ps in P−C1−G1. This behavior possibly results from the less efficient long-range electron tunneling which is discussed in detail below.

The higher generations of P−C4−$(V^{2+})_n$ dendron family display more pronounced slowing down of the recombination dynamics. The average time constant τ_2 increases to 15.2 ps in P−C4−G2 and 20.4 ps in P−C4−G3 since the expansion of acceptor shells allows the injected electron to travel further away from the donor. In the light of known kinetics features of the P−C1−$(V^{2+})_n$ system, the accompanying steady increase of the long-lived fraction of CS state given by the sum of amplitudes A_2 and A_∞ (**Tables 1** and **2**) is attributed to long-range electron tunneling and the electric field gradient set up by multiple charged viologen units. Compared with more than 10% increase in long-lived fraction from 4% in P−C1−G1 to 13~14% in P−C1−G3, the sum $A_2 + A_\infty$ detected in P−C4−$(V^{2+})_n$ dendrons exhibits a much smaller generation dependent extension from 15.2% in P−C4−G1 to 16.8% in P−C4−G2 and 19.7% in P−C4−G3. The less pronounced increase in the long-lived CS state population is likely to result from decreased rates for long-range electron tunneling to distant viologen units. Even though in P−C4−$(V^{2+})_n$ dendron family the partially conjugated mesitylene units still facilitate the long-range electron tunneling, the presence of 4 saturated methylenes in the long intervening bridge increases the separation between donor and distant acceptor and gives rise to a larger average damping

factor, β (see **3.6.6**). For both reasons, the long-range electron tunneling rates are dramatically slowed down and the site-to-site hopping plays a greater role in the growth of the long-lived fraction of CS state.

Table 1. Fitting parameters for the decay of the $Py^{+\bullet}$ signal monitored at 465 nm for P−C4−$(V^{2+})_n$ dendrons.

Generation	τ_1, ps	A_1	τ_2, ps	A_2	A_∞	$A_2 + A_\infty$
P−C4−G0	3.1 ± 0.02	1.0	–	–	–	–
P−C4−G1	3.1 ± 0.0	0.857 ± 0.017	13.8 ± 1.3	0.128 ± 0.020	0.015 ± 0.002	0.143 ± 0.022
P−C4−G2	3.1 ± 0.0	0.859 ± 0.023	14.2 ± 1.7	0.106 ± 0.024	0.035 ± 0.002	0.141 ± 0.026
P−C4−G3	3.1 ± 0.0	0.832 ± 0.008	16.8 ± 0.8	0.116 ± 0.008	0.052 ± 0.001	0.168 ± 0.009

Table 2. Fitting parameters for the decay of the $MV^{+\bullet}$ signal monitored at 615 nm for P−C4−$(V^{2+})_n$ dendrons.

Generation	τ_1, ps	A_1	τ_2, ps	A_2	A_∞	$A_2 + A_\infty$
P−C4−G0	2.9 ± 0.03	0.985 ± 0.006	–	–	0.015 ± 0.001	–
P−C4−G1	2.9 ± 0.0	0.838 ± 0.036	12.3 ± 3.8	0.090 ± 0.037	0.072 ± 0.003	0.162 ± 0.040
P−C4−G2	2.9 ± 0.0	0.806 ± 0.011	16.1 ± 1.8	0.114 ± 0.011	0.080 ± 0.003	0.194 ± 0.014
P−C4−G3	2.9 ± 0.0	0.774 ± 0.003	24.0 ± 1.1	0.118 ± 0.003	0.108 ± 0.001	0.226 ± 0.004

Table 3. Biexponential fitting parameters for the decay recorded for P−C4−G0.

λ_{Probe}, nm	τ_1, ps	A_1	τ_2, ps	A_2	A_∞	$A_2 + A_\infty$
465	1.8 ± 0.1	0.546 ± 0.023	4.2 ± 0.1	0.454 ± 0.082	0.000	0.454 ± 0.082
615	1.8 ± 0.1	0.546 ± 0.023	4.2 ± 0.1	0.454 ± 0.082	0.000	0.454 ± 0.082

4.3 The topology effect on intramolecular electron transfer dynamics

4.3.1 Introduction of P−C4−L system

In both P−C1−$(V^{2+})_n$ and P−C4−$(V^{2+})_n$ dendron families, we have shown that a diverging dendritic network can intercept electrons and extend the lifetime of a short-lived photoinduced CS state of the pyrene-viologen donor-acceptor diad through a combination of long-range electron tunneling and site-to-site hopping. In order to assess the topology

effect on electron transfer dynamics, a new series of compounds with pyrene attached to a linear chain of viologens was synthesized (**Scheme 3**). In the P−C4−L system, the 1→1 connectivity of acceptor units would alter the way of electronic communication between two viologen centers observed in analogous P−C4−$(V^{2+})_n$ dendritic system. Therefore, the overall electron transfer kinetics in the linear array of viologen electron acceptors should be different from that in a corresponding dendron.

The linear P−C4−L arrays, up to the third generation, were synthesized via a microwave heating technique [38-39]. In the process of synthesis (see **3.2.1**), 1,4-bis(bromomethyl)benzene was used instead of 1,3,5-tris(bromomethyl)benzene to afford 1→1 connectivity of viologens units. All P−C4−L compounds were dissolved in acetonitrile at the concentration of 1.5×10^{-5} M, as verified by their steady-state absorption spectra (**Figure 6**).

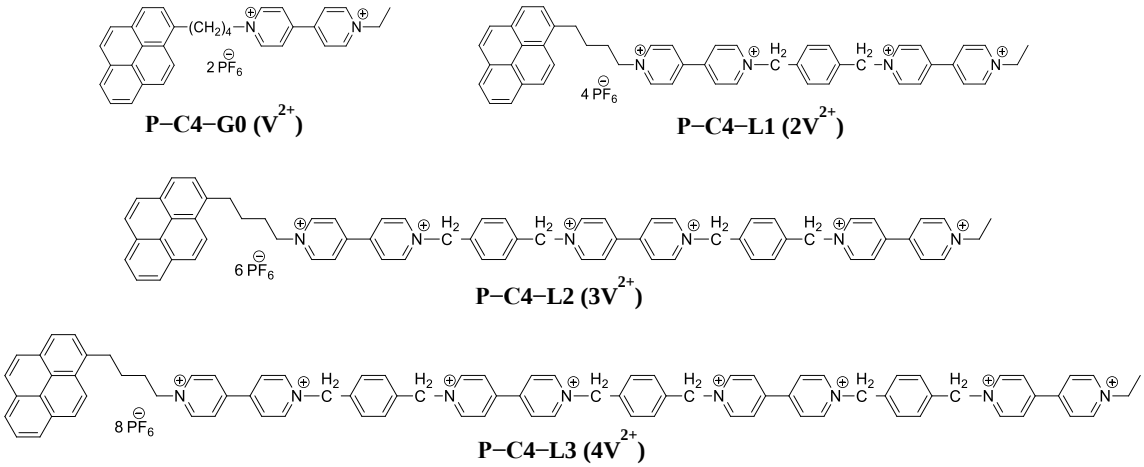

Scheme 3. Chemical structures of P−C4−L family. The number of viologen units increases linearly from P−C4−G0 to P−C4−L3 and is indicated in parentheses.

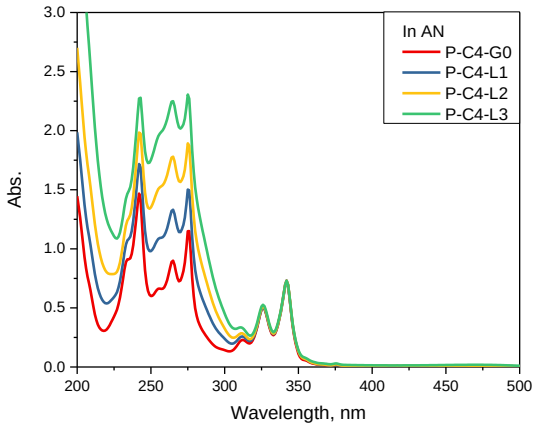

Figure 6. Steady-state absorption spectra of P−C4−G0, P−C4−L1, P−C4−L2 and P−C4−L3 recorded at the concentration of 1.5×10^{-5} M in CH_3CN.

In the linear P−C4−L system, after the initial electron transfer from the photoexcited donor to the LUMO of the apical acceptor, the electron is expected to travel along the linear chain of acceptors and undergoes at least one hop before returning to the apex. For the *n*th generation in P−C4−L family, because of the 1→1 connectivity of the acceptor array, the injected electron located at the viologen site in the *m*th ($0<m<n$) layer has an equal probability to move forward and backward, namely $P_{fr} = P_{back} = 1/2$ (**Figure 7**). Whereas in a dendritic system with 1→2 branching network of acceptors such as in P−C1−$(V^{2+})_n$ and P−C4−$(V^{2+})_n$ families, one viologen electronically couples with attached four degenerate sites. In this case, for an injected electron at any viologen site in the *m*th ($0<m<n$) layer, the probability of migrating forward to (m+1)th layer is 1/2, crossing over to the site in the same layer is 1/4, and returning to the (m-1)th layer is 1/4. For the apical viologen (m=0), the probability of electron hopping to the first layer is 1 in both dendritic and linear systems. For a terminal viologen in the *n*th generation (m=n), the probability of a return hop is 1/2 in a dendritic network, whereas in the linear chain it is 1. Overall, the probability of the electron arriving at the *m*th ($0<m<n$) layer and then returning

to the origin in the minimum possible number of steps decreases with the layer *m* in the linear chain as $P_{CR}(\text{linear}) = (1/2)^{2m-1}$, whereas in the dendritic network it follows a steeper $P_{CR}(\text{dendron}) = (1/2)^{3m-1}$ dependence (**Table 4** and **Figure 8**). Therefore, in P−C4−L*n* the probability of charge recombination from each layer is 2^n times greater than that in P−C4−G*n*. Accordingly, it is easier for the injected electron to become "lost" in the network of a 1→2 branching dendron than in a corresponding linear array.

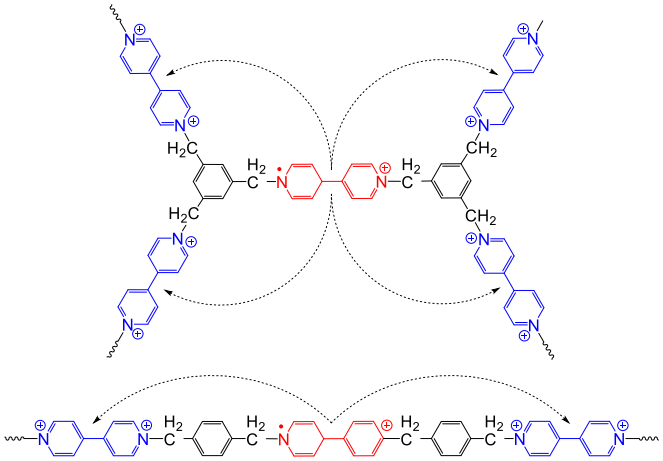

Figure 7. Possible electron hopping pathways from a reduced viologen site (marked in red) to the neighboring degenerate sites (marked in blue) in a 1→2 branching dendritic network (top) and a linear array (bottom) of viologen electron acceptors.

Table 4. Probability of corresponding events occurring in a *n*th generation dendron and linear array.

Event (in the minimum possible number of steps)	Dendritic	Linear
Probability of hopping to the *m*th layer ($m = 1, 2, \ldots, n$)	$\left(\frac{1}{2}\right)^{m-1}$	$\left(\frac{1}{2}\right)^{m-1}$
Probability of returning to the apical viologen from *m*th layer ($m = 1, 2, \ldots, n-1$)	$\left(\frac{1}{2}\right)^{2m}$	$\left(\frac{1}{2}\right)^{m}$
Probability of returning to the apical viologen from periphery ($m = n$)	$\left(\frac{1}{2}\right)^{2m-1}$	$\left(\frac{1}{2}\right)^{m-1}$
Probability of round trip between apical viologen and *m*th layer ($m = 1, 2, \ldots, n-1$)	$\left(\frac{1}{2}\right)^{3m-1}$	$\left(\frac{1}{2}\right)^{2m-1}$
Probability of round trip between apical viologen and periphery ($m = n$)	$\left(\frac{1}{2}\right)^{3m-2}$	$\left(\frac{1}{2}\right)^{2m-2}$

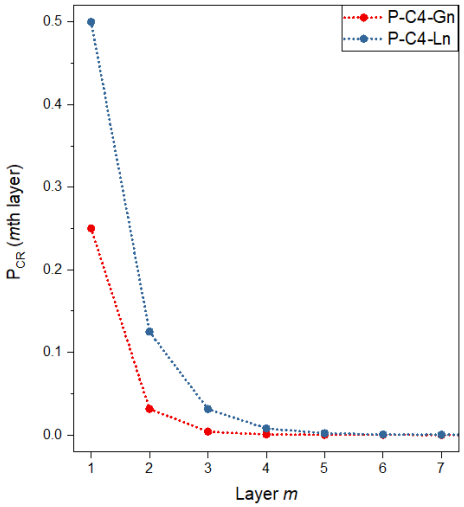

Figure 8. The probability of the electron arriving at the *m*th ($0<m<n$) layer and then returning to the apical viologen in the minimum possible number of steps in a dendritic network P−C4−G*n* and a linear array P−C4−L*n* as $P_{CR}(\text{dendron}) = (1/2)^{3m-1}$ and $P_{CR}(\text{linear}) = (1/2)^{2m-1}$.

4.3.2 Results and discussion

Transient absorption decay profiles of the P−C4−L system were recorded at 465 nm, the absorption maximum of $Py^{+\bullet}$, and 615 nm, the absorption maximum of $MV^{+\bullet}$, using 342 nm excitation (**Figure 9**). The rates for charge separation and instantaneous electron-hole recombination between pyrene and the first viologen moiety at the apex should be nearly identical for all generations in both P−C4−L and P−C4−$(V^{2+})_n$ families. In order to treat the data in a consistent manner and allow a direct comparison between linear and dendritic systems, all charge recombination profiles of P−C4−L1, P−C4−L2 and P−C4−L3 were fitted with a double exponential function with the condition of fixed value of τ_1 (**Figure 9** and **Table 5**, **6**).

The most pronounced difference between the decay dynamics in P−C4−$(V^{2+})_n$ dendrons and P−C4−L arrays can be observed through the comparison of their first

generations, since it is crucial that in the first generation the recombination at the apex has been avoided and the surviving electron travels further down the network through different pathways. In P−C4−G1, approximately 84.8% of the overall population of the CS state decays with $\tau_1 = 3.0$ ps. Because of the 1→2 branching of the dendron, the injected electron which escapes the immediate charge recombination has equal probability of hopping to either viologen unit in the second layer. Whereas, in P−C4−L1, there is only one hopping pathway for the injected electron locating at the first viologen. Since the rate for charge recombination occurring at the apex does not change in P−C4−L1, it would be expected that 91.8% of the overall population recombines on the same time scale τ_1 and the rest of 8.2% has one option of hopping to the second viologen, which is generally consistent with the experimental findings (**Table 5** and **6**).

Meanwhile, the connectivity of acceptors is closely related to electronic coupling between degenerate viologen sites. The electronic coupling between the LUMO orbitals of two viologens attached in *para* positions of a benzene ring is $|V_{LUMO\leftrightarrow LUMO}| = 15.6\ \text{cm}^{-1}$ (DFT calculations at the B3LYP 6-31G* level) and it increases to $36.0\ \text{cm}^{-1}$ when two viologens are linked to benzene in *meta* positions. The results suggest that in a linear array of viologens the rate of electron hopping between two sites should be expected to decrease by ~5 times. It should be mentioned that the DFT calculation of the complete *tris*(methyl viologen)benzene repeat unit indicates a much stronger electronic coupling with $|V_{LUMO\leftrightarrow LUMO}| = 100\sim200\ \text{cm}^{-1}$ which is difficult to precisely estimate because the triply substituted system undergoes spontaneous symmetry breaking in order to minimize the electrostatic repulsion among the viologen branches. Thus, the electron hopping rate in a linear array with 1→1 connectivity should be greatly slower than that in a corresponding

dendron. However, the recombination time constant $\tau_2 = 15.8\sim16.7$ ps in P−C4−L1 indicates that the "round trip" of electron hopping between apical viologen and the one in the first shell occurs at a time scale of 12.9~13.6 ps which is only ~1.3 times slower than 9.4~10.6 ps obtained for P−C4−G1. It is very possible that during the fitting for linear arrays the significantly small amplitude A_2 would lead to inaccurate and erroneous decay rates τ_2. In addition, since all DFT calculations were performed in vacuum where the electrostatic interaction with solvent molecules is not taken into consideration, more accurate computational calculations in acetonitrile are required.

Based on the knowledge of electron transfer kinetics in pyrene-viologen dendrons, the generation dependent extension of the average lifetime τ_2 from 16.3 ps in P−C4−L1 to 17.8 ps in P−C4−L2 and 23.1 ps in P−C4−L3 is an expected behavior (**Table 5** and **6**). The long-lived fraction of CS state, $A_2 + A_\infty$, increases from 7.5% in P−C4−L1 to 9.2% in P−C4−L2 and 10.7% in P−C4−L3. Compared with the situation in the P−C4−$(V^{2+})_n$ dendrons where the sum $A_2 + A_\infty$ grows from 15.2% in P−C4−G1 to 16.8% in P−C4−G2 and 19.7% in P−C4−G3 (**Table 1** and **2**), the linear P−C4−L system with 1→1 connectivity shows a weaker ability to intercept the population of the initial CS state. From another perspective, the ratio of A_∞ to the sum $A_2 + A_\infty$, which represents the proportion of CS state population "lost" in the network to the total population that escapes the instantaneous charge recombination, steadily increases from 15% in P−C4−L1 to 27% in P−C4−L2 and 28% in P−C4−L3. Whereas, in P−C4−$(V^{2+})_n$ dendrons, the ratio $A_\infty/(A_2 + A_\infty)$ grows significantly from 28% in P−C4−G1 to 33% in P−C4−G2 and 40% in P−C4−G3. Therefore, the injected electron which migrates beyond the apical viologen has a greater probability to be retained in the dendritic network of acceptors in comparison with the case

in the analogous linear arrays. This experimental finding is consistent with the conclusion drawn in the section **4.3.1**.

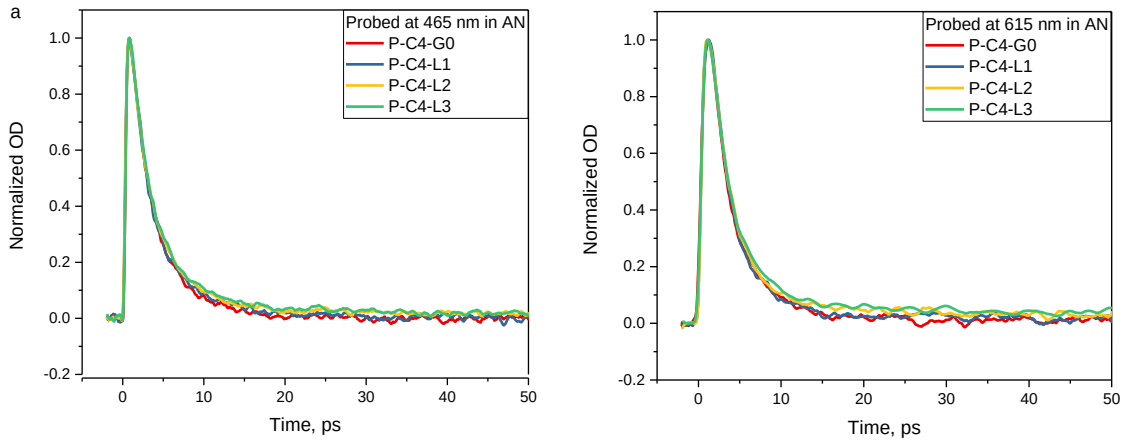

Figure 9. Transient absorption decay profiles of P−C4−L*n* recorded at (a) 465 nm, the absorption maximum of $Py^{+\bullet}$, and (b) 615 nm, the absorption maximum of $MV^{+\bullet}$.

Table 5. Fitting parameters for the decay of the $Py^{+\bullet}$ signal monitored at 465 nm for P−C4−L*n*.

Generation	τ_1, ps	A_1	τ_2, ps	A_2	A_∞	$A_2 + A_\infty$
P−C4−G0	3.1 ± 0.02	1.0	–	–	–	–
P−C4−L1	3.1 ± 0.0	0.935 ± 0.009	16.7 ± 1.9	0.061 ± 0.010	0.004 ± 0.002	0.065 ± 0.012
P−C4−L2	3.1 ± 0.0	0.913 ± 0.003	18.3 ± 1.8	0.069 ± 0.003	0.018 ± 0.001	0.087 ± 0.004
P−C4−L3	3.1 ± 0.0	0.901 ± 0.008	20.4 ± 3.0	0.079 ± 0.008	0.020 ± 0.001	0.099 ± 0.009

Table 6. Fitting parameters for the decay of the $MV^{+\bullet}$ signal monitored at 615 nm for P−C4−L*n*.

Generation	τ_1, ps	A_1	τ_2, ps	A_2	A_∞	$A_2 + A_\infty$
P−C4−G0	2.9 ± 0.03	0.985 ± 0.006	–	–	0.015 ± 0.001	–
P−C4−L1	2.9 ± 0.0	0.916 ± 0.034	15.8 ± 1.8	0.063 ± 0.035	0.021 ± 0.003	0.084 ± 0.038
P−C4−L2	2.9 ± 0.0	0.904 ± 0.005	17.3 ± 3.4	0.062 ± 0.003	0.034 ± 0.001	0.096 ± 0.004
P−C4−L3	2.9 ± 0.0	0.886 ± 0.016	25.7 ± 4.4	0.074 ± 0.016	0.040 ± 0.003	0.114 ± 0.019

4.4 Solvent effect on intramolecular electron transfer dynamics

In order to understand the electron transfer dynamics of pyrene-viologen dendrons in different environments, the solvent effect on charge separation and recombination

dynamics of P−C1−$(V^{2+})_n$ dendrons was investigated in propylene carbonate ($\varepsilon = 64$). Due to the polycationic character of viologen branches, only polar solvents can be used. In propionitrile ($\varepsilon = 27.2$) and DMSO ($\varepsilon = 46.7$), all dendrons show good solubility, but the baseline of the UV-Vis spectra of higher generations in the whole visible range is not zero for an unknown reason. In benzonitrile ($\varepsilon = 26.0$), two-photon excitation of the solvent while using the excitation of 345 nm leads to another problem. As a result, only acetonitrile and propylene carbonate, which differ considerably in polarity and viscosity, were used in this project.

The ground state absorption spectrum of P−C1−G0 in propylene carbonate shows nearly identical vibronic structure as that measured in acetonitrile (**Figure 10a**). The spectra of higher generations do not suggest a major conformational change caused by switching solvent from acetonitrile to the more polar propylene carbonate (**Figure 10b**).

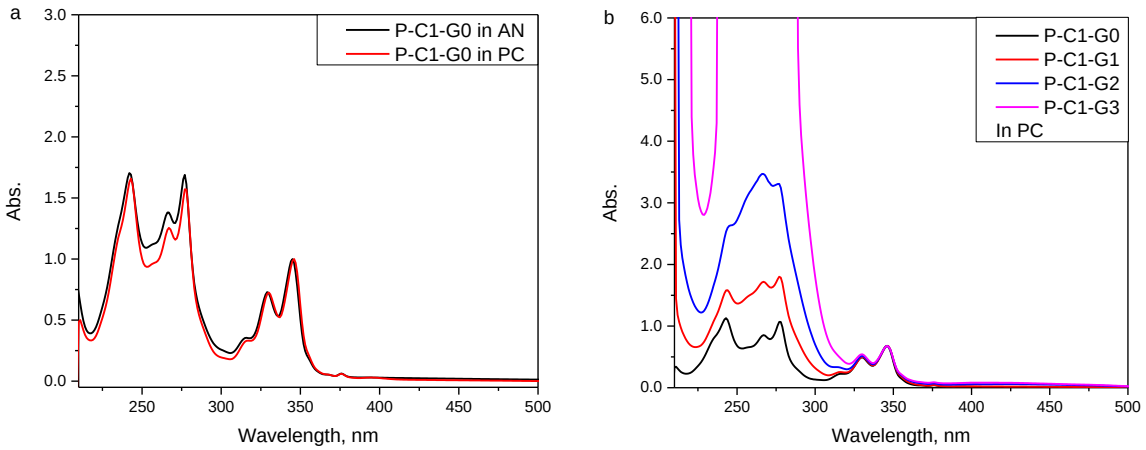

Figure 10. (a) Steady-state absorption spectrum of P−C1−G0 recorded at the concentration of 1.5 × 10^{-5} M in acetonitrile and propylene carbonate; (b) Steady-state absorption spectra of P−C1−$(V^{2+})_n$ dendrons dissolved in propylene carbonate.

The transient absorption spectrum of each member of P–C1–$(V^{2+})_n$ family in propylene carbonate also shows the characteristic broad absorption band of $MV^{+\bullet}$ and a sharper peak of $Py^{+\bullet}$ (**Figure 11**). The absorption band of $MV^{+\bullet}$ in propylene carbonate does appear to be somewhat broader and the whole spectrum is red-shifted by ~12 nm, probably due to reduced electrostatic repulsion between the $Py^{+\bullet}$ and the positively charged viologen network.

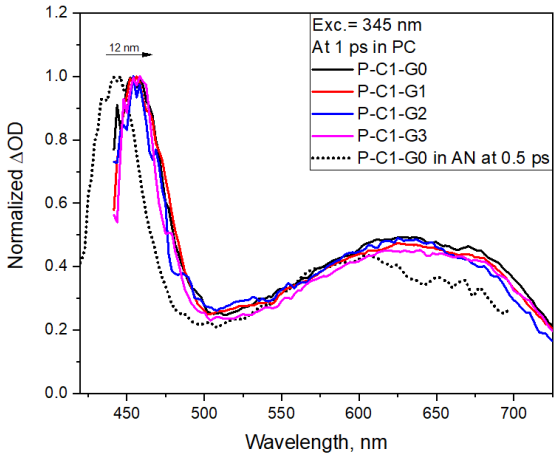

Figure 11. Normalized transient absorption spectra of P–C1–$(V^{2+})_n$ dendrons. All spectra were recorded at 1 ps delay following 345 nm excitation of 1.5×10^{-5} M solutions in propylene carbonate.

Time profiles were obtained at the probe wavelengths of 465 and 615 nm for all P–C1–$(V^{2+})_n$ dendrons in propylene carbonate (**Figure 12**). The double exponential function was applied to fit the decay curves, and the fitting results are summarized in **Table 7** and **8**. The interpretation of all fitting parameters is the same as that in the case of acetonitrile (see section **3.3**). Generally, in propylene carbonate, both time constants, $\tau_1 = 2.4\sim2.6$ ps and $\tau_2 = 15\sim29$ ps, are much slower compared with $\tau_1 = 0.7\sim0.8$ ps and $\tau_2 = 6\sim10$ ps obtained in acetonitrile, which suggests a strong solvent effect on electron transfer dynamics in the pyrene-viologen systems.

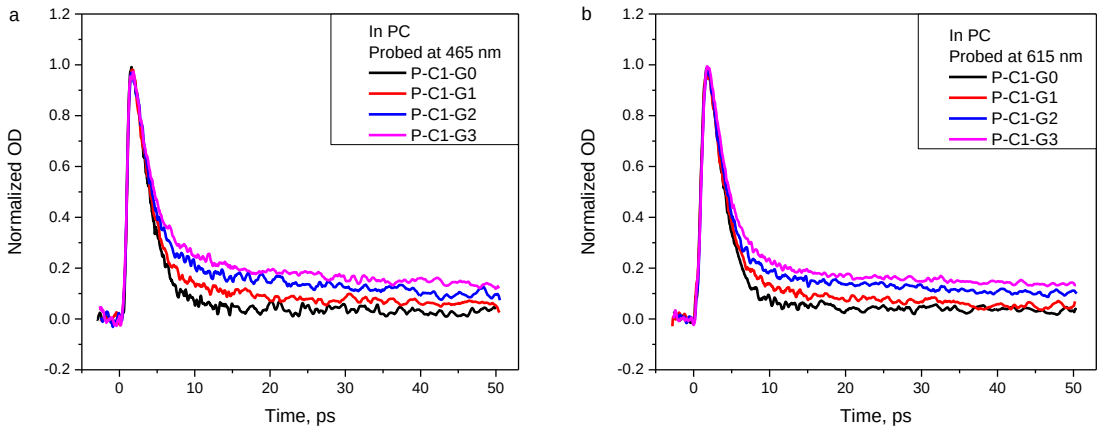

Figure 12. Transient absorption decay profiles of P–C1–$(V^{2+})_n$ dendrons in propylene carbonate recorded at (a) 465 nm, the absorption maximum of $Py^{+\bullet}$, and (b) 615 nm, the absorption maximum of $MV^{+\bullet}$.

Table 7. Fitting parameters for the decay of the $Py^{+\bullet}$ signal monitored at 465 nm for P–C1–$(V^{2+})_n$ dendrons in propylene carbonate.

Generation	τ_1, ps	A_1	τ_2, ps	A_2	A_∞	$A_2 + A_\infty$
P-C1-G0	2.5 ± 0.02	0.962 ± 0.004	–	–	0.038 ± 0.001	0.038 ± 0.001
P-C1-G1	2.5 ± 0.07	0.869 ± 0.021	15.9 ± 1.9	0.062 ± 0.013	0.069 ± 0.012	0.131 ± 0.025
P-C1-G2	2.5 ± 0.08	0.805 ± 0.021	24.8 ± 1.6	0.103 ± 0.045	0.092 ± 0.035	0.195 ± 0.080
P-C1-G3	2.5 ± 0.11	0.719 ± 0.029	28.9 ± 5.9	0.132 ± 0.011	0.149 ± 0.027	0.281 ± 0.027

Table 8. Fitting parameters for the decay of the $MV^{+\bullet}$ signal monitored at 615 nm for P–C1–$(V^{2+})_n$ dendrons in propylene carbonate.

Generation	τ_1, ps	A_1	τ_2, ps	A_2	A_∞	$A_2 + A_\infty$
P-C1-G0	2.4 ± 0.02	0.957 ± 0.004	–	–	0.043 ± 0.001	0.043 ± 0.001
P-C1-G1	2.5 ± 0.03	0.885 ± 0.014	15.2 ± 1.4	0.047 ± 0.027	0.068 ± 0.046	0.115 ± 0.073
P-C1-G2	2.5 ± 0.02	0.827 ± 0.013	22.4 ± 1.0	0.052 ± 0.026	0.121 ± 0.037	0.173 ± 0.063
P-C1-G3	2.6 ± 0.01	0.790 ± 0.007	26.6 ± 2.2	0.075 ± 0.016	0.135 ± 0.022	0.210 ± 0.038

Three electron-transfer processes are of primary importance: the charge separation between pyrene and the first viologen, the electron hopping among degenerate viologen sites, and the final charge recombination to the ground state. The ~3.5 times slower

recombination rates detected in propylene carbonate for all P−C1−$(V^{2+})_n$ dendrons are surprising considering that an increase in solvent polarity should lead to an increased reorganization energy and hence accelerate the electron transfer reaction occurring in the Marcus "inverted region". In fact, the solvent reorganization energy in the continuum model is proportional to $(1/\varepsilon_{op} - 1/\varepsilon_{st})$ where ε_{st} and ε_{op} are static and optical dielectric constants, respectively (**Table 9**). When the contribution of optical dielectric constant is taken into consideration, one can find that the reorganization energy for charge separation and recombination in propylene carbon is smaller than that obtained in acetonitrile (**Table 10**). Therefore, the rates for both charge separation and initial recombination are expected to be slower in the presence of propylene carbonate (**Figure 13a** and **b**).

Table 9. Solvent properties of the acetonitrile and propylene carbonate at room temperature.

Solvent	Static dielectric constant ε_s	Optical dielectric constant ε_o	Refractive index n	Viscosity η, mPa·s [40]	Dipole moment, D
Acetonitrile	36.6	1.81	1.3442	0.334	3.9
Propylene carbonate	64.9	2.01	1.4189	2.4	4.9

Table 10. Thermodynamic parameters calculated in the presence of two solvents.

Solvent	$-\Delta G^0{}_{CS}$, eV	$-\Delta G^0{}_{CR}$, eV	λ, eV	λ_{hop}, eV
Acetonitrile	1.69	1.61	1.27	1.35
Propylene carbonate	1.71	1.59	1.18	1.26

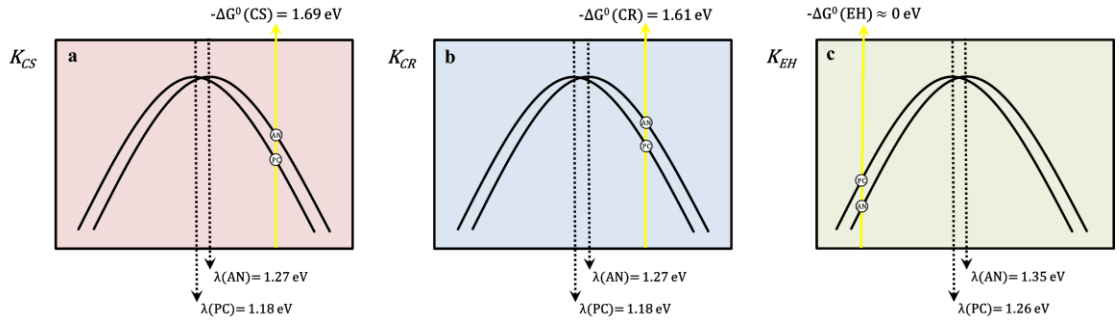

Figure 13. Change of charge separation rate (a), recombination rate (b), and electron hopping rate (c) by switching the solvent from acetonitrile to propylene carbonate.

In ordet to examine the solvent effect on charge separation rate, the rising and initial decaying region of the kinetic traces recorded for P−C1−G0 in both solvents was fitted using a double exponential function (**Figure 14**). The time constant τ_f with a negative amplitude indicates that the charge separation at the apex in propylene carbonate occurs within 390 fs which is significantly slower than 38~76 fs obtained in acetonitrile. The 5~10 fold change in τ_f cannot be fully interpreted by applying Marcus theory considering only 0.09 eV change in reorganization energy.

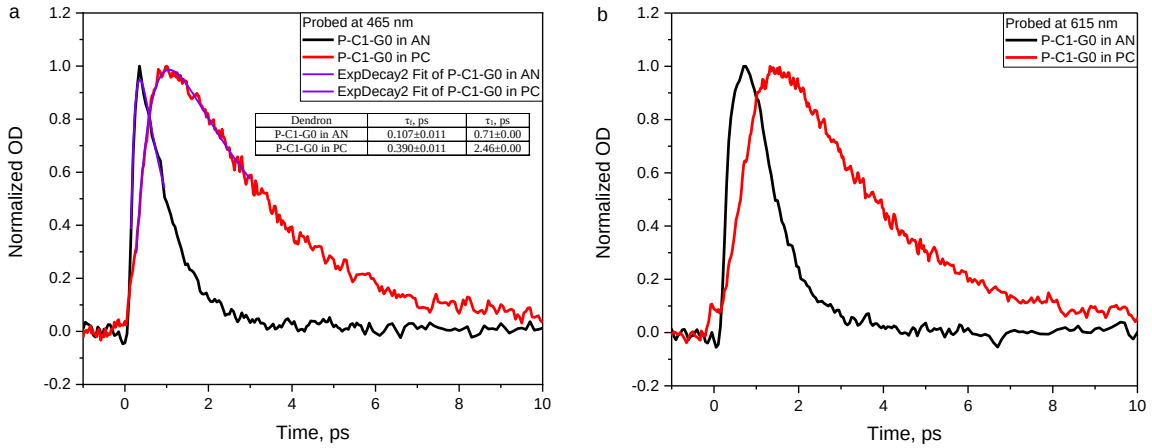

Figure 14. The comparison of transient absorption decay profiles of P−C1−G0 in acetonitrile and propylene carbonate probed at (a) 465 nm, the absorption of $Py^{+\bullet}$, and (b) 615 nm, the absorption of $MV^{+\bullet}$. The inset shows the biexponential fitting parameters for the rising and initial decaying part of the kinetic traces.

As for the electron hopping taking places in the Marcus "normal region", the hopping rate detected in propylene carbonate is expected to be faster due to a smaller reorganization energy (**Figure 13c** and **Table 10**). The time constant, $\tau_2 = 15{\sim}29$ ps, consists of the electron hopping along the viologen branches and the final charge recombination occurring at a time constant of $\tau_1 = 2.4{\sim}2.6$ ps. Thus, the electron hopping

between degenerate viologen sites occurs on the time scale of 13~26 ps in propylene carbonate which is significantly slower than 5.4~9.3 ps observed in acetonitrile. The inconsistence between experimental results and Marcus theory predictions warrants the consideration of other factors which can slow down the electron hopping process in propylene carbonate.

Acetonitrile and propylene carbonate differ in several physical parameters: molecular size, dipole moment, dielectric relaxation time, and viscosity (**Table 9**). The changes in these quantities can influence the electron transfer rates. Considering the 7-fold increase in viscosity by switching the solvent from acetonitrile to propylene carbonate, the most likely relevant parameter is the solvent viscosity. The influence of solvent viscosity on electron transfer rates has been observed in numerous systems where a large-amplitude motion of parts of the molecule takes place [41-44]. The geometry of the ground state MV^{2+} can be described by two aromatic pyridyl rings connected by a single bond in a highly twisted conformation with an interplanar angle of 30~40° depending on solvent. Whereas, its radical cation, $MV^{+\bullet}$, is characterized by a planar geometry with a strengthened inter-ring bond [45-47]. The conformational interconversion between MV^{2+} and $MV^{+\bullet}$ involves a rapid rotation about the inter-ring carbon-carbon bond which is hindered by the surrounding viscous propylene carbonate. The electron transfer rate is inversely proportional to a fractional power of solvent viscosity as $k \propto \eta^{-\alpha}$ where the value of the power dependence α is typically between 0 and 1 [48]. Based on the times scales of electron hopping in two solvents, $\alpha = 0.38$ is derived. The viscosity effects are most pronounced, however, any solvation process is slower in a viscous solvent, even the solvation of $Py^{+\bullet}$ takes more time in propylene carbonate than in acetonitrile.

4.5 Conclusion

In the P−C1−$(V^{2+})_n$ dendrons, the very short donor-acceptor separation results in a rapid charge recombination rate which dramatically reduces the fraction of surviving electrons that migrate into the dendritic network of viologens. In order to move the system away from the limitation of $k_{CR} \gg k_{hop}$, a new family of P−C4−$(V^{2+})_n$ dendrons in which the intervening bridge is extended by four methylenes has been synthesized. An increase in the distance between pyrene and the attached the apical viologen significantly slows the rates for both charge separation and recombination occurring at the apex by ~4 times, which is attributed to a combination result of decreasing electronic coupling and increasing solvent reorganization energy. It has been shown in the previous chapter that the branched multiacceptor structures inherently favor the outward flow of electrons away from the apex. This hypothesis is supported by electron transfer kinetics observed in an analogous P−C4−L system where a series of linear arrays of viologen units is employed. Due to the 1→1 connectivity, the linear system shows weaker ability to intercept the population of the initial CS state as well as a weaker ability to retain the injected electron within the system. Meanwhile, the lower electronic coupling between two degenerate viologen units in the *para* configuration decreases the electron hopping rate observed in P−C4−L system. Lastly, the solvent effect on intramolecular electron transfer dynamics was investigated in acetonitrile and propylene carbonate. The rates for charge separation, recombination and electron hopping are slowed down in propylene carbonate due to pronounced viscosity effect. In conclusion, the electron transfer dynamics in pyrene-viologen donor-acceptor systems shows a strong dependence on the distance between donor and acceptor, the connectivity of acceptors, and the surrounding medium. The detailed knowledge of this

dependence is essential for understanding the mechanisms of photochemical processes and obtaining guidelines for the control of reactions.

4.6 References

1. Closs, G. L.; Calcaterra, L. T.; Green, N. J.; Penfield, K. W.; Miller, J. R., Distance, stereoelectronic effects, and the Marcus inverted region in intramolecular electron transfer in organic radical anions. *The Journal of Physical Chemistry* **1986,** *90* (16), 3673-3683.

2. Closs, G. L.; Miller, J. R., Intramolecular Long-Distance Electron Transfer in Organic Molecules. *Science* **1988,** *240* (4851), 440-447.

3. Yonemoto, E. H.; Saupe, G. B.; Schmehl, R. H.; Hubig, S. M.; Riley, R. L.; Iverson, B. L.; Mallouk, T. E., Electron-Transfer Reactions of Ruthenium Trisbipyridyl-Viologen Donor-Acceptor Molecules: Comparison of the Distance Dependence of Electron Transfer-Rates in the Normal and Marcus Inverted Regions. *Journal of the American Chemical Society* **1994,** *116* (11), 4786-4795.

4. Davis, W. B.; Wasielewski, M. R.; Ratner, M. A.; Mujica, V.; Nitzan, A., Electron Transfer Rates in Bridged Molecular Systems: A Phenomenological Approach to Relaxation. *The Journal of Physical Chemistry A* **1997,** *101* (35), 6158-6164.

5. Le, T. P.; Rogers, J. E.; Kelly, L. A., Photoinduced Electron Transfer in Covalently Linked 1,8-Naphthalimide/Viologen Systems. *The Journal of Physical Chemistry A* **2000,** *104* (29), 6778-6785.

6. Paddon-Row, M. N., Orbital interactions and long-range electron transfer. 2003; pp 1-85.

7. Weiss, E. A.; Tauber, M. J.; Kelley, R. F.; Ahrens, M. J.; Ratner, M. A.; Wasielewski, M. R., Conformationally Gated Switching between Superexchange and Hopping within Oligo-p-phenylene-Based Molecular Wires. *Journal of the American Chemical Society* **2005,** *127* (33), 11842-11850.

8. Benniston, A.; Harriman, A., Controlling electron exchange in molecular assemblies. *Coordin Chem Rev* **2008,** *252* (23-24), 2528-2539.

9. Goldsmith, R. H.; DeLeon, O.; Wilson, T. M.; Finkelstein-Shapiro, D.; Ratner, M. A.; Wasielewski, M. R., Challenges in Distinguishing Superexchange and Hopping Mechanisms of Intramolecular Charge Transfer through Fluorene Oligomers. *The Journal of Physical Chemistry A* **2008,** *112* (19), 4410-4414.

10. Elicker, T. S.; Evans, D. G., Electron Dynamics in Dendrimers. *The Journal of Physical Chemistry A* **1999,** *103* (47), 9423-9431.

11. Lukas, A. S.; Miller, S. E.; Wasielewski, M. R., Femtosecond Optical Switching of Electron Transport Direction in Branched Donor-Acceptor Arrays. *The Journal of Physical Chemistry B* **2000,** *104* (5), 931-940.

12. Elicker, T. S.; Binette, J.-S.; Evans, D. G., Topological Effects in Electron Transfer: Applications to Dendrimers and Branched Molecules. *The Journal of Physical Chemistry B* **2001,** *105* (2), 370-378.

13. Kalyanaraman, C.; Evans, D. G., Molecular Conductance of Dendritic Wires. *Nano Letters* **2002,** *2* (5), 437-441.

14. Solomon, G. C.; Andrews, D. Q.; Van Duyne, R. P.; Ratner, M. A., Electron Transport through Conjugated Molecules: When the π System Only Tells Part of the Story. *Chemphyschem* **2009,** *10* (1), 257-264.

15. Crawford, M. K.; Wang, Y.; Eisenthal, K. B., Effects of conformation and solvent polarity on intramolecular charge transfer: a picosecond laser study. *Chem Phys Lett* **1981,** *79* (3), 529-533.

16. Miller, J. R.; Calcaterra, L. T.; Closs, G. L., Intramolecular long-distance electron transfer in radical anions. The effects of free energy and solvent on the reaction rates. *Journal of the American Chemical Society* **1984,** *106* (10), 3047-3049.

17. Rips, I.; Jortner, J., Dynamic solvent effects on outer-sphere electron transfer. *The Journal of Chemical Physics* **1987,** *87* (4), 2090-2104.

18. Maroncelli, M.; Macinnis, J.; Fleming, G. R., Polar Solvent Dynamics and Electron-Transfer Reactions. *Science* **1989,** *243* (4899), 1674-1681.

19. Heitele, H., Dynamic Solvent Effects on Electron-Transfer Reactions. *Angewandte Chemie International Edition in English* **1993,** *32* (3), 359-377.

20. Johnson, M. D.; Miller, J. R.; Green, N. S.; Closs, G. L., Distance dependence of intramolecular hole and electron transfer in organic radical ions. *The Journal of Physical Chemistry* **1989,** *93* (4), 1173-1176.

21. Tung, C.-H.; Zhang, L.-P.; Li, Y.; Cao, H.; Tanimoto, Y., Intramolecular Long-Distance Electron Transfer and Triplet Energy Transfer. Photophysical and Photochemical Studies on a Norbornadiene-Steroid-Benzidine System. *Journal of the American Chemical Society* **1997,** *119* (23), 5348-5354.

22. Paddon-Row, M. N.; Shephard, M. J., Through-Bond Orbital Coupling, the Parity Rule, and the Design of "Superbridges" Which Exhibit Greatly Enhanced Electronic Coupling: A Natural Bond Orbital Analysis. *Journal of the American Chemical Society* **1997,** *119* (23), 5355-5365.

23.Paddon-Row, M. N., Investigating long-range electron-transfer processes with rigid, covalently linked donor-(norbornylogous bridge)-acceptor systems. *Accounts of Chemical Research* **2002,** *27* (1), 18-25.

24. Schanze, K. S.; Cabana, L. A., Distance dependence of photochemical electron transfer across peptide spacers. *The Journal of Physical Chemistry* **1990,** *94* (7), 2740-2743.

25. Isied, S. S.; Ogawa, M. Y.; Wishart, J. F., Peptide-mediated intramolecular electron transfer: long-range distance dependence. *Chem Rev* **1992,** *92* (3), 381-394.

26. Turro, N. J.; Ramamurthy, V.; Scaiano, J. C. *Principles of Molecular Photochemistry: An Introduction*; University Science Publishers: New York, **2008**; pp 442-445.

27. Hoffmann, R., Interaction of orbitals through space and through bonds. *Accounts of Chemical Research* **2002,** *4* (1), 1-9.

28. Paulson, B. P.; Curtiss, L. A.; Bal, B.; Closs, G. L.; Miller, J. R., Investigation of Through-Bond Coupling Dependence on Spacer Structure. *Journal of the American Chemical Society* **1996,** *118* (2), 378-387.

29. Kapturkiewicz, A.; Herbich, J.; Karpiuk, J.; Nowacki, J., Intramolecular Radiative and Radiationless Charge Recombination Processes in Donor−Acceptor Carbazole Derivatives. *The Journal of Physical Chemistry A* **1997,** *101* (12), 2332-2344.

30. Nelsen, S. F.; Tran, H. Q., Solvent Effects on Electronic Coupling between Dialkylamino Groups in Aromatic Diamine Radical Cations. *The Journal of Physical Chemistry A* **1999,** *103* (41), 8139-8144.

31. Ratera, I.; Sporer, C.; Ruiz-Molina, D.; Ventosa, N.; Baggerman, J.; Brouwer, A. M.; Rovira, C.; Veciana, J., Solvent Tuning from Normal to Inverted Marcus Region of

Intramolecular Electron Transfer in Ferrocene-Based Organic Radicals. *Journal of the American Chemical Society* **2007,** *129* (19), 6117-6129.

32. Nau, W. M.; Pischel, U., "Inverted" Solvent Effect on Charge Transfer in the Excited State. *Angewandte Chemie International Edition* **1999,** *38* (19), 2885-2888.

33. Fujitsuka, M.; Tsuboya, N.; Hamasaki, R.; Ito, M.; Onodera, S.; Ito, O.; Yamamoto, Y., Solvent Polarity Dependence of Photoinduced Charge Separation and Recombination Processes of Ferrocene-C_{60} Dyads. *The Journal of Physical Chemistry A* **2003,** *107* (10), 1452-1458.

34. Wan, J.; Ferreira, A.; Xia, W.; Chow, C. H.; Takechi, K.; Kamat, P. V.; Jones, G.; Vullev, V. I., Solvent dependence of the charge-transfer properties of a quaterthiophene-anthraquinone dyad. *Journal of Photochemistry and Photobiology A: Chemistry* **2008,** *197* (2-3), 364-374.

35. Hyun, B.-R.; Bartnik, A. C.; Lee, J.-K.; Imoto, H.; Sun, L.; Choi, J. J.; Chujo, Y.; Hanrath, T.; Ober, C. K.; Wise, F. W., Role of Solvent Dielectric Properties on Charge Transfer from PbS Nanocrystals to Molecules. *Nano Letters* **2010,** *10* (1), 318-323.

36. El-Khouly, M. E.; Jaggi, M.; Schmid, B.; Blum, C.; Liu, S.-X.; Decurtins, S.; Ohkubo, K.; Fukuzumi, S., Annulation of Tetrathiafulvalene to the Bay Region of Perylenediimide: Fast Electron-Transfer Processes in Polar and Nonpolar Solvents. *The Journal of Physical Chemistry C* **2011,** *115* (16), 8325-8334.

37. Al-Subi, A. H.; Niemi, M.; Tkachenko, N. V.; Lemmetyinen, H., Quantitative Analysis of Intramolecular Exciplex and Electron Transfer in a Double-Linked Zinc Porphyrin-Fullerene Dyad. *The Journal of Physical Chemistry A* **2012,** *116* (39), 9653-9661.

38. Kawauchi, T.; Oguchi, Y.; Nagai, K.; Iyoda, T., Conical Gradient Junctions of Dendritic Viologen Arrays on Electrodes. *Sci Rep-Uk* **2015,** *5*.

39. Kawauchi, T.; Oguchi, Y.; Sawayama, J.; Nagai, K.; Iyoda, T., Microwave-Assisted Synthesis of Dendritic Viologen-Arranged Molecules with an ω-Mercaptoalkyl Group and Their Self-Assembled Monolayers Complexed with Various Anions. *Macromolecules* **2015,** *48* (22), 8090-8097.

40. Moumouzias, G.; Panopoulos, D. K.; Ritzoulis, G., Excess properties of the binary liquid system propylene carbonate + acetonitrile. *Journal of Chemical & Engineering Data* **1991,** *36* (1), 20-23.

41. Finckh, P.; Heitele, H.; Michel-Beyerle, M. E., Intramolecular electron transfer in viscous solution. *Chemical Physics* **1989,** *138* (1), 1-10.

42. Vauthey, E.; Phillips, D., Viscosity effect on the rate of back electron transfer within a short-lived exciplex. *Chemical Physics* **1990,** *147* (2-3), 421-430.

43. Feng, C.; Kedia, R. V.; Hazzard, J. T.; Hurley, J. K.; Tollin, G.; Enemark, J. H., Effect of Solution Viscosity on Intramolecular Electron Transfer in Sulfite Oxidase†. *Biochemistry-Us* **2002,** *41* (18), 5816-5821.

44. Grabowski, Z. R.; Rotkiewicz, K.; Rettig, W., Structural Changes Accompanying Intramolecular Electron Transfer: Focus on Twisted Intramolecular Charge-Transfer States and Structures. *Chem Rev* **2003,** *103* (10), 3899-4032.

45. Hofmann, H.-J.; Cimiraglia, R.; Tomasi, J., On the conformation of bipyridine dications and cation radicals. *Journal of Molecular Structure: THEOCHEM* **1986,** *139* (3-4), 213-219.

46. Ould-Moussa, L.; Poizat, O.; Castellà-Ventura, M.; Buntinx, G.; Kassab, E., Ab Initio Computations of the Geometrical, Electronic, and Vibrational Properties of the Ground State, the Anion Radical, and theN,N‘-Dihydro Cation Radical of 4,4‘-Bipyridine Compared to Transient Raman Spectra. *The Journal of Physical Chemistry* **1996,** *100* (6), 2072-2082.

47. Benniston, A. C.; Harriman, A.; Li, P.; Rostron, J. P.; Harrington, R. W.; Clegg, W., A Spectroscopic Study of the Reduction of Geometrically Restrained Viologens. *Chemistry - A European Journal* **2007,** *13* (28), 7838-7851.

48. Velsko, S. P.; Fleming, G. R., Solvent influence on photochemical isomerizations: Photophysics of DODCI. *Chemical Physics* **1982,** *65* (1), 59-70

Chapter 5. Vibrational Relaxation Dynamics of Photoexcited Methyl Viologen Radical Cation in Solution

The ultrafast charge separation and recombination in the pyrene-viologen diad brought out the importance of electron transfer occurring in not fully thermally and librationally equilibrated systems. In order to better understand these processes, vibrational cooling of hot methyl viologen radical cation ($MV^{+\bullet}$) was studied using femtosecond pump-probe spectroscopy. The photoexcitation of the $D_1 \leftarrow D_0$ transition led to very rapid internal conversion within 460 fs, generating a vibrationally excited ground state of $MV^{+\bullet}$ which thermalized on 1.6~16 ps time scale. The initial stage of vibrational excess energy loss corresponds to the intermolecular energy transfer to vibrational modes of the surrounding medium molecules, and the latter stage involves energy dissipation into relatively low-frequency librational and translational modes of the solvent. The effect of solvent and host-guest complexation on cooling dynamics of $MV^{+\bullet}$ was also investigated, and the results suggested that a good match between the density of vibrational states in $MV^{+\bullet}$ and surrounding medium could efficiently accelerate the vibrational cooling.

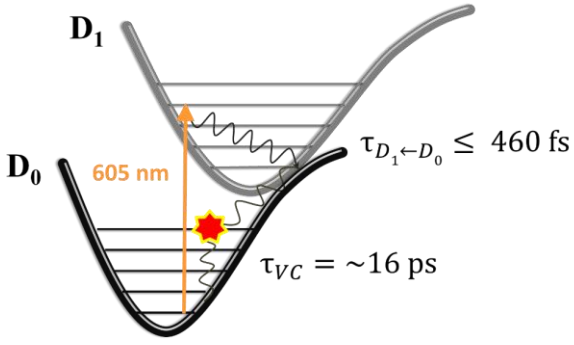

Figure 1. Energy level scheme accounting for the excited-state dynamics of $MV^{+\bullet}$ and assignment of the measured time constants.

5.1 Introduction

5.1.1 Vibrational relaxation of hot molecules

Vibrational relaxation in condensed phase is an essential dynamical process in which the population distribution in the high energy level of vibrational states returns to its thermodynamic equilibrium. For numerous processes in solution, such as photo-isomerization [1] and electron transfer reactions [2], the relative rate for coupling energy into the reaction coordinate to the vibrational relaxation rate determines the reaction rates, pathways, and product yields [3]. Therefore, vibrational relaxation has attracted considerable interest on both experimental [4-5] and theoretical sides [6-8]. The studies are focused primarily on the energy or population relaxation timescales associated with particular vibrational states. The development of ultrafast laser techniques has allowed direct study of a wide range of vibrational states and the identification of different relaxation mechanisms [9-11]. Meanwhile, the enhanced computational capabilities have permitted simulations of realistic liquid models [12].

The absorption of light by a polyatomic molecule can result in the population of an electronically excited state that is vibrationally excited. The large amount excess excitation energy residing in an individual “hot” molecule undergoes vibrational relaxation (VR) which involves two processes: intramolecular vibrational redistribution (IVR) and vibrational cooling (VC). IVR is the primary intramolecular process in which the initially populated state is rapidly redistributed over other isoenergetic states even in the absence of an external perturbation usually occurring on the time scale of 25 fs to a few picoseconds [13]. This fast randomization of excess energy is due to the strong anharmonic couplings of vibrational levels and their high density of states [14]. After IVR, the molecular

temperature can in principle be very high but is often not reached because of VC. The vibrationally hot molecules cool by transferring energy to various motions of the surrounding medium until thermal equilibrium is achieved. The time constants of VC lie in the range between 5 to 50 ps depending on the amount of excess energy and the specific properties of the surrounding medium [4-5].

The vibrational relaxation has been investigated extensively in the vibrationally excited aromatic molecules [5, 15-18] such as azulene. In 1955, Beer and Higgins firstly recognized the anomalous light emission of S_1 state of azulene [19]. In the following years, a large number of picosecond laser studies showed that radiationless decay from S_1 to ground state took places in less than 1 ps and the resulting hot ground state of azulene relaxed with a time constant up to 40 ps [20-21]. In 1996, Bearpark reported computational calculations that found a low-lying conical intersection between S_0 and S_1 potential energy surfaces which explained the ultrafast $S_1 \leftarrow S_0$ internal conversion and the formation of vibrationally hot ground state of azulene [22].

5.1.2 Introduction of methyl viologen radical cation

The methyl viologen (1,1′-dimethyl-4,4′-bipyridinium, MV^{2+}) plays an important role in numerous light-induced electron-transfer reactions due to its electrochromic properties and their ability to accept electrons [23]. As a result, it has attracted considerable attention for its wide use in light-driven molecular devices based on switching between the MV^{2+} and its reduced form $MV^{+\bullet}$ (**Scheme 1**) [24-25]. In all these applications, excited states of $MV^{+\bullet}$ may be generated via thermal excitation during the electron or energy transfer reactions such like in the case of pyrene-viologen systems (see **Chapter 3** and **4**).

Therefore, detailed knowledge of excited methyl viologen radical cation is essential for understanding the mechanisms of relevant photochemical processes.

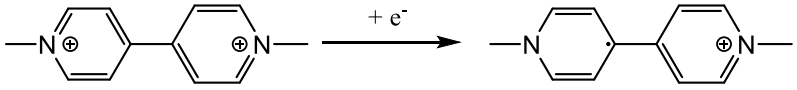

Scheme 1. One-reduction of the methyl viologen dication to the methyl viologen radical cation.

Häupl *et al.* [26] determined that the D_1 excited state of $MV^{+\bullet}$ has a lifetime of 700 fs in acetonitrile (< 350 fs in water [27]) and decays with the formation of vibrationally hot ground state which thermalizes on a slower ~15 ps time scale (~5 ps in water [27]). Further understanding the vibrational relaxation in excited $MV^{+\bullet}$ can open interesting perspectives for influencing or eventually controlling the dynamics of relevant ultrafast reactions in solution. In this project, the effect of solvent and host-guest complexation on VR dynamics of $MV^{+\bullet}$ was investigated in acetonitrile, propylene carbonate and in a complex with a crown ether (**Figure 2**).

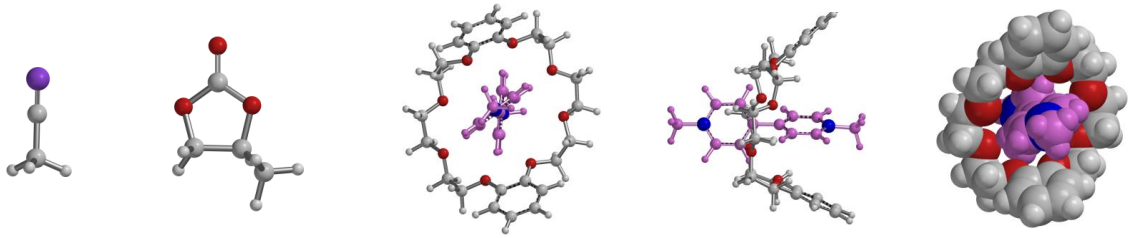

Figure 2. From left to right: acetonitrile (AN), propylene carbonate (PC) and three views of the methyl viologen encapsulated within the dibenzo-24-crown-8 (crown ether) host. Structures optimized in Spartan'14 at the AM1 semi empirical level.

5.2 Sample preparation

Acetonitrile (≥99.9%, Sigma-Aldrich) and propylene carbonate (anhydrous, 99.7%, Sigma-Aldrich) were degassed using the freeze-pump-thaw method. A saturated solution of methyl viologen dichloride (~1.40×10^{-4} M, 98%, Sigma-Aldrich) was prepared with degassed solvent and rest for 24 h. The suspension solution, containing 1.0 mg of zinc granule (20 mesh, ACROS Organics) and 3 mL of saturated methyl viologen (MV^{2+}) solution, was obtained by sonication for 2 h [28]. The dark blue color of mono-reduced methyl viologen ($MV^{+\bullet}$) was observed. Then, 500 μL of $MV^{+\bullet}$ solution was pipetted into 3 mL of degassed solvent for dilution and transferred into a standard quartz cuvette with the airtight valve. The entire sample preparation was performed under inert atmosphere in a glove box. In these conditions, approximately 70% of MV^{2+} species was reduced in the freshly-made sample. The dibenzo-24-crown-8 (98%, Sigma-Aldrich) was dissolved in deaerated acetonitrile solutions and formed host-guest complexation with $MV^{+\bullet}$ in 10-fold molar excess.

5.3 Results and discussion

5.3.1 Steady-state spectroscopy

The steady-state absorption spectrum of $MV^{+\bullet}$ is characterized by two well-defined bands (**Figure 3**). The broad absorption band spanning nearly the entire visible range from 450 to 800 nm is attributed to the $D_1 \leftarrow D_0$ transition. In the ultraviolet region, the much sharper absorption band peaking at 395 nm belongs to $D_2 \leftarrow D_0$ transition. No dimerization of $MV^{+\bullet}$ in CH_3CN was observed at the centration of 2×10^{-5} M employed in this study.

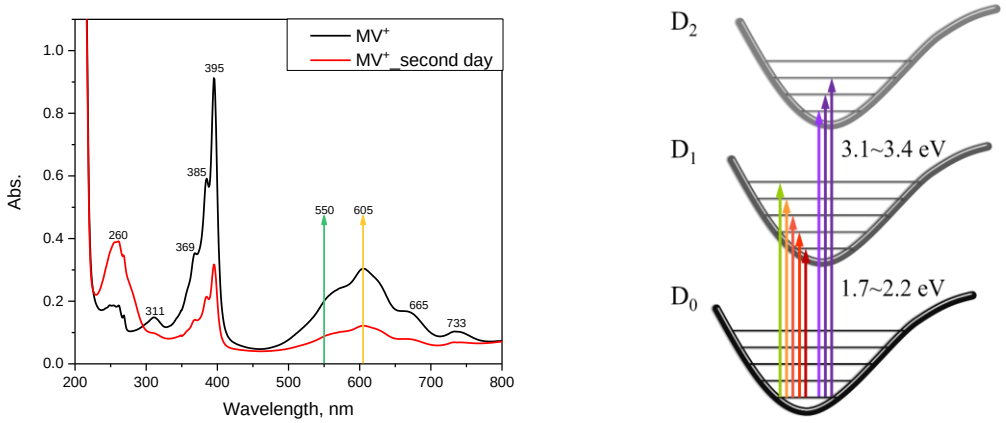

Figure 3. Ground state absorption spectrum of $MV^{+\bullet}$ in CH_3CN (2×10^{-5} M) measured at two successive days (left), and the energy level diagrams of $MV^{+\bullet}$ (right). The arrows in UV-Vis spectrum indicate the excitation wavelengths used in the pump-probe experiments.

$MV^{+\bullet}$ is stable for many days at room-temperature in acetonitrile solution in a glove box filled with nitrogen but degrades to MV^{2+} slowly during the experiments judging from the diminishing absorbance at 397 and 607 nm as well as the increase at 260 nm which corresponds to the absorption of MV^{2+} (**Figure 3**). Given the molar extinction coefficients of the methyl viologen and its radical cation in acetonitrile (**Table 1**), one can calculate that approximately 70% of MV^{2+} species was reduced in the freshly made sample. After 24 h, nearly 27% of $MV^{+\bullet}$ was survived. No fluorescence was detected at room temperature which suggests rapid $D_1 \leftarrow D_0$ internal conversion.

Table 1. Peak wavelengths and molar extinction coefficients for MV^{2+} and $MV^{+\bullet}$ in CH_3CN [29].

λ_{max}, nm	ε (MV^{2+}), $M^{-1}\,cm^{-1}$	ε ($MV^{+\bullet}$), $M^{-1}\,cm^{-1}$
260	20400±200	–
397	–	41800±800
607	–	13900±300

5.3.2 Transient absorption spectrum of the vibrationally hot electronic ground state of $MV^{+\bullet}$

Photoexcitation of $MV^{+\bullet}$ at 550 and 605 nm (**Figure 3**) results in the transitions to different vibrational states of the D_1 state. The population in the D_1 state undergoes rapid internal conversion generating a vibrationally excited ground state of $MV^{+\bullet}$ [26].

In pure acetonitrile, the obtained transient absorption (TA) spectrum of the hot ground state is strongly red shifted relative to that of the ground state and the sharp vibronic structure persists for tens of picoseconds (**Figure 4**). It should be noted that the appearance of multiple fine-structure peaks does not suggest favorable population of a particular mode. Considering the large density of vibrational modes of $MV^{+\bullet}$ in the range of 500~1600 cm^{-1} [30-32], it is likely that the population cascades from higher to lower states without any significant mode selectivity. However, due to spectroscopic selection rules, only the transitions of asymmetric skeletal stretching modes are likely to be observed in the TA spectra of hot ground state. In addition, the detected TA reflects the difference between the absorbance of the fully relaxed and vibrationally excited ground state, which may also give rise to the sharp vibronic features in the 650~800 nm region.

In all three media, the information on the distribution of vibrational energy in $MV^{+\bullet}$ was obtained by measuring the absorption change as a function of probe energy (**Figure 4** and **5**), and the relaxation of population in the manifold of vibrational levels was traced in real time at four probe wavelengths (705, 762, 798 and 845 nm). At longer wavelengths with small probe energy, the vibrational relaxation of "hot" population in higher vibrational energy levels was monitored, whereas at shorter probe wavelengths relatively "cold" population in lower energy levels was detected. The faster decrease in TA intensity from 2

to 30 ps is observed in the wavelength range of 800~900 nm suggesting the more efficient energy dissipation by the “hot” population.

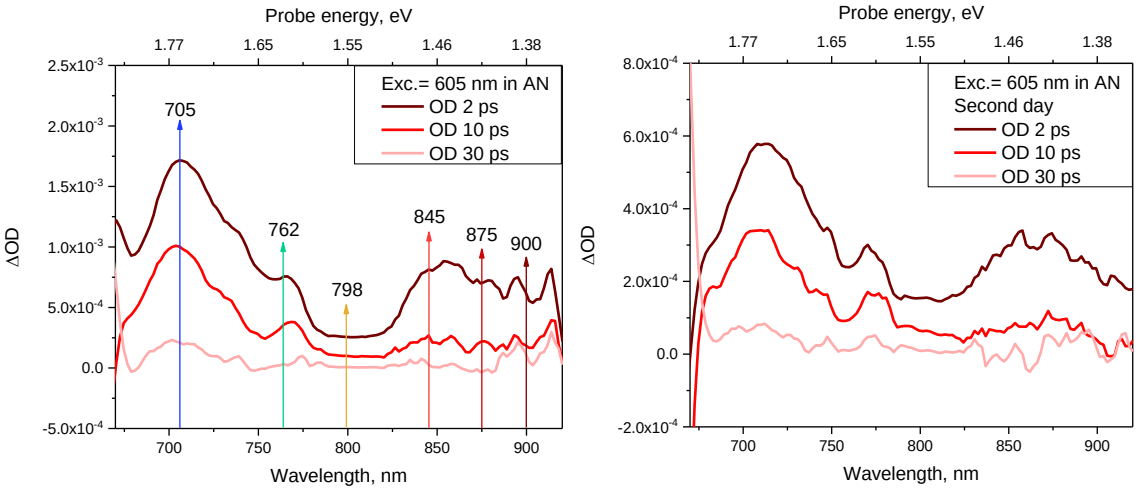

Figure 4. Transient absorption spectra of $MV^{+\bullet}$ recorded in acetonitrile at 2, 10, and 30 ps at the day when the sample was freshly prepared (left) and the following day (right). The arrows indicate the probe wavelengths which were selected to obtain the decay profiles shown in **Figure 6**.

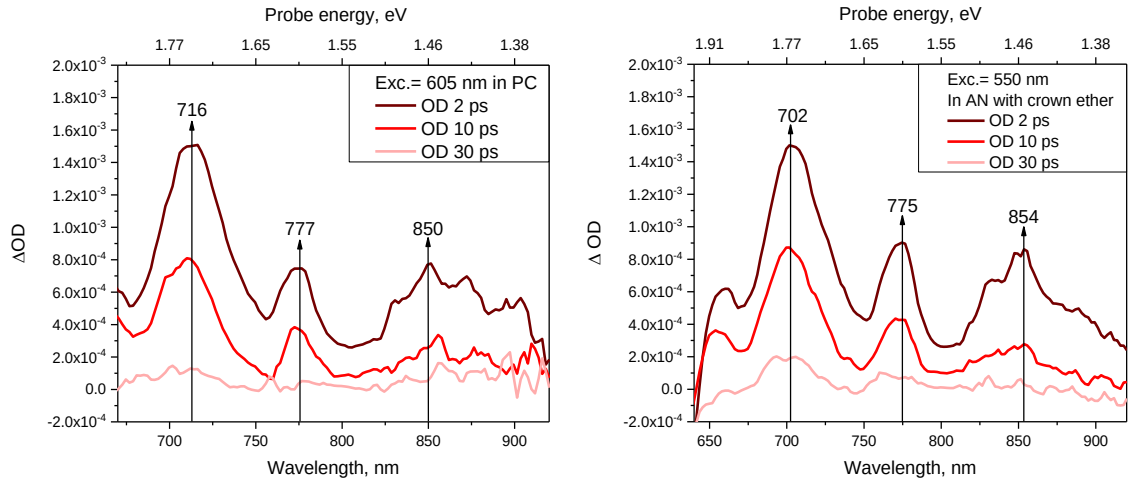

Figure 5. Transient absorption spectra of $MV^{+\bullet}$ recorded in propylene carbonate (left) and in complexation with crown ether (right) at 2, 10, and 30 ps. The arrows indicate the peak wavelengths of different vibronic bands.

5.3.3 Solvent effect and host-guest complexation on cooling dynamics of $MV^{+\bullet}$

Transient absorption decay profiles of $MV^{+\bullet}$ were obtained in acetonitrile (**Figure 6**), propylene carbonate (**Figure 7**) and in a complex with a crown ether (**Figure 8**) using 550 and 605 nm excitation. In three investigated media, the relaxation dynamics of $MV^{+\bullet}$ probed at 762, 798, and 845 nm has been precisely fitted with a double exponential function which yields components ranging from ~1.6 to 16 ps (**Table 2-4**). The two time constants, τ_1 and τ_2, cannot be easily assigned to a specific relaxation process as they reflect an ensemble of IVR, VC and solvation dynamics. In this case, both τ_1 and τ_2 are significantly influenced by the surrounding medium, suggesting that they are most likely related to the intermolecular vibrational energy transfer, that is, to VC. Therefore, we interpret that the fast component τ_1 corresponds to the primary rapid energy dissipation into the vibrational modes of surrounding medium and the slower component τ_2 is ascribed to the subsequent energy transfer to librational and translational modes of the solvent molecules. Accordingly, A_1 and A_2 can be viewed as the vibrational hot ground state population at different stages of its relaxation toward thermal equilibrium.

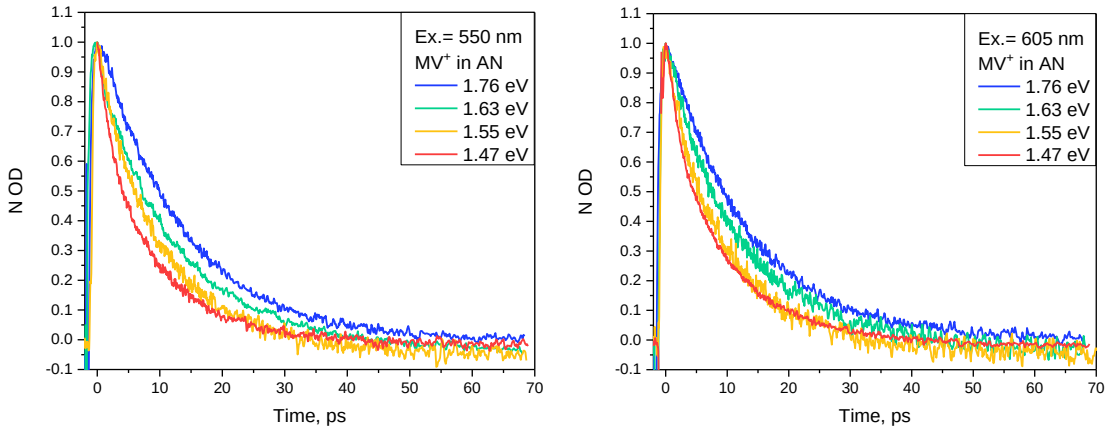

Figure 6. Transient absorption decay profiles of $MV^{+\bullet}$ in acetonitrile recorded at 705, 762, 798, and 845 nm using the excitation wavelengths of 550 nm (left) and 605 nm (right) respectively.

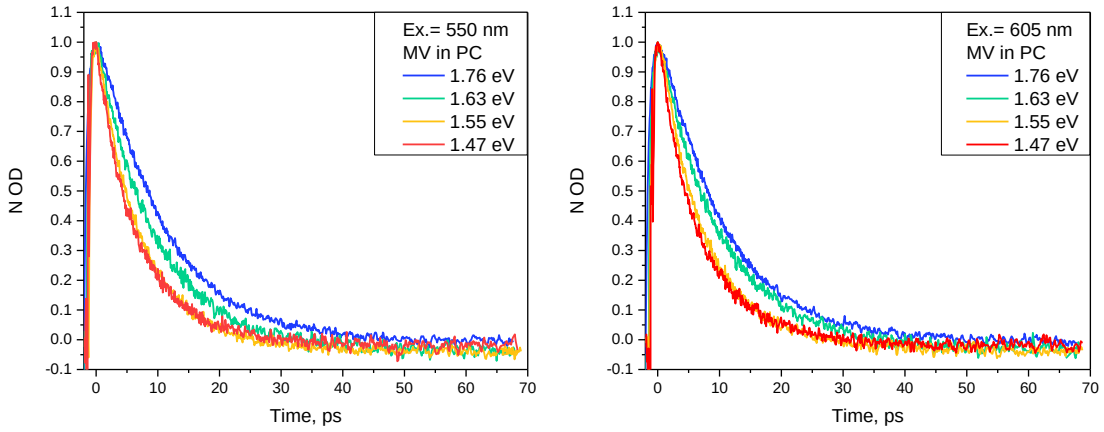

Figure 7. Transient absorption decay profiles of $MV^{+\bullet}$ in propylene carbonate recorded at 705, 762, 798, and 845 nm using the excitation wavelengths of 550 nm (left) and 605 nm (right) respectively.

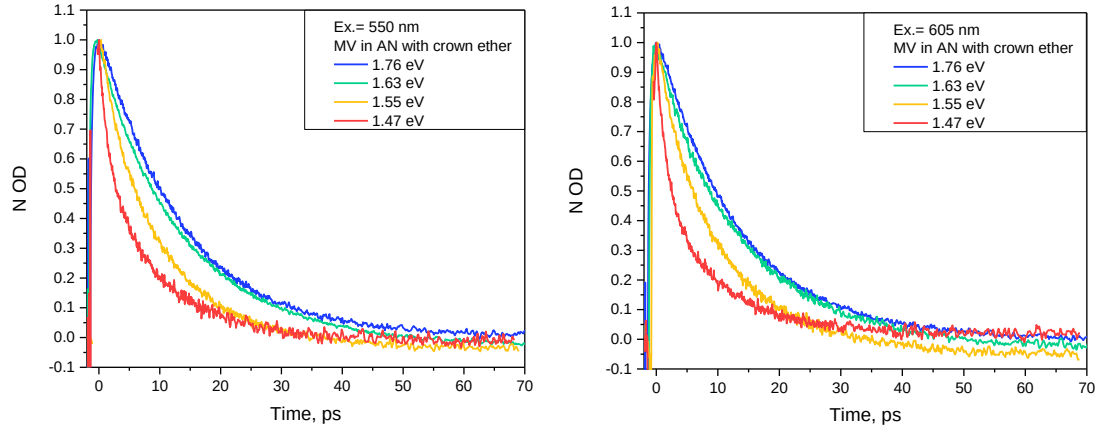

Figure 8. Transient absorption decay profiles of $MV^{+\bullet}$ encapsulated within the crown ether recorded at 705, 762, 798, and 845 nm using the excitation wavelengths of 550 nm (left) and 605 nm (right) respectively.

Table 2. Decay parameters of vibrationally hot $MV^{+\bullet}$ in acetonitrile probed at 705, 762, 798, and 845 nm.

λ_{Exc}	λ_{Pro}, eV	τ_1, ps	A_1	τ_2, ps	A_2
550 nm (2.25 eV)	1.47	2.09±0.08	0.30±0.01	10.12±0.11	0.70±0.01
	1.55	4.16±0.56	0.22±0.04	12.22±0.44	0.78±0.04
	1.63	7.80±0.97	0.37±0.11	16.40±1.37	0.63±0.11
	1.76	13.30±0.04	1.00	–	–
605 nm (2.05 eV)	1.47	1.92±0.05	0.26±0.01	10.06±0.07	0.74±0.01
	1.55	3.33±0.44	0.20±0.03	11.58±0.34	0.80±0.03
	1.63	5.51±0.70	0.30±0.07	16.02±1.05	0.70±0.07
	1.76	12.93±0.05	1.00	–	–

Table 3. Decay parameters of vibrationally hot $MV^{+\bullet}$ in propylene carbonate probed at 705, 762, 798, and 845 nm.

λ_{Exc}	λ_{Pro}, eV	τ_1, ps	A_1	τ_2, ps	A_2
550 nm (2.25 eV)	1.47	4.06±0.44	0.39±0.09	8.86±0.59	0.61±0.09
	1.55	5.87±0.46	0.35±0.16	11.57±1.55	0.65±0.16
	1.63	8.67±0.95	0.33±0.29	15.89±1.48	0.67±0.29
	1.76	10.84±0.03	1.00	–	–
605 nm (2.05 eV)	1.47	3.25±0.28	0.31±0.04	8.63±0.28	0.69±0.04
	1.55	5.45±0.35	0.38±0.09	11.37±1.14	0.62±0.09
	1.63	7.06±1.60	0.37±0.29	13.15±3.00	0.63±0.38
	1.76	10.48±0.03	1.00	–	–

Table 4. Decay parameters of vibrationally hot $MV^{+\bullet}$ encapsulated within crown ether in acetonitrile probed at 705, 762, 798, and 845 nm.

λ_{Exc}	λ_{Pro}, eV	τ_1, ps	A_1	τ_2, ps	A_2
550 nm (2.25 eV)	1.47	1.66±0.06	0.41±0.01	10.18±0.14	0.59±0.01
	1.55	2.64±0.11	0.28±0.01	11.43±0.15	0.72±0.01
	1.63	4.77±0.32	0.09±0.01	15.05±0.10	0.91±0.01
	1.76	13.44±0.03	1.00	–	–
605 nm (2.05 eV)	1.47	1.62±0.04	0.48±0.01	9.70±0.12	0.52±0.01
	1.55	2.46±0.12	0.16±0.01	10.90±0.01	0.84±0.01
	1.63	4.19±0.41	0.09±0.01	14.89±0.16	0.91±0.01
	1.76	13.06±0.02	1.00	–	–

Even though the fast component τ_1 is assigned to the initial stage of intermolecular energy transfer to surrounding molecules, the participation of IVR in the early relaxation dynamics cannot be excluded at this point. For small molecules, IVR takes place within a few ten to hundreds of picoseconds [7] and may get entangled with VC. Whereas, for larger molecules in solution, IVR speeds up very rapidly with increasing the number of atoms, *i.e.,* with the size of the molecule, due to the higher density of vibrational states. In this situation, IVR occurs in a time window ranging from 10 fs to a few hundreds of femtoseconds [9, 16, 33], which allows it to be well-separated from the subsequent VC. To assess the timescale of IVR occurring in the vibrationally excited ground state of $MV^{+\bullet}$,

the rising and initial decaying region of transient absorption probed at 705, 798 and 900 nm was fitted with a double exponential function in a short 7 ps time window (**Figure 9**). The time constant τ_{intra} with a negative amplitude indicates that the formation of "hottest" population probed at 900 nm takes place instantaneously within 185 fs (instrument resolution is 75~100 fs) and "coldest" population of time constant τ_{intra} implies the IVR process where the "hot" population with relatively high-frequency modes cools by energy redistribution in the manifold of low-frequency modes. Therefore, the component τ_{intra} corresponds to not only the $D_1 \leftarrow D_0$ internal conversion but also the intramolecular relaxation. Surprisingly, all derived time constants τ_{intra} are significantly faster than 700 fs reported by Häupl *et al* [26]. The main reason for the discrepancy is that Häupl *et al* only looked into the relaxation of "cold" population at 700 nm and did not extend the measurements into the near-IR region. Secondly, the time resolution of our instrument is ~2 times higher. Based on our results, IVR is completed within 460 fs and therefore differentiated from VC by their timescales.

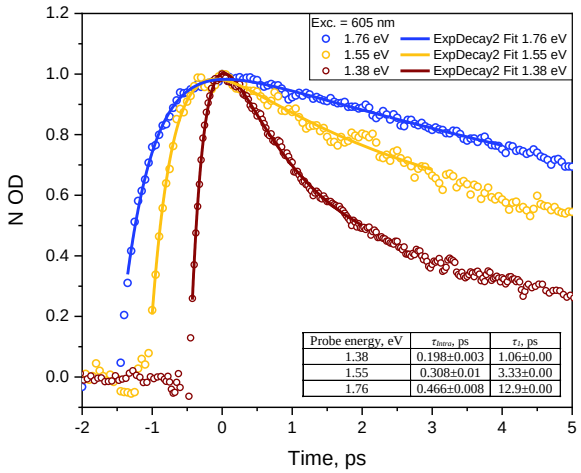

Figure 9. Biexponential fitting for the rising region of kinetic traces probed at 705, 798 and 900 nm. The inset shows the fitting parameters.

There are two extreme situations: (a) when probed at 705 nm, the "coldest" population undergoes only the latter stage of cooling and thus exhibits a monoexponential decay behavior; (b) when probed at 875 and 900 nm, the vibrational relaxation of "hottest" population displays the most pronounced biexponential behavior. The fast component decays with a time constant $\tau_1 = 1.1\sim1.3$ ps which suggests possible entanglement of initial cooling stage and subpicosecond IVR process (**Figure 10** and **Table 5**). The slow component $\tau_2 = 6.8\sim7.9$ ps corresponds to the remaining vibrational cooling process. Importantly, it should be mentioned that the absorption band of short-lived D_1 state is likely to appear in the 800~1300 nm region and superimpose on the spectrum of hot ground state. If this was the case, the very fast component τ_1 would be assigned to the lifetime of D_1 state, which is impossible considering the ~460 fs time constant for the formation of "coldest" population probed at 705 nm. The possible reason for failing to detect the D_1 state of $MV^{+\bullet}$ is that the $D_2 \leftarrow D_1$ transition lies beyond the red region of the measured spectrum or the D_1 state decays rapidly with a time constant being comparable to the time resolution of our instrument.

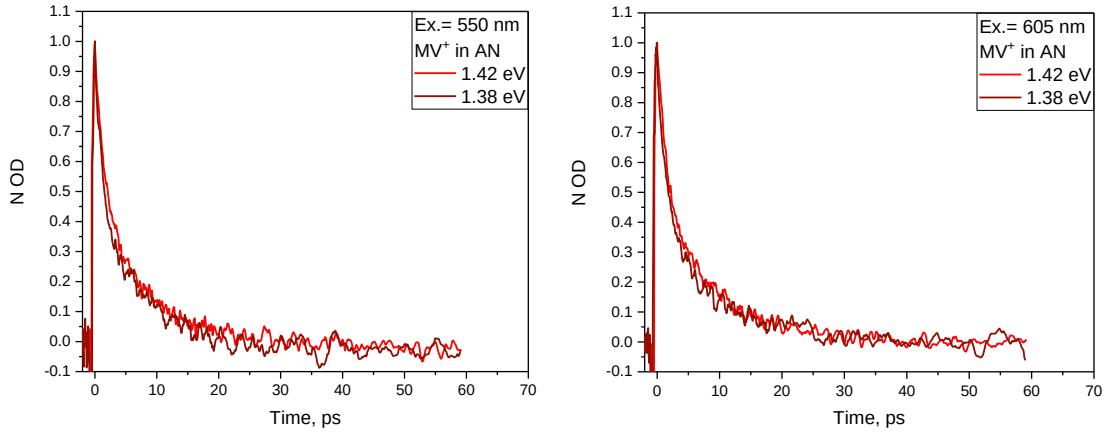

Figure 10. Transient absorption decay profiles of $MV^{+\bullet}$ in acetonitrile probed at 875 and 900 nm using excitation wavelengths of 550 nm (left) and 605 nm (right) respectively.

Table 5. Decay parameters of vibrationally hot $MV^{+\bullet}$ in acetonitrile probed at 875 and 900 nm.

λ_{Exc}	λ_{Pro}, eV	τ_1, ps	A_1	τ_2, ps	A_2
550 nm (2.25 eV)	1.38	1.09±0.16	0.46±0.04	7.18±0.40	0.54±0.03
	1.42	1.35±0.13	0.42±0.02	7.87±0.37	0.58±0.02
605 nm (2.05 eV)	1.38	1.06±0.09	0.47±0.00	6.79±0.14	0.53±0.00
	1.42	1.34±0.13	0.42±0.02	7.83±0.37	0.58±0.02

Generally, the dependence of cooling rates on the excitation energy is weak (**Figure 11**), which is consistent with the rapid internal conversion through a conical intersection. The conical intersection of D_0 and D_1 potential energy surfaces involves a few strongly coupled vibrational modes which further interact with many inactive modes resulting in vibrational energy redistribution in the ground state [34].

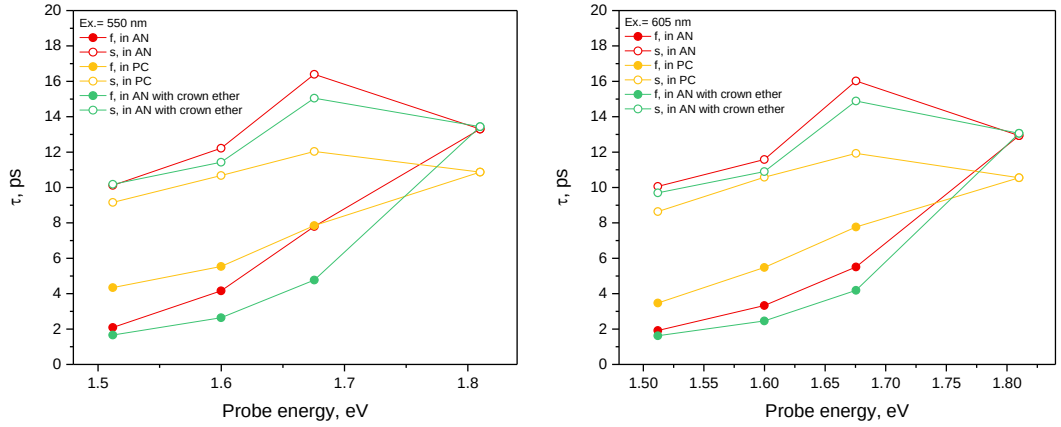

Figure 11. The fast and slow time constants extracted from the all vibrational cooling dynamics in three investigated media using the excitation wavelengths of 550 nm (left) and 605 nm (right).

Vibrational cooling of hot $MV^{+\bullet}$ in propylene carbonate exhibits a weaker dependence on the probe energy and behaves relatively monoexponentially which is reflected in the close values of fast and slow decay rates (**Figure 12a**). The slow component decaying with $\tau_2 = 8{\sim}15$ ps is faster at all probe wavelengths than that detected in acetonitrile (**Table 2** and **3**). In order to compare the cooling dynamics in a convenient

manner, transient absorption decays in both solvents were fitted using a single exponential function, and the results were plotted in **Figure 12b**. The average cooling rate significantly increases at all probe wavelengths by changing the solvent from acetonitrile to propylene carbonate, which is somewhat surprising considering the fast reorientational dynamics of the small acetonitrile molecule at room temperature. The origin of this behavior is rooted in the large number of normal modes of propylene carbonate (**Table 6**), resulting in a high and continuous density of vibrational states (VDOS). Particularly, in the range of 500~1600 cm^{-1} where numerous skeletal motions of $MV^{+\bullet}$ are located, the VDOS of propylene carbonate substantially overlaps with that of $MV^{+\bullet}$ (**Figure 13**). As a result, each mid-frequency solvent mode has a high probability to coincide with a solute mode with similar frequency, which facilitates efficient dissipation of excess vibrational energy residing within $MV^{+\bullet}$. On the contrary, the VDOS of acetonitrile is distributed at a few discrete frequencies and poorly matches the VDOS of $MV^{+\bullet}$ (**Figure 13**). In this case, the transition between the initial and final cooling stage observed in acetonitrile is not as smooth as in propylene carbonate.

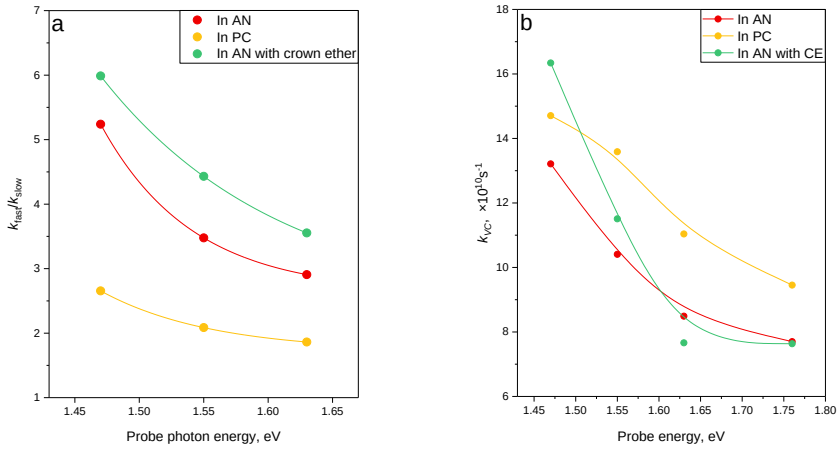

Figure 12. (a) The ratio of fast and slow decay rates as a function of probe energy for the three investigated media; (b) The vibrational cooling rates measured at several probe wavelengths.

Table 6. The number of vibrational modes of the solvent molecules within a given frequency range.

Compound	*n*	*n*(0~1600 cm^{-1})	*n*(0~1000 cm^{-1})	*n*(0~500 cm^{-1})
Acetonitrile	12	8	3	2
Propylene carbonate	33	27	13	5
$MV^{+\bullet}$	78	60	32	14
Crown ether	186	148	74	38

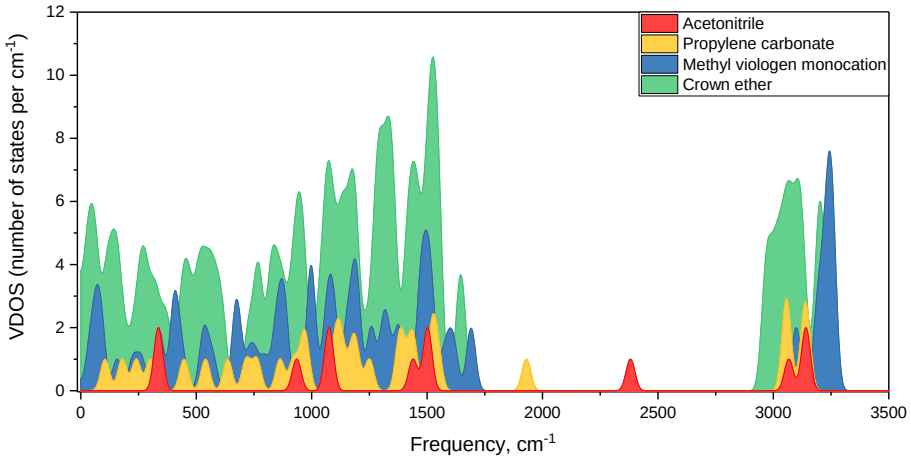

Figure 13. The density of vibrational states calculated for acetonitrile, propylene carbonate, methyl viologen, and crown ether. Only the fundamental frequencies are shown (DFT, B3LYP, in vacuum).

In comparison with other two investigated media, the vibrational cooling dynamics of $MV^{+\bullet}$ complexed with the crown ether displays the most pronounced biphasic behavior (**Figure 12a**). The initial decay of the excess vibrational energy with a time constant $\tau_1 =$ 1.6~4.8 ps is ~1.5 times faster at all probe wavelengths than the $\tau_1 = 2.0{\sim}7.8$ ps detected in pure acetonitrile (**Table 2** and **4**). Particularly, at long probe wavelengths of 798 and 845 nm, the average cooling rates of the "hot" population are remarkably faster when $MV^{+\bullet}$ is encapsulated within the ring of crown ether (**Figure 12b**). The acceleration of initial excess energy dissipation by complexation also correlates with dense vibrational states of crown ether molecule (**Figure 13**). The high- and mid-frequency vibrational modes of the host are efficiently coupled with those of the guest and hence serve as a heat sink to promote the

intermolecular energy transfer in the early stage. Once the heat exchange between $MV^{+\bullet}$ and surrounded crown ether is accomplished, the host-guest complex acts as a single solute molecule and continues to undergo the vibrational cooling by transferring energy to the librational and translational modes of acetonitrile molecules in the first solvation shell. Therefore, the latter stage of vibrational cooling is expected to proceed as slowly as the case in pure solvent. However, due to the accelerated initial energy dissipation enhanced by the complexation, the final thermal equilibration is completed earlier, leading to a faster τ_2 (**Table 4**).

5.4 Conclusion

The photoexcitation of methyl viologen radical cation in acetonitrile results in the formation of D_1 state which undergoes rapid internal conversion and generates a vibrationally hot ground state with large excess energy. This hot $MV^{+\bullet}$ primarily completes intramolecular vibrational redistribution within ~460 fs and undergoes vibrational cooling with a time constant up to 16 ps via the intermolecular process. The initial stage of vibrational cooling is associated with energy transfer to vibrational modes of the surrounding medium molecules, and the latter stage relates to energy dissipation into librational and translational modes of the solvent in the first solvation shell. Furthermore, the investigation of the influence of the solvent and complexation on the vibrational cooling dynamics of $MV^{+\bullet}$ suggests a strong correlation between cooling rates and density of vibrational states of surrounding medium. The large number of normal modes of surrounding medium with frequencies in the region of 500~1600 cm^{-1} serves as a heat sink and efficiently facilitates the vibrational cooling occurring in hot $MV^{+\bullet}$.

Since the $D_1 \leftarrow D_0$ excitation of $MV^{+\bullet}$ produces a hot ground state which gives easily detectable transients on the time scale of 1~16 ps, the characteristic spectrum of hot $MV^{+\bullet}$ can be applied to identify the possible generation of excited state of $MV^{+\bullet}$ during the photoinduced electron-transfer reactions where MV^{2+} serves as an acceptor. Further, the long persistence of hot ground state $MV^{+\bullet}$ is expected to greatly influence the escape of charge carriers from the geminate recombination in dendritic and polymeric materials such like pyrene-viologen families (see **Chapter 3** and **4**). In the broader picture, such thermal equilibration processes are of great importance for electron transfer occurring at short picosecond and subpicosecond time scales.

5.5 References

1. Fuß, W.; Lochbrunner, S.; Müller, A. M.; Schikarski, T.; Schmid, W. E.; Trushin, S. A., Pathway approach to ultrafast photochemistry: potential surfaces, conical intersections and isomerizations of small polyenes. *Chemical Physics* **1998,** *232* (1-2), 161-174.

2. Nicolet, O.; Vauthey, E., Ultrafast Nonequilibrium Charge Recombination Dynamics of Excited Donor-Acceptor Complexes. *The Journal of Physical Chemistry A* **2002,** *106* (23), 5553-5562.

3. Aßmann, J.; Kling, M.; Abel, B., Watching Photoinduced Chemistry and Molecular Energy Flow in Solution in Real Time. Angewandte Chemie International Edition 2003, 42 (20), 2226-2246.

4. Seilmeier, A.; Kaiser, W., Ultrashort Intramolecular and Intermolecular Vibrational Energy Transfer of Polyatomic Molecules in Liquids. In *Ultrashort Laser Pulses and*

Applications, Kaiser, W., Ed. Springer Berlin Heidelberg: Berlin, Heidelberg, 1988; pp 279-317.

5. Pigliucci, A.; Vauthey, E., Vibrational relaxation dynamics of polyatomic molecules in solution. *CHIMIA International Journal for Chemistry* **2003,** *57* (4), 200-203.

6. Kenkre, V. M.; Tokmakoff, A.; Fayer, M. D., Theory of Vibrational-Relaxation of Polyatomic-Molecules in Liquids. *J Chem Phys* **1994,** *101* (12), 10618-10629.

7. Nesbitt, D. J.; Field, R. W., Vibrational Energy Flow in Highly Excited Molecules: Role of Intramolecular Vibrational Redistribution. *The Journal of Physical Chemistry* **1996,** *100* (31), 12735-12756.

8. Wurzer, A. J.; Wilhelm, T.; Piel, J.; Riedle, E., Comprehensive measurement of the S1 azulene relaxation dynamics and observation of vibrational wavepacket motion. *Chem Phys Lett* **1999,** *299* (3-4), 296-302.

9. Kovalenko, S. A.; Schanz, R.; Hennig, H.; Ernsting, N. P., Cooling dynamics of an optically excited molecular probe in solution from femtosecond broadband transient absorption spectroscopy. *J Chem Phys* **2001,** *115* (7), 3256-3273.

10. Yoo, H. S.; DeWitt, M. J.; Pate, B. H., Vibrational Dynamics of Terminal Acetylenes: II. Pathway for Vibrational Relaxation in Gas and Solution. *The Journal of Physical Chemistry A* **2004,** *108* (8), 1365-1379.

11. Elles, C. G.; Cox, M. J.; Crim, F. F., Vibrational relaxation of CH3I in the gas phase and in solution. *The Journal of Chemical Physics* **2004,** *120* (15), 6973-6979.

12. Ka, B. J.; Geva, E., Classical vs quantum vibrational energy relaxation pathways in solvated polyatomic molecules. *J Phys Chem A* **2006,** *110* (49), 13131-13138.

13. Owrutsky, J. C.; Raftery, D.; Hochstrasser, R. M., Vibrational-Relaxation Dynamics in Solutions. *Annu Rev Phys Chem* **1994,** *45,* 519-555.

14. Sukowski, U.; Seilmeier, A.; Elsaesser, T.; Fischer, S. F., Picosecond Energy-Transfer of Vibrationally Hot Molecules in Solution: Experimental Studies and Theoretical Analysis. *J Chem Phys* **1990,** *93* (6), 4094-4101.

15. Gottfried, N. H.; Seilmeier, A.; Kaiser, W., Transient Internal Temperature of Anthracene after Picosecond Infrared Excitation. *Chem Phys Lett* **1984,** *111* (4-5), 326-332.

16. Wild, W.; Seilmeier, A.; Gottfried, N. H.; Kaiser, W., Ultrafast Investigations of Vibrationally Hot Molecules after Internal-Conversion in Solution. *Chem Phys Lett* **1985,** *119* (4), 259-263.

17. Iwaki, L. K.; Deak, J. C.; Rhea, S. T.; Dlott, D. D., Vibrational energy redistribution in liquid benzene. *Chem Phys Lett* **1999,** *303* (1-2), 176-182.

18. Mishra, P. K.; Vendrell, O.; Santra, R., Ultrafast Energy Transfer from Solvent to Solute Induced by Subpicosecond Highly Intense THz Pulses. *J Phys Chem B* **2015,** *119* (25), 8080-8086.

19. Beer, M.; Longuet-Higgins, H. C., Anomalous Light Emission of Azulene. *The Journal of Chemical Physics* **1955,** *23* (8), 1390-1391.

20. Ippen, E. P.; Shank, C. V.; Woerner, R. L., Picosecond dynamics of azulene. *Chem Phys Lett* **1977,** *46* (1), 20-23.

21. Wagner, B. D.; Szymanski, M.; Steer, R. P., Subpicosecond pump-probe measurements of the electronic relaxation rates of the S1 states of azulene and related compounds in polar and nonpolar solvents. *The Journal of Chemical Physics* **1993,** *98* (1), 301-307.

22. Bearpark, M. J.; Bernardi, F.; Clifford, S.; Olivucci, M.; Robb, M. A.; Smith, B. R.; Vreven, T., The Azulene S1State Decays via a Conical Intersection: A CASSCF Study with MMVB Dynamics. *Journal of the American Chemical Society* **1996,** *118* (1), 169-175.

23. Monk, P., The Viologens: Physicochemical Properties, Synthesis and Applications of the Salts of 4,4'-bipyridine, *John Wiley & Sons Ltd., Chichester, England* **1989**.

24. Ballardini, R.; Balzani, V.; Credi, A.; Gandolfi, M. T.; Venturi, M., Artificial Molecular-Level Machines: Which Energy to Make Them Work? *Accounts of Chemical Research* **2001,** *34* (6), 445-455.

25. Pease, A. R.; Jeppesen, J. O.; Stoddart, J. F.; Luo, Y.; Collier, C. P.; Heath, J. R., Switching Devices Based on Interlocked Molecules. *Accounts of Chemical Research* **2001,** *34* (6), 433-444.

26. Haupl, T.; Lomoth, R.; Hammarstrom, L., Femtosecond dynamics of the photoexcited methyl viologen radical cation. *J Phys Chem A* **2003,** *107* (4), 435-438.

27. Huang, Y. X.; Hopkins, J. B., Femtosecond resonance Raman investigation of four univalent bipyridinium radicals. *J Phys Chem-Us* **1996,** *100* (23), 9585-9591.

28. Ferrer, B.; Rogez, G.; Credi, A.; Ballardini, R.; Gandolfi, M. T.; Balzani, V.; Liu, Y.; Tseng, H. R.; Stoddart, J. F., Photoinduced electron flow in a self-assembling supramolecular extension cable. *P Natl Acad Sci USA* **2006,** *103* (49), 18411-18416.

29. Watanabe, T.; Honda, K., Measurement of the Extinction Coefficient of the Methyl Viologen Cation Radical and the Efficiency of Its Formation by Semiconductor Photocatalysis. *J Phys Chem-Us* **1982,** *86* (14), 2617-2619.

30. Forster, M.; Girling, R. B.; Hester, R. E., Infrared, Raman and Resonance Raman Investigations of Methylviologen and Its Radical Cation. *J Raman Spectrosc* **1982,** *12* (1), 36-48.

31. Poizat, O.; Sourisseau, C.; Corset, J., Vibrational and electronic study of the methyl viologen radical cation MV+. in the solid state. *Journal of Molecular Structure* **1986,** *143*, 203-206.

32. Lu, T. H.; Cotton, T. M.; Hurst, J. K.; Thompson, D. H. P., A Raman and Surface-Enhanced Raman-Study of Asymmetrically Substituted Viologens. *J Phys Chem-Us* **1988,** *92* (24), 6978-6985.

33. Elsaesser, T.; Kaiser, W., Vibrational and Vibronic Relaxation of Large Polyatomic Molecules in Liquids. *Annu Rev Phys Chem* **1991,** *42* (1), 83-107.

34. Domcke, W.; Yarkony, D. R.; Horst, K., *Conical intersections: electronic structure, dynamics and spectroscopy*. World Scientific: 2004; Vol. 15.